

Washington University in St. Louis

Washington University Open Scholarship

McKelvey School of Engineering Theses & Dissertations

McKelvey School of Engineering

Summer 8-15-2022

Droplet-based Two-phase Thermal Management

Junhui Li

Washington University in St. Louis

Follow this and additional works at: https://openscholarship.wustl.edu/eng_etds



Part of the [Thermodynamics Commons](#)

Recommended Citation

Li, Junhui, "Droplet-based Two-phase Thermal Management" (2022). *McKelvey School of Engineering Theses & Dissertations*. 792.

https://openscholarship.wustl.edu/eng_etds/792

This Dissertation is brought to you for free and open access by the McKelvey School of Engineering at Washington University Open Scholarship. It has been accepted for inclusion in McKelvey School of Engineering Theses & Dissertations by an authorized administrator of Washington University Open Scholarship. For more information, please contact digital@wumail.wustl.edu.

WASHINGTON UNIVERSITY IN ST. LOUIS

McKelvey School of Engineering
Department of Mechanical Engineering & Materials Science

Dissertation Examination Committee:

Patricia Weisensee, Chair

Ramesh Agarwal

Richard Axelbaum

Mark Meacham

David Peters

Droplet-Based Two-Phase Thermal Management

by

Junhui Li

A dissertation presented to
the McKelvey School of Engineering
of Washington University in
partial fulfillment of the
requirements for the degree
of Doctor of Philosophy

December 2022
St. Louis, Missouri

© 2022, Junhui Li

Table of Contents

List of Figures	v
List of Tables	x
List of Abbreviations	xi
List of Symbols	xii
Acknowledgements	xiv
Abstract	xv
Chapter 1: Introduction and Literature Review	1
1.1 Introduction	1
1.2 Droplet evaporation	3
1.3 Droplet impact on heated surfaces and Leidenfrost	6
1.4 Molten droplet impact	10
1.5 Outline of the Dissertation	12
Chapter 2: Investigation of the Confinement Effect on the Evaporation Behavior of a Droplet Pinned on a Micropillar Structure	15
2.1 Introduction and background	15
2.2 Simulation Methodology of Droplet Evaporation	18
2.3 Results and discussions	23
2.3.1 Isothermal evaporation in room temperature	23
2.3.2 Approximate solution of droplet evaporation atop a pillar structure under isothermal conditions	24
2.3.3 The combined effects from contact angle and pillar height on vapor diffusion confinement	27
2.4 The effect of micropillar height on vapor diffusion confinement for droplet evaporation on heated substrate	31
2.5 Experimental Validation	34
2.6 Conclusion	37
Chapter 3: Low Weber Number Droplet Impact on Heated Hydrophobic Surfaces	39
3.1 Introduction	39
3.2 Experimental methods	42
3.2.1 Sample fabrication	42

3.2.2	Experimental setup	43
3.2.3	Heat transfer analysis and data processing	44
3.2.4	Uncertainty analysis	50
3.3	Results and Discussions	51
3.3.1	Droplet impact on a smooth hydrophobic surface	51
3.3.2	Bubble entrapment and inner contact line heat transfer	59
3.4	Surface roughness effect	72
3.5	Conclusion.....	75
Chapter 4: Droplet Impact and Leidenfrost Dynamics on a Heated Post.....		77
4.1	Introduction	77
4.2	Experimental method	79
4.2.1	Sample preparation	79
4.2.2	Experimental setup	80
4.2.3	Uncertainty analysis	81
4.3	Results and Discussions	82
4.3.1	Droplet lifetime and Leidenfrost temperature	82
4.3.2	Boiling regimes and droplet breakup.....	88
4.3.3	Cooling capacity in the nucleate boiling regime	95
4.3.4	Droplet impact on inclined surfaces	102
4.4	Conclusion.....	107
Chapter 5: Heat Transfer Mechanism of Molten Droplet Impact.....		109
5.1	Introduction	109
5.2	Experimental method	109
5.3	Results and discussions	111
5.3.1	Transient heat transfer of paraffin droplets for impact at room temperature	111
5.3.2	Effect of impact Weber number	114
5.3.3	Effect of droplet conductivity	115
5.4	Conclusion.....	118
Chapter 6: Conclusions and Outlook		119
6.1	Conclusions	119
6.2	Outlook and future work	121

References..... 123

Appendix 1: Sample fabrication and experimental uncertainty of droplet evaporation on the micropillar..... 136

List of Figures

Figure 1-1 Schematic of local evaporative flux distribution of a droplet evaporating at different contact angles. The red arrows represent the strength and the direction of the evaporative flux at the droplet surface.....	5
Figure 1-2 Evaporation regimes of droplet impact at different wall temperatures ¹⁰	7
Figure 1-3 A general droplet impact process in the film evaporation regime	8
Figure 1-4 Schematic of a Leidenfrost droplet	9
Figure 2-1 Schematic of vapor molecules (blue dots) diffusing away from the liquid-vapor interface for a droplet evaporating on: (a) a flat substrate, (b) a micropillar, and (c) a heated micropillar. Black arrows show the direction of vapor diffusion. The finite height of the micropillar structure enables the vapor molecules to diffuse partially downward, which is prohibited in evaporation on a flat substrate. For a droplet evaporating on a heated micropillar, the high temperature near the contact line will further promote a stronger vapor diffusion rate at the contact region and create a more non-uniform distribution of local evaporation rate along the liquid-vapor interface. For simplicity, the interior channel is not shown, but its effects are included in the numerical model.....	17
Figure 2-2 Schematic of the computational domain and boundary conditions of the simulation method. For the isothermal condition, only concentration boundary conditions are applied. For the heated condition, a constant temperature boundary condition is further imposed at the bottom surface of the micropillar.	19
Figure 2-3 The iso-concentration contour with the vector plot of local evaporative flux J , along the liquid-air interface at four different pillar heights: (a) $0R$, (b) $0.25R$, (c) $0.75R$ and (d) $2R$. The concentration of the vapor domain is represented by the different colored contour lines. The length and the direction of the red arrow represents the magnitude and the direction vector of the evaporative flux.	24
Figure 2-4 Simulation results and the approximate solution for the total evaporation rate m , at different pillar heights. The horizontal axis value $h = r/R$ represents the nondimensional pillar height.....	26
Figure 2-5 Simulation results for local evaporation rates along the liquid-air interface at different pillar heights (a) $0R$, (b) $0.1R$, (c) $0.5R$, and (d) $2R$ with different contact angles.	30
Figure 2-6 Simulation results of evaporation rates on various pillar heights at three different substrate temperatures 60°C , 80°C , and 98°C . The evaporation rates for different pillar heights are normalized with respect to the evaporation rate for a pillar height of zero. For substrate temperatures of 60°C , 80°C , and 98°C , the largest evaporation rates occur at pillar heights of $h = 5.5$, $h = 3$, and $h = 0$, respectively. As the substrate temperature increases, the evaporation rate decreases faster as it exceeds the maximum value, which indicates that a conductive resistance is more critical at higher temperature condition.	34

Figure 2-7 Photographs of evaporating droplets on two different micropillars, taken at three different times. Both droplets have the same contact diameter. The droplet evaporating on the micropillar with a height of $2R$ shrinks faster over time, while the droplet evaporating on a flat substrate (i.e., $h = 0R$) experiences a smaller change over the same time period. Thus, the evaporation rate of a supported droplet increases with increasing pillar height.....	36
Figure 2-8 Total evaporation rates from experimental data, simulation results, and the approximate solution for isothermal evaporation at different pillar heights. Images are taken from the video of the evaporation process where the contact angle equals 90° . The simulation results match the experimental data within 5%. The maximum difference occurs at a pillar height of $150 \mu\text{m}$ ($h = 3$).....	36
Figure 3-1 Schematic of the heater design and fabrication process of the smooth hydrophobic IR-transparent sample	43
Figure 3-2 Schematic of the experimental setup.....	44
Figure 3-3 Schematic of the heat transfer analysis	45
Figure 3-4 Comparison of the calculated heat flux using Ansys Fluent, the in-house 3D simulation, the in-house 1D simulation, and the pseudo-1D method.....	49
Figure 3-5 Experimental result using synchronized high-speed optical and IR imaging of a droplet impacting a smooth hydrophobic surfaces at $We = 1.6$ and substrate temperature of 50°C : (a) High-speed camera snapshots of the droplet shape, (b) corresponding temperature, and (c) heat flux distributions. Scale bars are 0.5 mm . The white dashed line in b) at 3.9 ms marks half of the the maximum spreading area that is used to calculate the area-weighted total heat fluxes.	52
Figure 3-6 The heat flux evolution of droplet impact at $We = 1.6$ and substrate temperature at $50 \pm 0.5^\circ\text{C}$. (a) The contact line heat flux (maximum heat flux within ± 3 pixel from the contact line) plotted against the corresponding contact line velocity. (b) Transient behavior of the heat flux normalized by the maximum spreading area. The uncertainty in heat flux values is universally 11.2% . Error bars are omitted for the sake of clarity.	54
Figure 3-7 The total transferred heat at substrate temperatures of $50 \pm 0.5^\circ\text{C}$ (black triangle) and $65 \pm 0.5^\circ\text{C}$ (blue square) and the corresponding $D1.25v$ value. The dashed lines are the linear curve fittings of the two data sets, with R^2 value 0.968 (black) and 0.974 (blue). Droplets at two sizes, $D = 1.6 \pm 0.05 \text{ mm}$ and $D = 1.8 \pm 0.05 \text{ mm}$ at impact velocities from around 0.2 m/s to 0.6 m/s were tested.....	57
Figure 3-8 Comparison of scaling models for the total transferred heat at substrate temperatures of $50 \pm 0.5^\circ\text{C}$ (black triangle) and $65 \pm 0.5^\circ\text{C}$ (blue square) for (a) $We^{0.859}$ as derived from Liang <i>et al.</i> ¹⁴³ and (b) $\beta_{max} 2D^{1.5}$ from Laan <i>et al.</i> ¹⁴⁴	59
Figure 3-9 Bubble entrapment during droplet impact on a smooth Teflon AF surface with $We = 3.0$ at substrate temperatures of (a) 22°C , (b) $50 \pm 0.5^\circ\text{C}$, and (c) $65 \pm 0.5^\circ\text{C}$. (d) Bubble entrapment behavior at different Weber numbers, substrate temperatures, and surface	

chemistries. The contact angles of the PDMS surface are $\theta_{eq} = 104^\circ$, $\theta_{ad} = 110^\circ$, and $\theta_{re} = 87^\circ$. The contact angles of the HTMS surface are $\theta_{eq} = 100^\circ$, $\theta_{ad} = 103^\circ$, and $\theta_{re} = 84^\circ$. As a reminder, contact angles on Teflon AF are $\theta_{eq} = 115^\circ$, $\theta_{ad} = 126^\circ$, and $\theta_{re} = 111^\circ$ 61

Figure 3-10 Bubble entrapment during droplet impact on different hydrophobic surfaces at room temperature (22°C). (a) Teflon AF surface at $We = 3.0$, (b) PDMS surface at $We = 2.5$, (c) HTMS surface at $We = 3.4$ 63

Figure 3-11 Experimental result for bubble entrapment during droplet impact on heated surfaces (a,d) side-view images of the droplet shape, and (b,e) corresponding temperature, and (c,f) heat flux distributions. (a-c): $We = 4.0$, substrate temperature $50 \pm 0.5^\circ\text{C}$; ((d-f): $We = 2.8$, substrate temperature $65 \pm 0.5^\circ\text{C}$. Scale bars are 0.5 mm. 65

Figure 3-12 The heat flux at the inner contact line (black triangles) and the primary outer contact line (red squares). Plotted are the average heat flux values of the right and left side of the contact lines along the symmetry axis. (a) $We = 4.0$, substrate temperature $50 \pm 0.5^\circ\text{C}$, (b) $We = 2.8$, substrate temperature $65 \pm 0.5^\circ\text{C}$ 67

Figure 3-13 The transient evolution of total transferred heat during droplet impact with and without an entrapped bubble at (a) $50 \pm 0.5^\circ\text{C}$ substrate and (b) $65 \pm 0.5^\circ\text{C}$ substrate. The droplet impact experiments with the bubble entrapment were conducted near the upper limit of the Weber number range of bubble occurrence. Then the impact height was increased ever so slightly to obtain a droplet impact condition without bubble entrapment..... 68

Figure 3-14 The heat flux distribution in bottom view for bubble entrapment at (a) $We = 4.0$ and substrate temperature of $50^\circ\text{C} \pm 0.5^\circ\text{C}$, (c) $We = 2.8$ and substrate temperature of $65 \pm 0.5^\circ\text{C}$; The total transferred heat during the droplet impact with a trapped bubble, with trapped bubble excluding the inner evaporation, and without the entrapped bubble at a substrate temperature of (b) $50 \pm 0.5^\circ\text{C}$ and (d) $65 \pm 0.5^\circ\text{C}$ 70

Figure 3-15 Heat flux distributions near the bubble and inner contact line regions. The color bar of the images is based on the heat flux value of the inner contact line region. The scale bars are 0.5mm. (a), (b) The heat flux distributions at different times after impact and the transient maximum heat flux near the inner contact line region with an initial substrate temperature of 50°C at $We = 2.6$. Note the different time scale as compared to Figure 3-12. (c), (d) Same data, but for an initial substrate temperature of 65°C at $We = 2.4$ 71

Figure 3-16 Surface topography and droplet spreading on the smooth and rough Teflon AF surfaces. (a) AFM surface topography images of the smooth Teflon AF surface (top) and the rough Teflon AF (bottom), with scale bars of $5\mu\text{m}$. (b) The maximum spreading diameter, β_{max} , of droplet impact on the two surfaces at different impact Weber numbers. 73

Figure 3-17 Droplet impact on smooth and rough Teflon AF surfaces with an initial surface temperature of $65 \pm 0.5^\circ\text{C}$ (a) Transient behavior of the area-weighted average heat flux. (b) Change of the area-weighted average temperature.....	74
Figure 4-1 Schematic of the experimental setup.....	81
Figure 4-2 Droplet evaporation lifetime on the post and flat substrates at different initial substrate temperatures for $We \approx 1.5$. The snapshots compare typical droplet shapes at $T_s = 165^\circ\text{C}$	83
Figure 4-3 Image sequence of droplet impact on a flat (top) and a post (bottom) substrate at $T_s = 165^\circ\text{C}$	85
Figure 4-4 Analytical model to estimate the temperature distribution along the cylindrical post. (a) The boundary conditions of the 1D heat equation. (b) Estimated temperature distribution along the post for $T_s = 165^\circ\text{C}$ using Eq. 4.4. The dashed horizontal line represents the Leidenfrost temperature of the flat surface.....	86
Figure 4-5 Typical water droplet dynamics and boiling modes on the post substrate. (a) Deposition at $We = 50, T_s = 120^\circ\text{C}$; (b) Atomization at $We = 25, T_s = 160^\circ\text{C}$; (c) Rebound with atomization at $We = 25, T_s = 240^\circ\text{C}$; (d) Breakup with atomization at $We = 50, T_s = 250^\circ\text{C}$; (e) Rebound at $We = 50, T_s = 330^\circ\text{C}$; (f) Breakup at $We = 74, T_s = 330^\circ\text{C}$	90
Figure 4-6 We - T_s regime maps for droplet impact on (a) a post substrate and (b) a flat substrate. Six different impact and boiling modes are observed. The orange dashed line is a visual guide for the transition between droplet rebound and non-rebound regimes. The black dashed line represents the transition between rebound and breakup regimes...	91
Figure 4-7 Comparison of droplet (breakup) dynamics for different substrate temperatures (all at $We \approx 57$). (a) Low-temperature breakup mode at $T_s = 190^\circ\text{C}$. (b) Mid-temperature non-breakup transition mode at $T_s = 210^\circ\text{C}$. (c) High-temperature breakup mode at $T_s = 230^\circ\text{C}$. (d) Schematics of the different breakup mechanisms.....	93
Figure 4-8 Image sequence of the droplet impact at $We \approx 57$ on (a) a flat substrate at $T_s = 180^\circ\text{C}$, (b) a post substrate at $T_s = 180^\circ\text{C}$, (c) a flat substrate at $T_s = 320^\circ\text{C}$, and (d) a post substrate at $T_s = 320^\circ\text{C}$. The top view snapshots are recorded at an angle of approximately 20° from the vertical.	95
Figure 4-9 Area-weighted average bottom-surface temperatures for (a) $T_s = 110^\circ\text{C}$, (b) $T_s = 130^\circ\text{C}$, (c) $T_s = 150^\circ\text{C}$, and (d) $T_s = 165^\circ\text{C}$. within the droplet lifetime on the post substrate. The x-axis is the non-dimensional time $t^* = t/t_0$, where t is the real time and t_0 is the droplet lifetime on the post substrate. For all the experiments, droplets were initially at room temperature ($\approx 25^\circ\text{C}$) and impacted the substrates with $We \approx 20$	97
Figure 4-10 High-speed snapshots of the bubble generation and boiling behavior at (a) $T_s = 110^\circ\text{C}$ and (b) $T_s = 150^\circ\text{C}$. The view is tilted from the horizontal by approximately 5° for better visualizations of the post structure and the bubbles inside the droplet....	99

Figure 4-11 Area-weighted average bottom surface temperature for multi-droplet impact at (a) $T_s = 110^\circ\text{C}$, (b) $T_s = 130^\circ\text{C}$, (c) $T_s = 150^\circ\text{C}$, and (d) $T_s = 165^\circ\text{C}$. The volume flow rate is $31.5 \mu\text{L/s}$ for 110°C , and $137.5 \mu\text{L/s}$ for all other cases. For all the experiments $We \approx 20$	102
Figure 4-12 High-speed and IR imaging sequence of droplets impacting on the post and flat substrates inclined at 30° at an initial temperature of $T_s = 145^\circ\text{C}$	104
Figure 4-13 High-speed and IR imaging sequence of droplets impacting on a flat and a post substrate inclined at 30° at an initial temperature of $T_s = 160^\circ\text{C}$	105
Figure 4-14 Temporal evolution of the area-weighted average bottom surface temperature for the two surfaces at (a) $T_s = 145^\circ\text{C}$ and (b) $T_s = 160^\circ\text{C}$ at an inclination angle of 30° from the horizontal.....	106
Figure 4-15 High-speed imaging sequence of off-center droplets impacting the post substrates inclined at 30° at initial temperatures of $T_s = 145^\circ\text{C}$. The horizontal distance from the impact location to the center of the post is 1.0 mm (top) and 1.6 mm (bottom).	107
Figure 5-1 Experimental setup of molten droplet impact	110
Figure 5-2 Experimental result using synchronized high-speed optical and IR imaging of a paraffin droplet impacting a Teflon AF surface at $We = 70$ at room temperature: high-speed camera snapshots of the droplet shape (top row), the corresponding temperature (middle row), and heat flux distributions (bottom row). The temperature color bar for the $t = 6.0, 7.6,$ and 13.2 ms is modified to show the temperature distribution at the interface, while the other sample area remains at room temperature (25°C). The scale bar is 1mm.....	112
Figure 5-3 Heat flux evolution of paraffin droplet impact at $We = 70$ and a substrate originally at room temperature ($25 \pm 0.5^\circ\text{C}$). (a) Transient heat flux at the contact line and central region (1 mm^2 surrounding the impact location). (b) Transient behavior of the heat flux normalized by the maximum spreading area. The uncertainty in heat flux values is universally 10%. Error bars are omitted for the sake of clarity.	114
Figure 5-4 Heat transfer behavior at different impact Weber numbers. (a) The total transferred heat; (b) The transient heat flux distributions at $t = 56$ ms.	115
Figure 5-5 Experimental result using synchronized high-speed optical and IR imaging of a Field's metal droplet impacting a Teflon AF surface at $We = 42$ at room temperature: Temperature distributions (top row), and the corresponding heat flux distributions (bottom row).	117
Figure 5-6 Temperature history of the center region (0.02 mm^2 around the impact location on the solid surface) of a Field's metal droplet impacting a Teflon AF surface at $We = 42$ at room temperature	118

List of Tables

Table 2-1 Simulation setup	22
Table 2-2 Total evaporation rates at different substrate temperatures.....	37

List of Abbreviations

AFM	Atomic force microscopy
CA	Contact angle
CCA	Constant contact angle
CCR	Constant contact radius
CHF	Critical heat flux
CL	Contact line
DI	De-ionized (water)
fps	Frames per second
HTMS	(heptadecafluoro-1,1,2,2-tetrahydrodecyl)trimethoxysilane
IPA	Isopropanol
IR	Infrared
LED	Light-emitting diode
PDMS	Polydimethylsiloxane
rpm	Revolutions per minute
RTD	Resistance temperature detectors
TIR	Total internal reflection

List of Symbols

A	Area (m^2)
B	Pixel length [m]
c	Concentration (mol/m^3)
C_p	Specific heat capacity ($\text{J}/\text{kg}\cdot\text{K}$)
D	Diffusion coefficient (m^2/s)
D_{pillar}	Diameter of the micropillar (m)
h	Pillar height (m)
\bar{h}	Non-dimensional pillar height
h_{fg}	Latent heat of vaporization (J/kg)
h_1	Heat transfer coefficient ($\text{W}/\text{m}^2\cdot\text{K}$)
I	Electrical current [A]
J	Local evaporative flux (kg/s)
J^*	Normalized evaporative flux
l	Arc length (m)
l^*	Normalized arc length
k	Thermal conductivity ($\text{W}/\text{m}\cdot\text{K}$)
L	Length (m)
\dot{m}	Total evaporation rate ($\text{kg}/\text{m}^2\cdot\text{s}$)
M	Molar mass (mol/m^3)
\vec{n}	Direction vector
p	Pressure (Pa)
Q	Thermal Energy (J)
q	Rate of heat transfer (W)
q''	Heat flux (W/m^2)

r	Radial location (m)
R	Droplet diameter (m)
R_e	Electric Resistance (Ω)
t	Time (s)
T	Temperature (K)
V	Droplet Volume (m^3)
\vec{V}	Velocity (m/s)
z	Axial location (m)
α	Toroidal coordinate
α_t	Thermal diffusivity (m^2/s)
β	Thermal expansion coefficient (K^{-1})
δ	Thickness (m)
γ	Kinematic viscosity (m^2/s)
μ	Dynamic viscosity (Pa·s)
ρ	Density (kg/m^3)
τ	Toroidal coordinate
ϕ	Relative humidity

Acknowledgements

First of all, I would like to acknowledge my Ph.D. advisor Dr. Patricia Weisensee, for her continuous guidance and support during my Ph.D. study. Throughout these five years, she has been showing me how to become a good researcher and, more importantly, a good person. I am deeply moved by her passion for research and encouraged by her inspiring words.

I want to thank all my committee members, Dr. Ramesh Agarwal, Dr. David Peters, Dr. Mark Meacham, and Dr. Richard Axelbaum, for their generous help in my research and career. They are all my role models who teach me through their own behaviors. I also want to thank Dr. Damena Agonafer for his guidance on the droplet evaporation project.

I want to acknowledge my colleagues and friends, Jianxing Sun, Li Shan, Wenliang Qi, Binjian Ma, and Mingyang Cui, for their assistance and support on my research projects. Finally, I want to express my appreciation to all the Thermal Fluids Lab members for their help and encouragement.

Junhui Li

Washington University in St. Louis

December 2022

ABSTRACT OF THE DISSERTATION

Droplet-Based Two-Phase Thermal Management

by

Junhui Li

Doctor of Philosophy in Mechanical Engineering

Washington University in St. Louis, 2022

Professor Patricia Weisensee, Chair

The rapid development of electronic systems with ever-higher power densities in a wide range of applications requires new advanced thermal management methods. Droplet-based two-phase thermal management technologies are considered promising solutions to conquer the cooling challenges in the electronic industries. The heat transfer behavior of droplets is based on several important fundamental processes, such as droplet evaporation, droplet impact on heated surfaces, and molten droplet impact. In this dissertation, four research projects are completed to explore the insights of these fundamental processes.

For droplet evaporation, I introduce an investigation of diffusion confinement of droplets evaporating on a supported pillar structure. We investigate the diffusion confinement effect imposed by the bottom substrate and the side wall of the micropillar through numerical simulations and experimental investigation. We find that raising the micropillar height from 0 to $2R$, $5R$, and $20R$ led to 26%, 35%, and 42% enhancements, respectively, in the total evaporation rates of a hemispherical droplet under an isothermal condition.

Moving from the static evaporation process to a dynamic process, I experimentally study the low-Weber number droplet impact on heated hydrophobic surfaces in the film evaporation

regime. Denoting the drop diameter and impact velocity as D and v , we find that the total transferred heat Q scales as $\sim D^{1.25}v$, which is validated using experiments. A unique feature of low- We droplet impact on non-wetting surfaces is the formation of a sub-millimetric entrapped bubble that forms during receding. We find that the overall heat transfer is reduced by 5.6% and 7.1% at surface temperatures of 50°C and 65°C, respectively, as the entrapped bubble reduces the total liquid-solid interface area.

After studying the droplet impact under non-boiling conditions, I continue to explore the droplet impact on a heated post in the nucleate boiling and Leidenfrost regimes to investigate the influence of the surface structure on the heat transfer and hydrodynamics. We find that the post substrate leads to a shorter droplet lifetime and a 20°C higher dynamic Leidenfrost temperature compared to a flat substrate, attributed to mixed boiling modes along the height of the post and additional pinning. In the nucleate boiling regime, the droplet impact on the post substrate shows an up to 24% larger cooling capacity due to the additional liquid-solid interface area.

Finally, I experimentally investigate the heat transfer and solidification mechanisms during molten paraffin droplet impact using synchronized high-speed optical and infrared (IR) imaging. The contact line heat transfer is found to be nearly constant during the spreading process after impact. The overall heat transfer is increased by higher impact Weber numbers due to a larger spreading area. In addition, when replacing the low-conductivity paraffin droplet with Field's metal, we find a higher local heat flux near the center region compared to the contact line region due to the higher conductivity of the metal droplet.

Overall, this dissertation presents new fundamental insights into droplet-based two-phase systems, including droplet impact, droplet evaporation and boiling, and droplet solidification.

The research outcomes enhance our understanding of static and dynamic phase change processes and provide fundamental theories for developing droplet-based two-phase thermal management systems.

Chapter 1: Introduction and Literature

Review

1.1 Introduction

Nowadays, electronic devices are being integrated with everyday life in different conditions and applications. With the increasing demand for market development, electronic devices move towards multi-functionality, miniaturization, thinness, and lightness¹. However, higher packing densities and smaller device sizes lead to greater power consumption and heat flux density. Thermal management of these advanced electronic systems is becoming a critical technical challenge. The cooling requirement can be as high as $1000\text{W}/\text{cm}^2$ for some of the electronic packaging systems². However, the traditional single-phase cooling methods, such as air cooling and liquid cooling, are facing great challenges in providing enough cooling capacities. In addition to overcoming high heat fluxes, thermal management technologies also need to address the challenge of non-uniform power dissipation (*e.g.*, the existence of hot spots) and confined space constraints (*e.g.*, 3D stacked packaging)³. In an effort to overcome the various thermal challenges, droplet-based two-phase thermal management technologies, such as droplet evaporation-based micro-heat exchangers⁴⁻⁵, droplet impingement system⁶, and spray cooling systems⁷, are developed by taking advantage of both the latent heat of phase change and the small size and high mobility of the droplets. However, the physical fundamentals of droplet-based two-phase thermal management techniques are still not well understood due to the complexity of heat transfer, hydrodynamics, and phase change that are coupled in these systems. Droplet evaporation is a simultaneous heat and mass transfer phenomenon, which plays an important role in two-phase heat exchangers^{4-5, 7-8}. Evaporation is most often limited by the time

required for the saturated vapor to diffuse from the vicinity of the droplet interface to the far field⁹. Hence, the geometric features, such as the substrate and the supporting structures, typically strongly influence vapor diffusion. Understanding the effect of these features is key to enhancing evaporation rates and consequently evaporative cooling capabilities. However, little is known about the diffusion confinement posed by the geometry of a non-planar substrate and its influence on local and total heat transfer.

The physics of droplet evaporation can be more complicated when the liquid-vapor interface is combined with rapid deformation and displacement, especially when droplets impact heated surfaces. The heat transfer of this process is strongly influenced by the droplet dynamics and substrate temperature¹⁰. Understanding the fundamentals of interfacial heat transfer during the droplet impact is crucial for enhancing the cooling performance of droplet impingement applications. However, it is unclear how the local heat transfer behaves at the liquid-solid interface on a microscopic level¹¹, especially at the contact line region during the de-wetting process of the droplet impact.

The cooling efficiency of the droplet impact and evaporation is significantly reduced in the Leidenfrost regime when the surface temperature is higher than the Leidenfrost temperature (T_L). The droplet remains separated from the hot solid surface by a developing vapor layer, which acts as a thermal barrier and blocks the heat transfer¹²⁻¹³. Micro and nanostructured surfaces have been widely studied to explore their influence on heat transfer and T_L ¹⁴⁻¹⁹. However, the Leidenfrost dynamics of surfaces with structures with a similar dimension to the droplet, which are easier to manufacture and more robust than most microstructures, remain unknown. A large structure can induce a complete deformation of the entire droplet shape and thus significantly change the droplet impact behavior.

Other than the liquid-vapor system, the droplet-based solid-liquid system also draws great attention driven by important industrial applications such as thermal spray coating systems²⁰ and 3D printing²¹. During a molten droplet impact, the solidification of the droplet confines the mobility of the droplet and influences the (phase change) heat transfer characteristics of the droplet. However, the interfacial heat transfer mechanism between the droplet and substrate is not well-understood, as the heat transfer is composed of phase change and direct liquid-to-solid or solid-to-solid conduction, which changes rapidly as the droplet deforms and solidifies.

This dissertation aims to answer some of the discussed unknowns and to investigate the physical fundamentals of droplet-based two-phase thermal management systems.

1.2 Droplet evaporation

Our understanding of the droplet evaporation process has been evolving for over one hundred years. Since the 1890s, the evaporation of a droplet in an ambient gas was considered a diffusion-controlled process by Maxwell^{9, 22}. For a droplet evaporating in an open ambient environment without forced or natural convection, evaporation is most often limited by the time required for the saturated vapor to diffuse from the droplet surface to the far field. In other words, the evaporative mass transport is governed by Fick's law of diffusion:

$$J = -D \cdot \nabla c, \quad (1.1)$$

where J is the diffusive mass flux, D is the diffusion coefficient, and c is the vapor concentration. Since then, many studies have focused on the fundamentals of droplet evaporation on solid surfaces. Analysis of droplet evaporation was conducted in experimental studies with droplet sizes ranging from 1pL to 40 μ L²³. Two modes of evaporation typically occur: The constant contact radius (CCR) mode, where the contact area with the substrate remains constant

throughout the drying process, and the constant contact angle (CCA) mode, where the contact radius decreases with time but the contact angle remains invariable. For droplet evaporation in the CCR mode, the evaporation rate for a liquid with a contact angle $<90^\circ$ is linear with time. Birdi and Winter performed intensive research on the evaporation of a sessile droplet in which a constant evaporation rate is recorded by measuring the weight change of water droplets evaporating on a glass surface²⁴. Moreover, the evaporation rates of pinned sessile droplets of water on glass and n-octane on Teflon surfaces were also found to be constant over time²⁵. In contrast, evaporation from hydrophobic or superhydrophobic surfaces is not linear with time and occurs in the CCA mode until the drop reaches a certain critical height²⁶. Bourges-Monnier and Shanahan²⁷ found that contact angles remain constant when the surrounding atmosphere is saturated with the vapor of the liquid. However, as the liquid evaporates, the atmospheric vapor fraction decreases, which yields a reduced contact angle. As a result, the evaporation behavior of sessile liquid droplets was found to be closely related to the wetting characteristics (represented by the contact angle) and liquid properties, such as vapor diffusion coefficient and heat of vaporization.²⁸⁻³¹

During the evaporation process, the vapor diffusion transport from the droplet-gas interface to the environment is confined by the non-penetrating solid substrate. The spherical symmetry of the diffusion problem is lost, which increases the complexity of the problem considerably³².

Figure 1-1 shows the schematic of evaporative flux distributions of droplets evaporating solid substrates with different contact angles. Qualitatively, for hydrophilic surfaces (contact angle $< 90^\circ$), the diffusion confinement is decreased near the contact line location due to the small contact angle, which leads to an enhancement of the local evaporative flux. In contrast, a hydrophobic surface (contact angle $> 90^\circ$) reduces the local evaporative flux near the contact line

due to higher diffusion confinement in the gas wedge. The physical value that relates to diffusion confinement is the vapor concentration gradient, which is strongly influenced by geometric features.

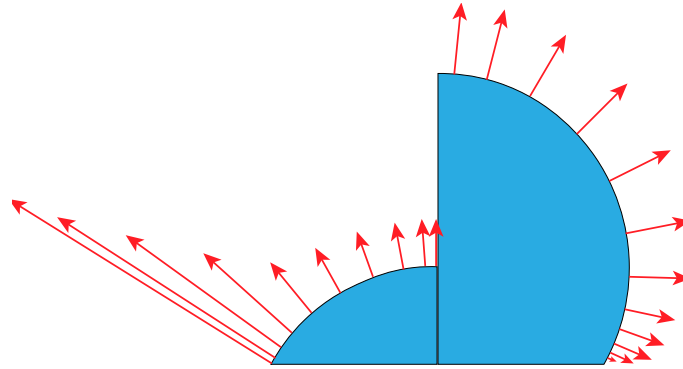


Figure 1-1 Schematic of local evaporative flux distribution of a droplet evaporating at different contact angles. The red arrows represent the strength and the direction of the evaporative flux at the droplet surface.

Numbers of studies have investigated the diffusion confinement from the solid wall³³⁻³⁴. Picknett and Bexon derived an equation to predict the wall effect by defining a capacitance C , as a function of the contact angle of the spherical cap and the radius of curvature R , *i.e.*, $f(\theta) = 1/2(C/R)$. Liebermann corrected the calculated diffusion coefficient in the study by considering the solubility of air bubbles in water and dividing by “ $\ln 2$ ” to account for the wall effects³³. Coutant and Penski performed evaporation experiments on ethylbenzene, water, and mesitylene sessile drops. Their results are in very close agreement with the early theory. Baines and James expressed the $f(\theta)$ factor in terms of the Sherwood number, which expanded the application of the theory to sessile drop evaporation in both still and moving air³⁵. Then, Rowan *et al.*³⁶ derived an approximate solution by assuming the vapor concentration gradient (dc/dR) to be radially outward. This assumption allowed obtaining a more simplified equation as $f(\theta) = (1 - \cos\theta)/2$. With the same assumption, Bourges-Monnier and Shanahan³⁷ proposed a self-consistent solution for the concentration gradient (dc/dR), where the equation for $f(\theta)$ became

$f(\theta) = -\cos\theta/2\ln(1 - \cos\theta)$. As demonstrated by these studies, the diffusive evaporation model containing the $f(\theta)$ factor has proved to be applicable to both large and small droplets in predicting the influence of the geometric diffusion confinement of a substrate³⁴.

In this dissertation, I study the influence of the geometric diffusion confinement effect of droplet evaporation on supporting structures. In addition, I also investigate the different changes on conduction resistance and diffusion resistance at varying structure heights.

1.3 Droplet impact on heated surfaces and Leidenfrost

The droplet impact on heated surfaces has been investigated since the pioneering experiments of water droplets impacting a heated surface in film boiling regime by Wachters *et al.*³⁸. With the development of experimental and computational tools, droplet impact on heated surfaces has been investigated under the influence of different parameters, such as wettability, impact velocity, and saturation temperature. However, one of the most important parameters that control the droplet impact behavior is the wall temperature. As the wall temperature increase, four evaporation regimes can be identified based on the droplet lifetime: film evaporation, nucleate boiling, transition boiling, and film boiling, shown in Figure 1-2¹⁰.

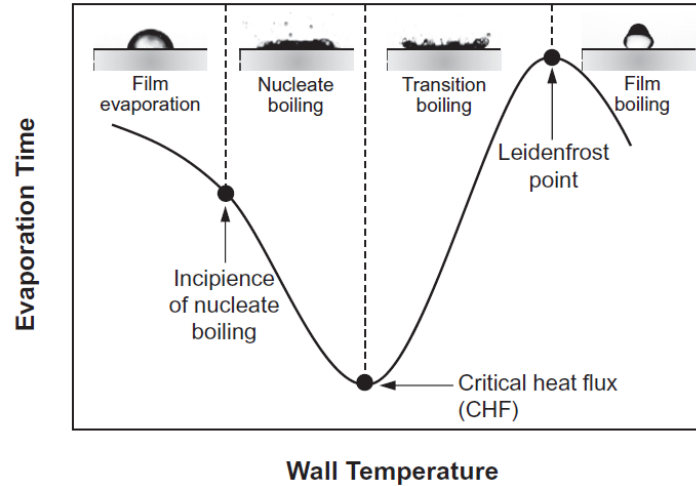


Figure 1-2 Evaporation regimes of droplet impact at different wall temperatures¹⁰

The droplets maintain film evaporation if the wall temperature is below the boiling point. In this regime, the droplet dynamics are similar to a droplet impact with isothermal conditions, where heat transfer is negligible. Figure 1-3 shows the general droplet dynamics in the film evaporation regime. After the droplet impacts the surface, the droplet immediately enters the spreading process. The kinetic energy of the droplet initiates the lateral movement of the liquid, flattening the droplet and partially converting kinetic energy into surface energy. As the droplet deforms and extends to a certain shape, *i.e.*, the maximum spreading state, the surface energy starts to transfer back to kinetic energy and drives the flat droplet to recede again. This process is called the receding process or recoil process. Then, determined by the surface wettability, the droplet either oscillates and deposits with a certain contact area and contact angle, or partially or completely lifts off the surface.

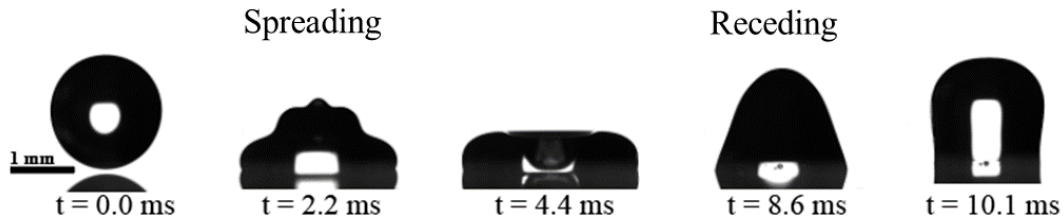


Figure 1-3 A general droplet impact process in the film evaporation regime

In film evaporation, heat transfer is dominated by heat conduction from the wall to the liquid and evaporation due to mass transfer along the liquid-gas interface. Importantly, the majority of the evaporation heat transfer occurs at the triple phase contact line³⁹ due to a relatively low thermal barrier and high concentration gradient (on hydrophilic surfaces). For moving contact lines, the contact line heat flux is higher for a advancing contact line than a receding contact line¹¹, due to a larger convection heat transfer and a higher wall temperature. Pasandideh-Fard *et al.*⁴⁰ investigated water droplets impacting a hydrophobic surface and found the cooling effectiveness to increase with the Weber number, mainly due to the increase of the liquid-solid interfacial area. Others investigated the heat transfer of bouncing droplets and found that the cooling effectiveness increase with Weber number but decreases with droplet diameter and surface cavity fraction⁴¹. Similar to a bouncing droplet, Shiri *et al.* found that for a given spreading factor, the interfacial heat transfer is related to the thermal properties of the drop and bulk substrate and also the relative thermal, inertial, and capillary dynamics of the drop⁴².

As the wall temperature becomes higher than the saturation temperature, the drop undergoes nucleate boiling. The phase change now occurs at the liquid-solid interface, where the vapor bubbles grow and coalesce until they are uplifted from the wall by buoyancy. The droplet dynamics in the nucleate boiling and transition boiling regimes (if the wall temperature is slightly higher) are very complicated due to the chaotic boiling behavior. Atomization occurs more easily on a hydrophilic surface⁴³, and can be generated from the central or the contact line

region, indicating a partial contact or a complete contact between the droplet and the solid surface⁴⁴⁻⁴⁵. Most studies concentrate on the heat transfer performance of the nucleate boiling regime, especially near the critical heat flux (CHF) point, which corresponds to the shortest drop lifetime and the highest heat flux. The spreading and splashing processes also play an important role in the overall heat transfer behavior⁴⁶. Droplets with smaller surface tension and latent heat are more likely to undergo faster boiling, which promotes the breakup of liquid drops and generation of dry surface areas, compromising cooling performance⁴⁷.

If the wall temperature exceeds the Leidenfrost temperature, T_L , a thin micrometer-scale vapor layer can levitate the droplet and significantly decreases the liquid–solid contact area, shown in Figure 1-4. The vapor layer also serves as a thermal barrier that significantly blocks the heat transfer between the droplet and the surface. Depending on the impact momentum, the drop may bounce, break up, or roll on the wall, further complicating the heat transfer process.

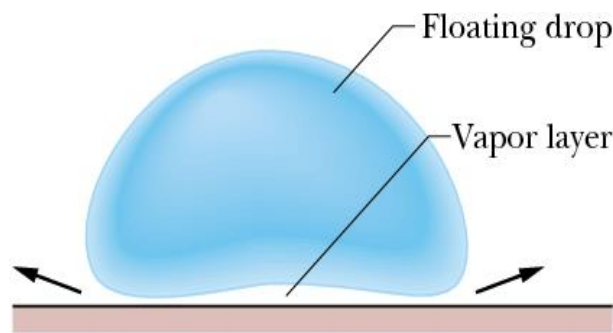


Figure 1-4 Schematic of a Leidenfrost droplet

Since the Leidenfrost effect negatively impacts the liquid cooling efficiency at high wall temperatures, research has been carried out to increase the T_L and delay the transition to the film boiling regime. Micro- and nanostructured surfaces have been widely studied to explore their influence on heat transfer and T_L ¹⁴⁻¹⁹. The static Leidenfrost temperature increases on microstructure-array surfaces with sparse structure spacings, as the pressure in the vapor

decreases thanks to the gaps in the structures and becomes insufficient to support the liquid droplet¹⁴⁻¹⁵. Quantitatively, the static Leidenfrost temperature is found to increase with the effective permeability of the surface, which is a function of the micropillar spacing and height and the excess vapor gap¹⁶. On the other hand, during droplet impact, at a fixed interspacing and pillar width, the dynamic Leidenfrost temperature is found to increase with Weber number, but to decrease with increasing pillar height⁴⁵. Other micro/nanostructured surfaces influence the droplet dynamics through enhanced wettability and wicking, which prevent the droplet from detaching from the surface. Kruse *et al.*¹⁷ used a micro/nanostructured surface fabricated by femtosecond laser processing and increased T_L by up to 175 °C, which was attributed to the reduced contact angle and substantial capillary wicking. A similar observation was also reported on multiscale micro/nano-textured zirconium surfaces⁴⁸. Silicon surfaces covered with carbon-nanofibers delay the transition to film boiling to 200°C higher temperatures compared to smooth surfaces for FC-72 droplets⁴⁹. Combining small-scale structures with other surface designs, a structured surface that consist of small steel pillars, an embedded insulating membrane, and U-shaped channels was created that had a Leidenfrost temperature of 1150°C - a record thus far⁵⁰.

In this dissertation, I study two scenarios that relate to droplet impact on heated surfaces. First, for low-Weber number droplet impact on heated hydrophobic surfaces, I study the local and total heat transfer at the solid-liquid interface during the droplet impact, paying special attention to the distinct bubble entrapment phenomenon. Second, I investigate droplet impact and Leidenfrost dynamics on a heated post, *i.e.*, a surface structure with a similar dimension as the droplet.

1.4 Molten droplet impact

When the substrate temperature is lower than that of the droplet, solidification upon impact can occur, depending on the melting/solidification temperature of the liquid. Molten droplet impact,

which is another form of non-isothermal droplet impact, is of great importance in the development of applications such as thermal spraying⁵¹⁻⁵² and 3D printing^{21, 53}. In contrast to the cold droplet impact on heated surfaces that is accompanied by evaporation, the molten droplet impact on a supercooled surface induces solidification.

Bhola and Chandra⁵⁴ investigated the impact and solidification of molten wax droplets on an aluminum surface and concluded that the extent of droplet solidification is too small to affect droplet impact dynamics. Others⁵⁵ used molten eutectic solder and found that the spreading can be arrested by solidification at the wetting line when the wall temperature is low. Kant *et al.* applied total internal reflection (TIR) microscopy to study the freezing kinetics during water droplet impacting on supercooled surfaces. They found that at a small supercooling temperature, the freezing starts at random locations at the interface; but at a sufficiently high supercooling temperature, solidification initiates near the center of the droplet and propagates to the contact line during droplet spreading.

From a heat transfer perspective, the thermal contact resistance is found to have a great influence on the maximum spreading diameter and solidification thickness development for a molten tin droplet⁵⁶. The interfacial heat transfer coefficient between the melt and the substrate can also be evaluated by matching model calculations with the top splat surface temperature history measured by a fast-response pyrometer⁵⁷. Due to the existence of the liquid-solid interface, the interfacial heat transfer coefficient is much higher in the early contact stage than the later stages of solidification and the solid cooling phase.

In this dissertation, I experimentally study the heat transfer mechanism at the droplet-substrate interface during the molten droplet impact process. The effect of the impact Weber number and surface temperature on heat transfer efficiency are also analyzed.

1.5 Outline of the Dissertation

This dissertation investigates the physical fundamentals of droplet-based two-phase systems, including droplet evaporation, droplet impact on heated surfaces, and molten droplet impact. The dissertation is organized as follows.

In Chapter 2, I will discuss the diffusion confinement of droplet evaporation on a supporting pillar structure. We investigate the diffusion confinement effect imposed by the bottom substrate and the side wall of the micropillar through numerical simulations and experimental investigation. We find that raising the micropillar height from 0 to $2R$, $5R$, and $20R$ led to 26%, 35%, and 42% enhancements, respectively, in the total evaporation rates of hemispherical droplets under isothermal conditions. This improvement is attributed to the diffusion transport in the downward direction that subsequently enhances evaporative transport.

In Chapter 3, I will elaborate on the investigation of low-Weber number droplet impact on heated hydrophobic surfaces in the film evaporation regime. Using synchronized high-speed optical and infrared (IR) imaging, we correlate the droplet dynamics to the spatial distribution of the solid-liquid interfacial temperature, heat flux, and the total heat transfer to the droplet. The total transferred heat of a completely rebounding droplet is also modeled analytically. Denoting the drop diameter and impact velocity as D and v , we find that the total transferred heat Q scales as $D^{1.25}v$, which is validated using experiments. A unique feature of low- We droplet impact on non-wetting surfaces is the formation of a sub-millimetric entrapped bubble that forms during receding. We find that the overall heat transfer is reduced by 5.6% and 7.1% at surface

temperatures of 50°C and 65°C, respectively, as the entrapped bubble reduces the total liquid-solid interface area.

Chapter 4 presents the results of droplet impact and Leidenfrost dynamics on a heated millimetric post. We investigate the droplet lifetime, breakup and boiling modes, as well as the cooling performance of different substrates using high-speed optical and infrared imaging. The post substrate leads to a shorter droplet lifetime and a 20°C higher dynamic Leidenfrost temperature compared to a flat substrate, attributed to mixed boiling modes along the height of the post and additional pinning. For temperatures below the Leidenfrost point, in the nucleate boiling regime, the post substrate also provides a larger maximum temperature drop than its flat counterpart. The enhanced cooling capacity can be attributed to better droplet pinning and an enlarged droplet-substrate contact area. The post's superior cooling performance becomes especially clear for impact on an inclined surface, where the post successfully prevents the rolling and bouncing of the droplet, providing a 51% to 180% increase in the maximum local temperature drop.

Chapter 5 introduces the study on the heat transfer mechanism of molten droplet impact. We experimentally investigate the local heat transfer mechanism during molten paraffin droplet impact using synchronized high-speed optical and infrared imaging. The contact line heat transfer is found to be nearly constant during the spreading process of the droplet impact. A lower substrate temperature increases the overall heat transfer by both higher conduction and solidification heat transfer, while the improvement from a higher impact velocity is only attributed to a larger spreading area. In addition, we also explore the influence of different droplet thermal conductivities by comparing impacting droplets of paraffin wax droplet and

Field's metal. The center region of the metal droplet yields the highest heat flux, which represents a higher local phase change rate.

Finally, in Chapter 6, I will summarize my research and provide insights into future directions for droplet-based two-phase thermal management in fundamental research and industrial applications.

Chapter 2: Investigation of the Confinement Effect on the Evaporation Behavior of a Droplet Pinned on a Micropillar Structure

This chapter is based, in part, on Li, Junhui, *et al.* "Investigation of the confinement effect on the evaporation behavior of a droplet pinned on a micropillar structure." *Journal of colloid and interface science* 555 (2019): 583-594.⁵⁸ and reproduced here with minor modifications.

2.1 Introduction and background

Droplet evaporation is important in many applications such as spray coating⁵⁹⁻⁶¹, inkjet printing⁶²⁻⁶³, fuel injection for spray combustion⁶⁴, bio-sensing⁶⁵, and two-phase heat exchangers^{4-5, 7-8}.

For example, the evaporation of droplets can transport substantial heat across a small temperature gradient, potentially solving cooling challenges in high power electronic systems⁶⁶⁻⁶⁸. However, the practical performance is highly dependent on the intrinsic transport characteristics of the evaporating droplet. For example, the heat transfer performance of 100 μm diameter evaporating droplets is dictated by the vapor diffusion resistance which contributes to more than 85% of the total thermal resistance⁶⁹. A better understanding of the transport characteristics and associated mechanisms of the droplet evaporation process can benefit many practical applications.

As introduced in Chapter 1, the diffusion-limited evaporation mechanism was proposed in the 1890's by Maxwell, who first modeled the liquid evaporation from a spherical bulb that is motionless relative to an infinite uniform medium^{9, 22}. Since then, considerable theoretical analysis has been dedicated to understanding diffusion-dominated transport of droplets during evaporation⁷⁰⁻⁷⁴. Along with these theoretical analyses, the evaporation rates from sessile

droplets have also been quantified by exploring the dynamic behavior of the droplet morphology during the evaporation process^{24-25, 27, 75}. In general, the evaporation behavior of sessile liquid droplets is closely related to the wetting characteristics (represented by the contact angle) and liquid properties, such as the vapor diffusion coefficient and latent heat of vaporization²⁸⁻³¹.

One distinctive feature of sessile droplet evaporation is that the presence of the solid substrate hinders the downward diffusion of vapor molecules and results in a smaller evaporation rate than that of a free droplet⁷⁶⁻⁸¹. Picknett and Bexon first found a reduction in evaporation rate resulting from the presence of the solid substrate below the evaporating droplet²³. They derived an equation to predict the wall effect by defining a capacitance, C , as a function of the contact angle of the spherical cap and the radius of curvature R , i.e., $f(\theta) = 1/2(C/R)$. Since then, different expressions of $f(\theta)$ have been proposed by a variety of studies to describe the evaporation flux from capped spherical droplet as a function of the contact angle³³⁻³⁷. However, all these studies considered only vapor diffusion confinement induced by a semi-infinite planar substrate. For a pinned droplet evaporating on a non-planar substrate, such as one supported on a micropillar structure at a finite height above the bottom substrate, the confinement effect is still poorly understood, because the vapor molecules escaping from the contact line diffuse partially downward, as shown in Figure 2-1. This phenomenon can become more complex if the evaporation proceeds on a heated micropillar, where the vapor concentration becomes nonuniform along the liquid-vapor interface (Figure 2-1).

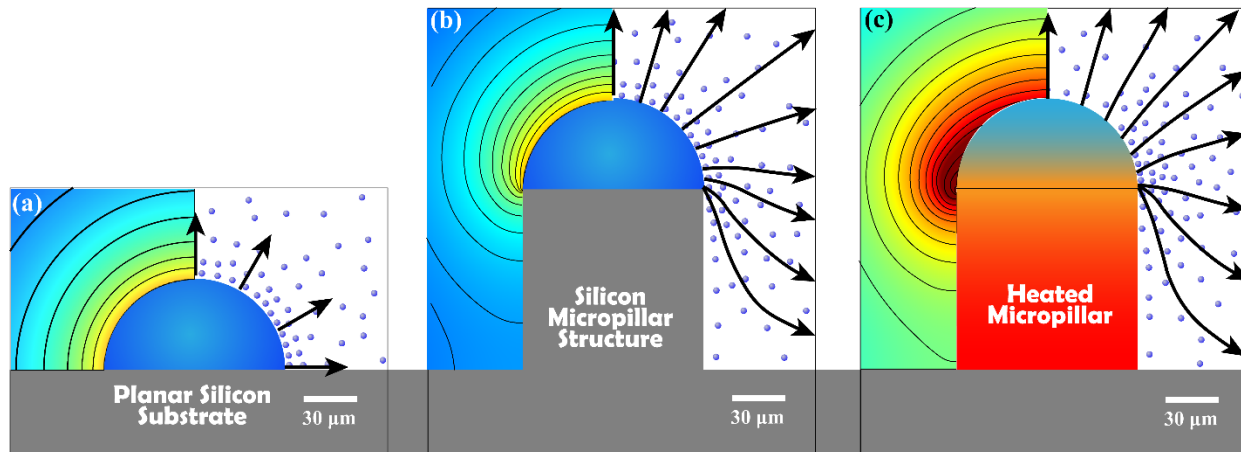


Figure 2-1 Schematic of vapor molecules (blue dots) diffusing away from the liquid-vapor interface for a droplet evaporating on: (a) a flat substrate, (b) a micropillar, and (c) a heated micropillar. Black arrows show the direction of vapor diffusion. The finite height of the micropillar structure enables the vapor molecules to diffuse partially downward, which is prohibited in evaporation on a flat substrate. For a droplet evaporating on a heated micropillar, the high temperature near the contact line will further promote a stronger vapor diffusion rate at the contact region and create a more non-uniform distribution of local evaporation rate along the liquid-vapor interface. For simplicity, the interior channel is not shown, but its effects are included in the numerical model.

We here perform a comprehensive numerical and experimental study to quantify the diffusion confinement effect on the evaporation transport of droplets pinned on porous micropillar structures with different heights, ranging from 0 μm to 1000 μm, in both isothermal and heated substrate conditions. The evaporation from the pinned microdroplet is modeled by coupling the heat conduction inside the droplet and pillar with the vapor diffusion in the ambient air, using the commercial Multiphysics software COMSOL⁸². In particular, the convection current inside the droplet and the ambient air are neglected due to the Peclet number < 1 , Marangoni number < 8000 , and Rayleigh number < 0.03 . Transient evaporation experiments were conducted using fabricated micropillar samples of 6 different heights (0, 50, 75, 100, 125, and 150 μm), which validates the simulation results with a relative error less than 5% in evaporation rate. The results revealed drastic increases in the total evaporation with increasing micropillar height due to the enlarged diffusive space below the droplet. In particular, increasing the height of the micropillar from 0R to 1R and 5R increased the total evaporation rate by 22 % and 37%, respectively. An

approximate solution for the total evaporation rate and local evaporative flux on the suspended droplet is also developed in this study, which yields highly consistent results with the simulation (relative error < 1%). Finally, the evaporation simulation on a heated substrate revealed the existence of optimum micropillar heights at which the evaporation rate is maximized at different temperature conditions. This locally maximized evaporation transport results from competition between increased conduction and reduced diffusion transport resistance with increasing pillar height.

2.2 Simulation Methodology of Droplet Evaporation

An axisymmetric numerical model was developed in the commercial Multiphysics software COMSOL to simulate the evaporation of droplets on a horizontal surface or pinned on top of micropillar structures with various heights. Figure 2-2 shows the geometry of the simulation domain, which consists of a porous micropillar, a capped spherical droplet, and an ambient air domain. The outer diameter of the cylindrical micropillar is 100 μm . Water is supplied to the droplet through a 50 μm diameter channel inside the micropillar. The height of the micropillars is varied from 0 μm to 1000 μm . The ambient air domain is modeled as a hemisphere with a diameter 100 times larger than the diameter of the cylindrical pillar, which ensures that vapor transport from the evaporating droplet is not affected by any boundary effect.

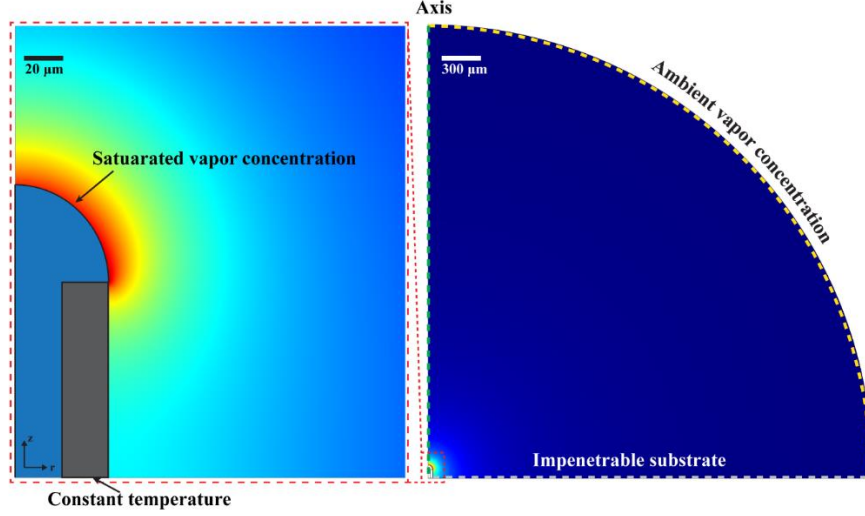


Figure 2-2 Schematic of the computational domain and boundary conditions of the simulation method. For the isothermal condition, only concentration boundary conditions are applied. For the heated condition, a constant temperature boundary condition is further imposed at the bottom surface of the micropillar.

When analyzing the evaporation transport in isothermal conditions, the gas species transport in the ambient domain is described by

$$-\vec{V} \cdot \nabla c_v + \nabla \cdot (D \nabla c_v) = 0. \quad (2.1)$$

In our study, the convection inside the gas domain which originates from two sources: (1) the thermal buoyancy flow induced by the self-cooling effect and (2) the Stefan flow driven by the vapor transport in the gas domain⁸³⁻⁸⁵. However, the strength of both these two flows are very weak for a droplet size of 100 μm. For example, the strength of the thermal buoyancy flow can be described by the Rayleigh number which is found to be less than 0.1 for a droplet on a non-heated micropillar. Such value indicates that natural convection in the gas domain can be neglected. Other studies⁸⁶⁻⁸⁹ have also quantified the importance of the self-cooling effect on an evaporating microdroplet by a dimensionless evaporative cooling number Ec , which characterizes the strength of the thermal convection flow. These studies showed that the critical value for Ec number is 1^{86,90}, while the Ec for a water droplet investigated in our study is only

0.11. Therefore, the self-cooling induced thermal buoyancy flow has little effect on the evaporative heat transfer in our study. Neglecting the advection term for a droplet evaporating on a non-heated pillar and assuming a uniform diffusion coefficient over the ambient environment, the simulation is governed by the Laplace diffusion equation, given by

$$\nabla^2 c_v = 0, \quad (2.2)$$

A constant concentration boundary condition was assigned at the far field, where the concentration was equal to the concentration of vapor in air at 25% relative humidity and 300K. An impenetrable condition (i.e. zero diffusive flux) was assigned to the solid-vapor interfaces, and expressed as

$$\frac{dc_v}{d\vec{n}} = 0. \quad (2.3)$$

Since the droplet size was large enough, the liquid-vapor interfacial pressure was not affected by the curvature of the droplet⁹¹. Therefore, the concentration at the liquid-vapor interface was assumed to be equivalent to the saturation concentration, i.e.,

$$c_{v,lv} = c_{sat}(T_{lv}), \quad (2.4)$$

where c_{sat} is the saturated vapor concentration which can be found from a thermodynamic table⁹². When analyzing the evaporation behavior of the microdroplet, the energy transport equation for the droplet and silicon micropillar was incorporated in the simulation model and coupled with the diffusion model through energy conservation and temperature continuity at the liquid-vapor interface. In the liquid domain, heat is transported by both the convection and conduction. Convection includes the continuous inlet flow from the center pore, convection due to buoyance inside the droplet, and Marangoni convection inside the droplet. The convection magnitudes

from each of the three sources were calculated using the Péclet number, Rayleigh number, and Marangoni number for the flow field, respectively. In this study, the Péclet number and Rayleigh number were found to be sufficiently small. The theoretically calculated Marangoni number, however, is found to often overpredict the Marangoni strength in experiments by 100 times for water droplets⁹³⁻⁹⁴. Moreover, other studies have shown that the effect of Marangoni flow on evaporation is negligible for droplets with volume larger than 1 nL^{91,95}. As a result, the convective heat transfer inside the droplet plays an insignificant role compared to conduction and thus can be neglected. Consequently, the heat transfer in the liquid and solid domains is governed by the conduction equation:

$$\nabla^2 T = 0, \quad (2.5)$$

where T is the continuous temperature function in both the liquid and solid domain. In the simulation, an isothermal boundary condition was assigned to the base surface of the micropillar. At the liquid-vapor interface, a heat flux thermal boundary condition was imposed to satisfy the energy conservation between conduction and evaporative transport:

$$k_l \left(\frac{\partial T}{\partial \vec{n}} \right)_{lv} = D h_{fg} \left(\frac{\partial c_v}{\partial \vec{n}} \right)_{lv}, \quad (2.6)$$

where k_l is the thermal conductivity of water, h_{fg} is the latent heat of vaporization, D is the air-vapor molecular diffusion coefficient, and c_v is the vapor concentration at the liquid-vapor interface. The left term in equation (7) represents the conduction heat flux at the liquid-vapor interface, while the right term represents the evaporation heat transfer at the interface. When evaporation proceeds at ambient pressure, the interfacial resistance is usually much smaller than the diffusion resistance and therefore is neglected in this study⁹⁶. In addition, no radiation heat

transfer was considered in the process due to the negligible effect compared to the conduction and convection heat transfer.

In the actual simulation, a converged concentration and temperature field are obtained by solving the species transport equation and heat conduction equation iteratively through a finite number of cycles. The specific settings in the numerical study are summarised in Table 2-1, including the geometric details, material properties, and solution method in the software. The geometric parameters were kept the same as for the fabricated samples.

In this study, unstructured triangular meshes were generated by COMSOL Multiphysics® with a higher density near the liquid-air interface. A mesh-independent study was conducted at four different mesh sizes for droplet evaporation without the presence of the pillar structure. The simulation model is validated using the analytical model of droplet evaporation on a flat substrate proposed by Popov⁹⁷. The difference between the results obtained from the numerical simulation and Popov model is less than 10%, which suggests that the numerical model developed in this study is accurate and reliable.

Table 2-1 Simulation setup

Input parameters	Value
Outer diameter, D_{pillar}	100 μm
Inner diameter, d	50 μm
Perimeter, L	3.14×10^{-4} m
Operating pressure, p_{amb}	101325 Pa
Operating relative humidity, ϕ_{∞}	25%
Properties	Water

Surface tension, σ	7.3×10^{-2} N/m		
Equilibrium contact angle, θ_e	23°		
Solution methods	Setup		
Mesh type	Triangular		
Number of cells	$\bar{h} = 0$	$\bar{h} = 5$	$\bar{h} = 20$
	120013	319529	723451
Study type	Stationary		
Solver	PARDISO		
Preordering algorithm	Nested dissection multithreaded		
Relative tolerance	1.0×10^{-6}		

2.3 Results and discussions

2.3.1 Isothermal evaporation in room temperature

Figure 2-3 shows the iso-concentration contours and the local diffusion flux vectors for droplets evaporating on pillars with heights between 0 to $2R$. With a zero height, the magnitude of the diffusion flux is constant along the liquid-vapor interface. However, with a finite pillar height, the iso-concentration line close to the liquid-vapor interface must end on the side wall of the pillar in the horizontal direction in order to satisfy the impenetrable boundary condition. This geometric constraint results in a sharp bending of the iso-concentration line near the contact line region, creating a high local concentration gradient and therefore a strong local diffusion flux near the contact line region.

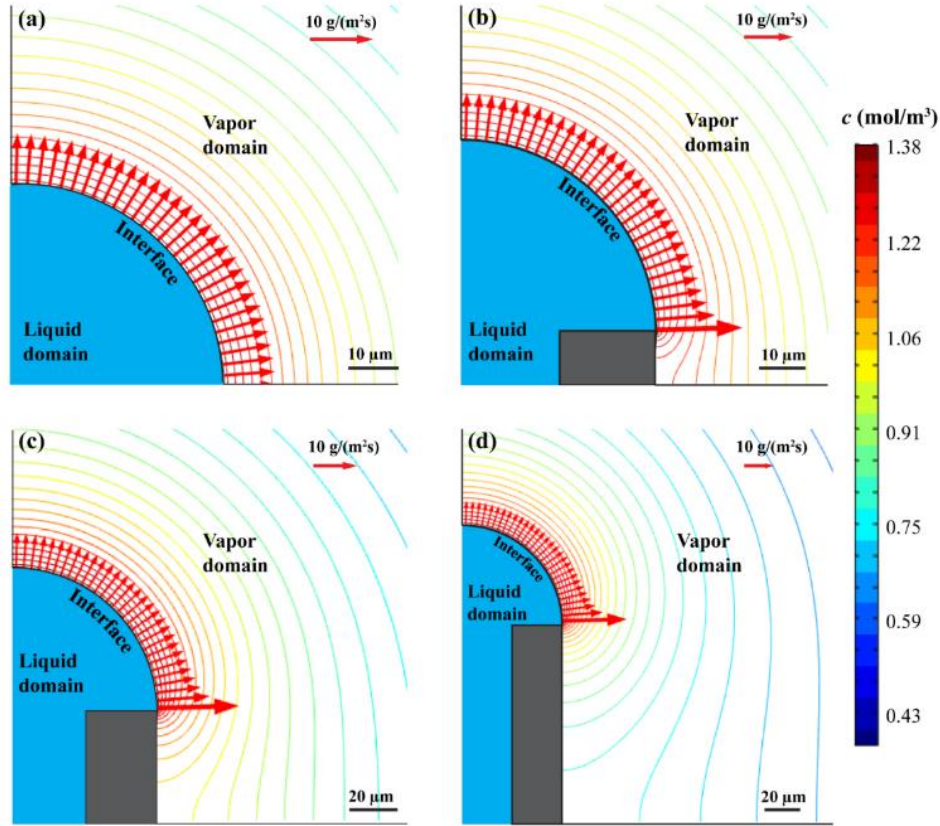


Figure 2-3 The iso-concentration contour with the vector plot of local evaporative flux J , along the liquid-air interface at four different pillar heights: (a) $0R$, (b) $0.25R$, (c) $0.75R$ and (d) $2R$. The concentration of the vapor domain is represented by the different colored contour lines. The length and the direction of the red arrow represents the magnitude and the direction vector of the evaporative flux.

2.3.2 Approximate solution of droplet evaporation atop a pillar structure under isothermal conditions

An approximate solution for the evaporation rate of a hemispherical droplet on a pillar can be established based on the solution on an infinite flat substrate. Such a solution was first proposed by Maxwell²², who analyzed the vapor transport from a spherical wet bulb thermometer. The evaporation rate for a hemispherical droplet is expressed as

$$\dot{m} = 2\pi RDM(c_s - c_\infty), \quad (2.7)$$

where c_s is the concentration of the saturated vapor just above the liquid-air interface, c_∞ is the ambient vapor concentration, R is the diameter of the liquid-solid interface, and D is the

diffusion coefficient for vapor in air. For a pillar with a finite height h , the evaporation rate will be enhanced due to the attenuated diffusion hindrance caused by the bottom substrate. To describe this behavior, a correction function $a(\bar{h})$ can be included to account for the enhanced evaporation caused by increasing pillar height:

$$\dot{m} = a(\bar{h})\dot{m}_{\bar{h}=0}, \quad (2.8)$$

where $\bar{h} = h/R$ is the nondimensional pillar height and $\dot{m}_{\bar{h}=0}$ is the total evaporation rate without pillar structure. According to the total evaporation rates obtained from numerical simulations with different pillar heights, the correction function $a(\bar{h})$ can be approximated by non-linear regression fitting as

$$a(\bar{h}) = -\frac{0.44}{1 + \bar{h}} + 1.44. \quad (2.9)$$

Based on the previous results, the total evaporation rate can be expressed as

$$\dot{m} = 2\pi a(\bar{h})DRM(c_s - c_\infty). \quad (2.10)$$

Substituting equation (6) into (7) yields the complete approximate solution of total evaporation rate:

$$\dot{m}(\bar{h}) = 2\pi \left(1.44 - \frac{0.44}{1 + \bar{h}}\right) DRM(c_s - c_\infty). \quad (2.11)$$

Figure 2-4 shows the comparison between the total evaporation rates obtained from numerical simulations and those predicted by the approximate solution. Excellent agreement (<1% difference) is found between these results. When $\bar{h} < 10$, the evaporation rate increases rapidly with increasing \bar{h} , due to attenuation of the diffusion confinement. For $\bar{h} > 20$, the evaporation

rate increases much slower and eventually approaches a plateau. Therefore, the confinement effect can be considered to vanish at a pillar height of $20R$, and any further increase in the distance between the droplet and substrate does not affect the concentration gradient near the droplet significantly.

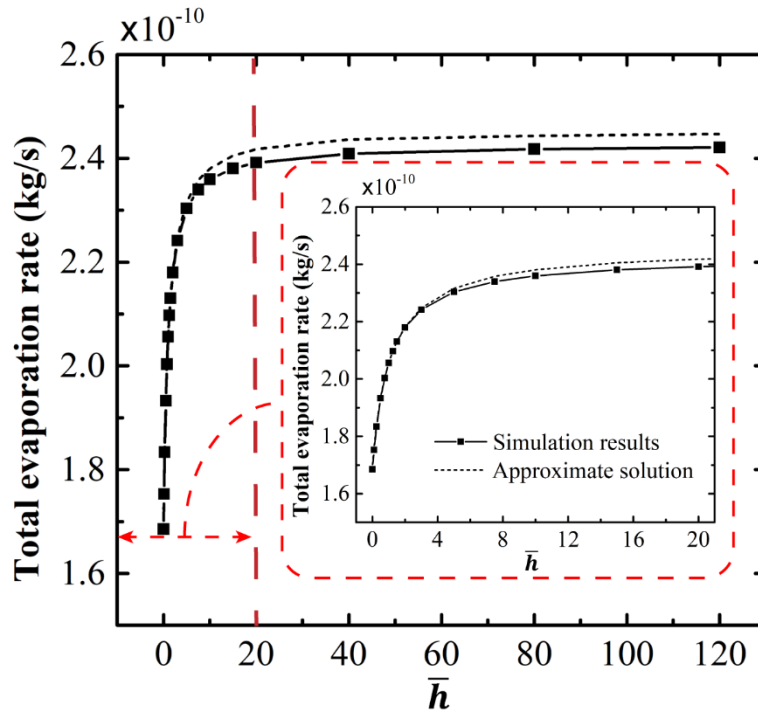


Figure 2-4 Simulation results and the approximate solution for the total evaporation rate \dot{m} , at different pillar heights. The horizontal axis value $\bar{h} = r/R$ represents the nondimensional pillar height.

A correction factor can also be developed to describe the distribution of the local evaporation flux along the liquid vapor interface at different pillar heights. For a hemispherical droplet evaporating on a flat substrate, the local evaporative flux along the droplet surface is uniform and given by

$$J = \frac{\pi DM(c_s - c_\infty)}{R}, \quad (2.12)$$

An extra term, $f_h(\alpha, \bar{h})$, describing the reduction in vapor diffusion confinement with increasing pillar height can be imposed in toroidal coordinates at $\theta = 90^\circ$:

$$J(\alpha) = \frac{\pi DM(c_s - c_\infty)}{R} f_h(\alpha, \bar{h}), \quad (2.13)$$

where the toroidal coordinate α is uniquely related to the polar coordinate r on the surface of the drop by,

$$r = \frac{R \sinh \alpha}{\cosh \alpha + \cos \theta}. \quad (2.14)$$

Using a smooth surface fit (by the MATLAB curve fitting tools), the value of $f_h(\alpha, \bar{h})$ can be imposed.

2.3.3 The combined effects from contact angle and pillar height on vapor diffusion confinement

The diffusive mass transport of an evaporating droplet is also highly dependent on the contact angle of the droplet, as discussed in previous studies^{28-31, 97-99}. For example, Deegan *et al.* provided an approximated analytical solution for the evaporation rate of droplets with spherical caps as a function of their intrinsic contact angle⁹⁸. Popov⁹⁷ extended the work by Deegan and calculated the local and total mass transport rates valid for all contact angles, in which higher evaporation near the contact line is observed for contact angles smaller than 90° . To capture the combined effects of the contact angle and micropillar height on the diffusion transport behavior of an evaporation droplet, we further model the evaporation behavior of droplets with different contact angles on micropillars with different heights, following the procedures described earlier. Figure 2-5 (a) shows five distributions of evaporative flux along the liquid-vapor interface when

the height is zero. From the top center point ($l^* = 0$) of the capped spherical droplet to the contact line ($l^* = 1$), the arc length is normalized with respect to the maximum arc length by

$$l^* = \frac{l_{\text{local}}}{l_{\text{max}}}. \quad (2.15)$$

The local evaporative flux is normalized with respect to the local evaporation flux at the top center point of the capped spherical droplet (i.e., $l_{\text{local}} = 0$):

$$J^* = \frac{J}{J_{l^*=0}}. \quad (2.16)$$

For a contact angle of 90° , the evaporative flux along the droplet surface is uniform. In this case, the evaporation process can be treated as a 1-dimensional problem since the vapor distribution remains constant for different radial directions. For a contact angle greater than 90° , the evaporative flux decreases near the contact line region. Due to the presence of the substrate, a large contact angle results in a small region for vapor diffusion at the contact line, which reduces the concentration gradient and the local evaporative flux. For a contact angle smaller than 90° , the evaporation near the contact line region is enhanced by the large space available for vapor diffusion. In this case, the substrate enhances the vapor diffusion rather than confining it. Therefore, the confinement on the vapor diffusion transport by a flat solid substrate is present only for contact angles greater than 90° and is intensified by increasing contact angle.

Figure 2-5 (b-d) shows the simulation results for vapor diffusion rates along the liquid-air interface at different contact angles and non-zero pillar heights. For all conditions, an increased contact angle substantially reduces in the evaporation rate at different arc length locations, due to the stronger confinement of vapor diffusion. For a contact angle smaller than 90° , both the

contact angle and pillar height provide positive impacts that promote stronger vapor diffusive transport near the contact region. Therefore, a monotonically increasing diffusion rate along the droplet interface is found for all pillar heights. For a contact angle greater than 90° , however, it is interesting to notice that the local diffusion does not follow a monotonically decreasing trend, as shown in Figure 2-5 (a). This behavior is caused by the competing effects of the contact angle and pillar height on the vapor diffusion transport. A larger contact angle results in stronger vapor diffusion confinement by the substrate near the contact line region, since the direction of the vapor diffusion near the contact line is oriented more downward.

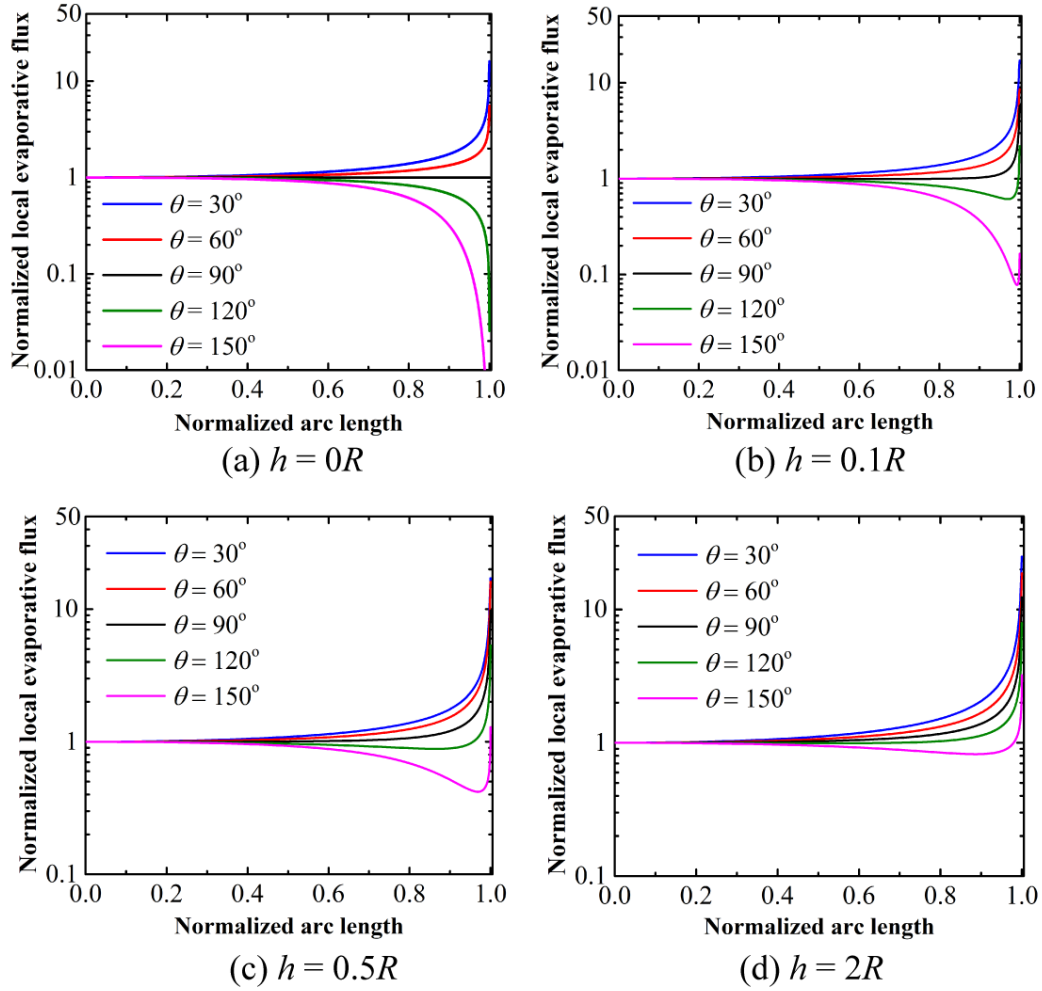


Figure 2-5 Simulation results for local evaporation rates along the liquid-air interface at different pillar heights (a) $0R$, (b) $0.1R$, (c) $0.5R$, and (d) $2R$ with different contact angles.

An approximated solution for the diffusive mass transport rate can also be developed to describe the combined effects of the contact angle and pillar height on diffusion transport. Consider an evaporating droplet with an arbitrary contact angle θ on a flat substrate, the local evaporative flux has been derived by Popov as

$$J(\alpha) = \frac{DM(c_s - c_\infty)}{R} f(\theta), \quad (2.17)$$

and $f(\theta)$ is a term accounting for the diffusion confinement by the contact angle, given by

$$f(\theta) = \frac{1}{2} \sin \theta + \sqrt{2}(\cosh \alpha + \cos \theta)^{\frac{3}{2}} \times \int_0^{\infty} \frac{\cosh(\theta\tau)}{\cosh(\pi\tau)} \tanh[(\pi - \theta)\tau] P_{-1/2+i\tau}(\cosh \alpha) \tau d\tau. \quad (2.18)$$

The $f(\theta)$ term can be added to equation (10) directly to describe the distribution of evaporative flux for droplets with varied contact angles and pinned on pillars with varied heights, since the contact angle and pillar height provide independent effects on the vapor diffusion confinement. In this case, the local evaporative flux in a toroidal coordinate system considering the impacts from the changes in both contact angle and pillar height, can be expressed as

$$J(\alpha) = \frac{\pi DM(c_s - c_\infty)}{R} f_h(\alpha, \bar{h}) f(\theta). \quad (2.19)$$

Similarly, the approximated solution of the total evaporation rate, shown in equation (8), can also be modified to take the contact angle impact into consideration as:

$$\dot{m} = -\pi RDM(c_s - c_\infty) \left(1.44 - \frac{0.44}{1 + \bar{h}} \right) \left[\frac{\sin \theta}{1 + \cos \theta} + 4 \int_0^{\infty} \frac{1 + \cosh 2\theta\tau}{\cosh 2\pi\tau} \tanh[(\pi - \theta)\tau] d\tau \right]. \quad (2.20)$$

2.4 The effect of micropillar height on vapor diffusion confinement for droplet evaporation on heated substrate

Adding a heat source can significantly alter the distribution of the local vapor diffusion rates. For example, Gleason *et al.* showed that the inherent decreasing trend of the local diffusion rate from the center to the contact line of an evaporating droplet with a contact angle greater than 90° can be reversed when heat is applied beneath the droplet⁸¹. To explore how the vapor diffusion

confinement is affected by different heating conditions, we investigate the evaporation behavior of droplets on heated micropillars of different heights. Specifically, constant temperature boundary conditions of $T_{sub} = 60^\circ\text{C}$, 80°C , and 98°C are imposed on the bottom surface of the pillar to simulate droplet evaporation on heated substrates. In addition, considering that both the thermal buoyancy flow and Stefan flow become stronger with increasing heat flux, the convective flow is included in the gas domain by incorporating the following continuity, momentum, and energy equations in the simulation

$$\nabla \cdot (\rho \mathbf{u}) = 0 \quad (2.21)$$

$$\rho(\mathbf{u} \cdot \nabla) \mathbf{u} = \nabla \cdot \left[-\rho \mathbf{I} + \mu[\nabla \mathbf{u} + (\nabla \mathbf{u})^T] - \frac{2}{3} \mu(\nabla \cdot \mathbf{u}) \mathbf{I} \right] + \rho \mathbf{g} \quad (2.22)$$

$$\rho c_p \mathbf{u} \cdot \nabla T - \nabla \cdot (k \nabla T) = \rho c_p \frac{\partial T}{\partial t} \quad (2.23)$$

The liquid-vapor interfacial temperature solved inside the droplet is used as the boundary condition for solving the temperature in the gas domain. The velocity boundary condition at the liquid-vapor interface in the gas domain is given by ¹⁰⁰:

$$\vec{V}_n = \frac{1}{C_{air}} \cdot D \frac{\partial C_{air}}{\partial n} = -\frac{1}{C_g - C_v} \cdot D \frac{\partial C_v}{\partial n} \quad (2.24)$$

In the simulation, the thermal buoyancy flow is taken into consideration by setting the air density as a function of the local temperature solved by the heat transfer model. The same gas species transport model described by Eq. (2.24) and the same boundary conditions are used to solve vapor transport. However, Eq. (2.24) incorporates the velocity field calculated in the gas domain.

Figure 2-6 shows the simulated evaporation rates of droplets on micropillars with different heights for three different substrate temperatures. Contrary to the monotonic increasing trend shown in Figure 2-4, the total evaporation rate was found to increase first and decrease later with increasing pillar height substrate temperatures. Specifically, for substrate temperatures 60°C, 80°C, and 98°C, the pillar heights yielding the largest evaporation rate are $\bar{h} = 5.5$, $\bar{h} = 3$, and $\bar{h} = 0$, respectively. The decrease in the evaporation rate after reaching a certain pillar height is attributed to an increase in the conduction resistance as the micropillar becomes taller. As shown in Figure 2-6, the improvement in the diffusion mass transport caused by increasing pillar height becomes less significant when the pillar height is sufficiently large. However, the conduction resistance along the micropillar keeps increasing linearly with increasing pillar height. Therefore, as the attenuation of vapor diffusion confinement becomes insignificant at higher pillar heights, evaporative transport becomes dominated by the increase in conduction resistance. Finally, for substrate temperature of 98°C, the decrease of the diffusion resistance is less than the increase of conduction resistance as pillar height becomes larger.

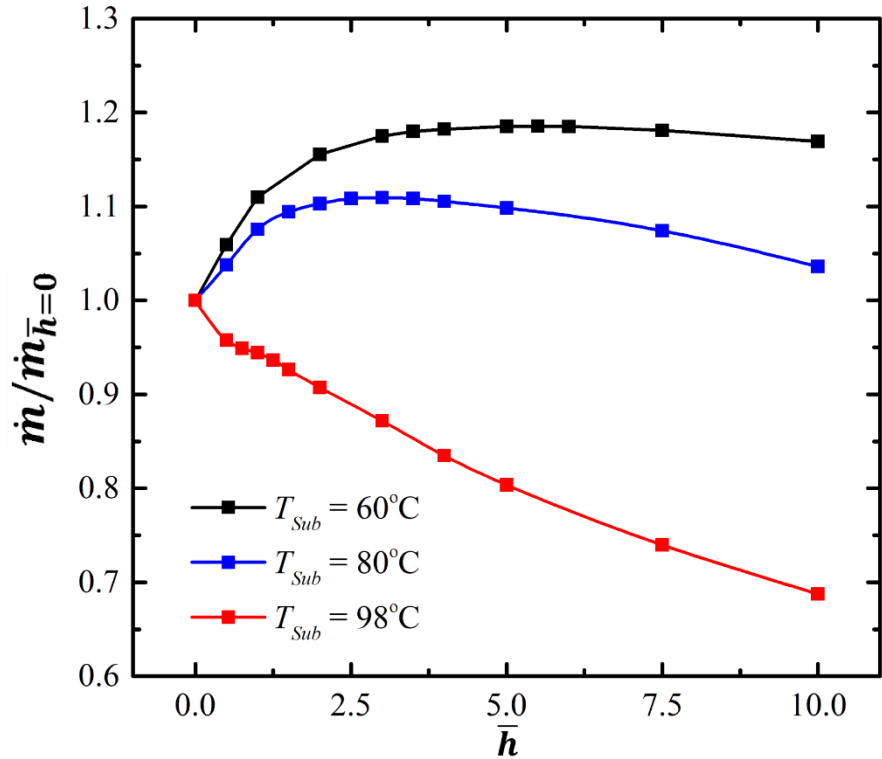


Figure 2-6 Simulation results of evaporation rates on various pillar heights at three different substrate temperatures 60°C, 80°C, and 98°C. The evaporation rates for different pillar heights are normalized with respect to the evaporation rate for a pillar height of zero. For substrate temperatures of 60°C, 80°C, and 98°C, the largest evaporation rates occur at pillar heights of $\bar{h} = 5.5$, $\bar{h} = 3$, and $\bar{h} = 0$, respectively. As the substrate temperature increases, the evaporation rate decreases faster as it exceeds the maximum value, which indicates that a conductive resistance is more critical at higher temperature condition.

2.5 Experimental Validation

To validate the numerical simulation, the evaporation rates of water droplets supported on micropillar structures with different heights are measured experimentally. Figure 2-7 shows droplets evaporating over time on four micropillars with a height of $0R$, $1R$, $1.5R$, and $2R$. The volume of the droplet evaporating on the micropillar with a height of $2R$ shrinks the fastest, i.e., it exhibits the largest evaporation rate. By contrast, the droplet evaporating on the flat substrate (i.e., $h = 0R$) experiences the smallest change over the same time. These observations are consistent with our numerical analysis, discussed in section 2.3.3. To quantify the evaporation rate, we measure the maximum height of the droplet in the image sequence and calculate the corresponding change in droplet volume by

$$V = \frac{\pi}{6}h(3r^2 + h^2), \quad (26)$$

where r is the outer radius of the micropillar, and h is the instantaneous height of the droplet. The instantaneous evaporation rate is then calculated by taking the derivative of the droplet volume over time. The resulting evaporation rates of the droplets at a contact angle of 90° are shown in Figure 2-8 together with the numerical predictions obtained from Section 2.3. The experimental measurements of evaporation rates are in excellent agreement with the simulation result, with a maximum error of less than 5%. Therefore, the numerical results obtained are validated as reliable.

For droplet evaporation on a heated substrate, a validation experiment is performed for a pillar height of $112 \mu\text{m}$ and a steady droplet shape with a contact angle of 72° at different substrate temperatures. The geometric features of the droplet and the pillar used in simulation are the same as in the experimental test. The total evaporation rates acquired numerically and experimentally are shown in Table 2-2. The maximum difference between the experimental data and simulation result is within 24% which only occur at the highest substrate temperature. This is attributed to the numerical model neglecting the conduction through the base substrate (i.e., the temperature measured by the resistance temperature detector (RTD) sensor is different from the temperature at the base of the pillar) and the evaporation interfacial resistance between the liquid and air domain. Therefore, the interfacial vapor temperature can be over-predicted by $\sim 6^\circ\text{C}$ at 98°C , which yields $\sim 20\%$ higher vapor diffusion rate.

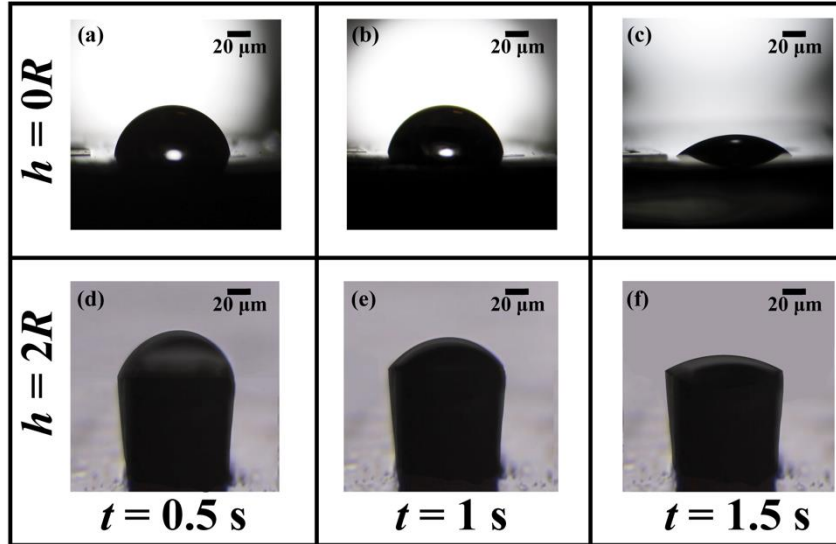


Figure 2-7 Photographs of evaporating droplets on two different micropillars, taken at three different times. Both droplets have the same contact diameter. The droplet evaporating on the micropillar with a height of $2R$ shrinks faster over time, while the droplet evaporating on a flat substrate (i.e., $h = 0R$) experiences a smaller change over the same time period. Thus, the evaporation rate of a supported droplet increases with increasing pillar height.

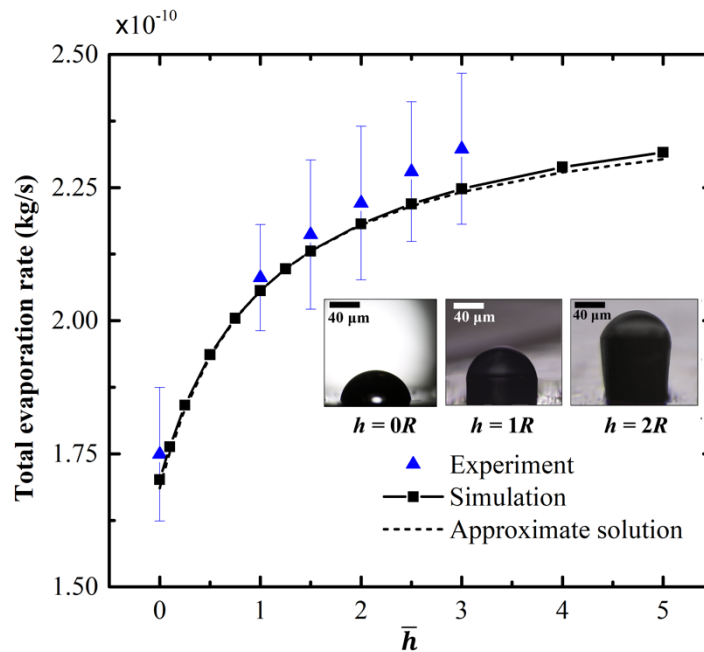


Figure 2-8 Total evaporation rates from experimental data, simulation results, and the approximate solution for isothermal evaporation at different pillar heights. Images are taken from the video of the evaporation process where the contact angle equals 90° . The simulation results match the experimental data within 5%. The maximum difference occurs at a pillar height of $150\ \mu\text{m}$ ($\bar{h} = 3$).

Table 2-2 Total evaporation rates at different substrate temperatures

Substrate temperature (°C)	Total evaporation rate by experiment ($\times 10^{-9}$ kg/s)	Total evaporation rate by simulation ($\times 10^{-9}$ kg/s)
60	0.94 ± 0.17	1.05
70	1.39 ± 0.17	1.58
80	2.00 ± 0.17	2.32
90	3.00 ± 0.17	3.41
98	4.10 ± 0.17	5.09

2.6 Conclusion

In this chapter, we explored the evaporation behavior of a droplet pinned on a micropillar structure. A multiphase numerical model was developed in COMSOL® to simulate the evaporative transport from microdroplets supported on micropillar structures with varying heights, in both isothermal and substrate-heated conditions. The numerical results were further validated by experimental measurements of the evaporation rate performed under the same environmental conditions. The results demonstrate that increasing micropillar height can reduce the vapor diffusion confinement on the evaporating droplet which is reflected by both a higher local and higher total evaporation rate. Specifically, raising the micropillar height from 0 to $2R$, $5R$, and $20R$ led to 26%, 35%, and 42% enhancement, respectively, in the total evaporation rate of a hemispherical droplet under an isothermal condition. In addition, we found that the confinement of vapor diffusion at the contact line for droplets with a contact angle greater than 90° is alleviated with increasing pillar height due to the greater vapor diffusion space available beneath the droplet. When the pillar height is sufficiently large (e.g., $h > 20R$), the local evaporation rate increases from the top center to the contact line region of these large droplets, contrary to the trend observed for the evaporation of large droplets on a flat substrate. With these findings, we further developed a closed-form expression for the total and local evaporation rate

of droplets as a function of the contact angle θ and the normalized pillar height $\bar{h} = h/R$. This expression was developed by incorporating a correction factor term to the analytical solution of droplet evaporation proposed by Popov⁹⁷. Compared to the past studies only focusing on the vapor diffusion confinement effect of a droplet evaporating on a planar substrate^{23, 27, 36-37, 81, 98-99, 101-104}, our expression provides a simple and elegant way to predict the relationship between the evaporation transport behavior of a droplet on a non-planar surface and pillar as a function of the height of the micropillar structure. For droplets evaporating on heated micropillars, we found that evaporation transport was affected by a competition between the effect of increasing conduction resistance and reduced vapor diffusion confinement as the pillar height increased. Thus, with increasing pillar height, the total evaporation rate first increases and later decreases (except for a substrate temperature of 98°C). Specifically, for substrate temperatures 60°C, 80°C, and 98°C, the pillar heights providing the largest evaporation rates are $\bar{h} = 5.5$, $\bar{h} = 3$ and $\bar{h} = 0$, respectively. In summary, this study provides a quantitative analysis of the diffusion-limited evaporation transport of a supported droplet, which is affected by the pillar height, contact angle, and heating conditions. The analysis and the approximated solutions presented here can help researchers understand the more complex transport physics involved in droplet evaporation on non-planar substrates in a variety of practical scenarios.

Chapter 3: Low Weber Number Droplet Impact on Heated Hydrophobic Surfaces

This chapter is based, in part, on the following manuscript and reproduced here with minor modifications: Li, Junhui, and Patricia B. Weisensee. "Low Weber number droplet impact on heated hydrophobic surfaces." *Experimental Thermal and Fluid Science* 130 (2022): 110503.¹⁰⁵.

3.1 Introduction

Research of droplets impacting heated surfaces is motivated by various applications such as spray cooling^{40, 106}, internal combustion engines¹⁰⁷⁻¹⁰⁸, and horizontal-tube falling film evaporation in desalination and refrigeration¹⁰⁹. During this process, the wall temperature and the impact Weber number, which compares the relative importance of inertia and surface tension forces, are the two most important parameters governing the impact behavior (i.e., droplet hydrodynamics) and heat transfer¹¹⁰. Although many studies investigated the droplet impact with high wall temperature conditions in the nucleate boiling and Leidenfrost regime^{45, 111-114}, only few have examined wall temperatures lower than the boiling point, i.e., in the film evaporation regime^{41, 115}.

During non-isothermal droplet impact, the total heat transfer is composed of the conduction, convection, and partial evaporation of the liquid^{10, 116}. Pasandideh-Fard *et al.*⁴⁰ proposed a quantitative measurement of droplet cooling, namely the cooling effectiveness, relating the actual heat transfer to the maximum possible heat transfer. They investigated water droplets impacting a hydrophobic surface and found the cooling effectiveness to increase with the Weber number. Herbert *et al.*¹¹ concluded that conduction and convection heat transfer at the liquid-solid interface dominate the total heat transfer during spreading, while at the maximum spreading and the following receding stage, a certain amount of the total heat transfer can be attributed to

evaporation. Others used infrared (IR) thermography to study droplets impacting superhydrophobic surfaces⁴¹⁻⁴². The total heat transfer on micro-structured and nano-textured superhydrophobic surfaces was found to be much smaller than on smooth or sticky surfaces.

During droplet impact, the local heat transfer can be experimentally inferred from the temporal evolution of the temperature distribution of the droplet-substrate interface using high-speed IR thermography^{11, 117-118} or using high-fidelity numerical simulation methods^{41, 119-120}. The area near the triple-phase contact line between the liquid, substrate, and surrounding air, has a much higher local heat flux than the other regions of the liquid-solid interface due to the existence of evaporation^{118, 121}. The magnitude of the local heat flux near the triple-phase contact line depends on the direction of the moving contact line (advancing or receding) and its velocity¹²²⁻¹²³. Kunkelmann *et al.*¹²¹ explored the local heat flux of a detaching bubble during pool boiling and found that the contact line heat flux changes linearly with the contact line velocity for an advancing contact line, while it remains constant for a receding contact line. For impacting FC-72 droplets, on the other hand, the advancing contact line heat flux was found to increase quadratically with the contact line velocity¹¹. Our understanding of the contact line heat transfer during receding, however, is insufficient due to the small receding distances and velocities of the contact line of (partially) wetting droplets. It is unclear to which extent the contact line heat flux is affected by a completely rebounding (bouncing) droplet. One can expect that a fully receding contact line has a lower heat flux as it moves over a pre-cooled and wetted surface (in contrast to an advancing contact line, which moves over a heated surface).

During receding, the total contact line length can be artificially increased, for example, through the formation of satellite droplets during droplet impact on wettability-patterned surfaces¹²⁴⁻¹²⁵. Moreover, entrapped bubbles can generate a secondary internal contact line during the droplet

impact on hydrophobic or superhydrophobic surfaces. A sub-millimetric entrapped bubble can be observed within the droplet for a specific range of low Weber numbers¹²⁶⁻¹²⁹. Distinct from the microscopic impact bubble that occurs during the early stages of spreading¹³⁰⁻¹³¹, the entrapped bubble forms during the receding stage and can either be attached to the solid substrate or floating within the droplet. Bartolo *et al.*¹²⁶ first reported the formation of the entrapped bubble inside an impacting droplet on a superhydrophobic surface. Hung *et al.*¹²⁷ identified the impact velocity and droplet size range for bubble occurrence for droplets impinging on parafilm surfaces. Chen *et al.*¹²⁸ examined the bubble occurrence for ten different solid surfaces with water contact angles of 40–161° and concluded that the bubble entrapment occurs only on sufficiently hydrophobic surfaces ($\theta_{eq} \geq 103^\circ$) within a narrow range of impact velocities. However, most of the previous bubble entrapment studies considered an isothermal condition where the heat transfer is negligible. It is unknown about the bubble entrapment during non-isothermal droplet impact and its effect on the heat transfer efficiency. The trapped air bubble is expected to significantly influence the heat transfer due to its higher thermal resistance and the presence of a secondary triple-phase contact line. Furthermore, while beyond the scope of this study, the existence of an entrapped air bubble for impact on cooled surfaces could greatly reduce the adhesion after solidification – for the better (*e.g.*, anti-icing surfaces¹³²⁻¹³⁴) or the worse (*e.g.*, droplet-based additive manufacturing¹³⁵⁻¹³⁶).

In this study, the coupling of hydrodynamics and heat transfer during low Weber number droplet impact on heated hydrophobic surfaces is investigated experimentally using synchronized high-speed optical and infrared (IR) imaging. The overall and local heat transfer, especially near the contact line region(s), is explored for droplet impact on smooth hydrophobic surfaces. A scaling law for the total heat transfer is proposed based on an analytical derivation and experimental

validation. Correlating droplet dynamics to the spatial distribution of the solid-liquid interfacial temperature and heat flux, we analyze the evolution of the entrapped bubble and its influence on the local and total heat transfer. In addition, we quantify the effect of surface roughness on the total heat transfer based on the result from two surfaces with different roughness. This study can provide new insights into the fundamentals of the transient phase-change heat transfer processes and its applications.

3.2 Experimental methods

3.2.1 Sample fabrication

The sample fabrication process, including heater design and the application of the smooth hydrophobic coating, is shown in Figure 3-1. First, two copper sheets were attached to opposing ends of an IR-transparent calcium fluoride substrate (UQG Optics, 25.4 mm × 25.4 mm × 1.18 mm). Then, a 4 μm thin layer of black paint (SPB 100), which serves as a transducer for the thermal imaging, was spin-coated for 90 s at 600 rpm onto the CaF₂ substrate. The thickness of the black paint layer was measured using a profilometer (Alpha-Step D-100 Stylus Profiler). On top of the black paint layer, a 150 nm thin chromium film was deposited using thermal evaporation, serving as a heater (effective heater area: 16.5 mm × 25.5 mm). The two copper sheets served as voltage transducers between the power supply (Instek PSW 160-7.2) and the Cr heater to achieve uniform heating. A 100 nm thin layer of Teflon AF was then spin-coated on the Cr layer using 1% Teflon AF 1601 solution with a spin time of 30 s at 2000 rpm and exhibits good adhesion. The equivalent, advancing, and receding contact angles of the Teflon AF surface are $\theta_{eq} = 115^\circ \pm 2^\circ$, $\theta_{ad} = 126^\circ \pm 2^\circ$, and $\theta_{re} = 111^\circ \pm 2^\circ$, respectively.

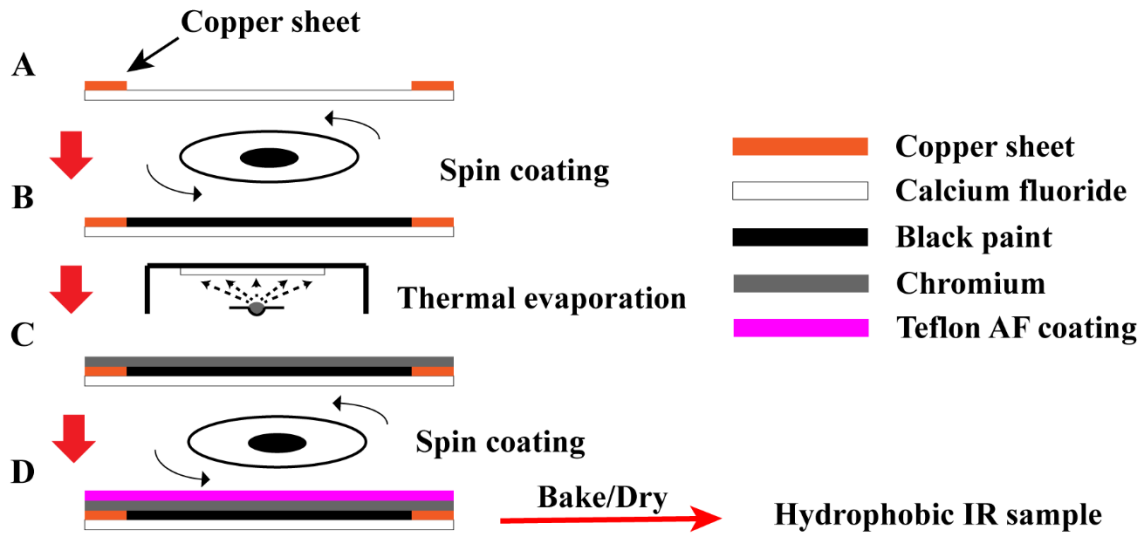


Figure 3-1 Schematic of the heater design and fabrication process of the smooth hydrophobic IR-transparent sample

3.2.2 Experimental setup

The experimental approach is similar to that of a previous study of our group¹²⁴, and a schematic of the experimental setup is shown in Figure 3-2. The side-view shadowgraph images of the impacting droplets were recorded at 10,000 frames per second (fps) using a Photron Mini AX200 high-speed camera with a Canon MP-E 65mm f/2.8 1-5X Macro Lens at a spatial resolution of 3.3 $\mu\text{m}/\text{pixel}$. A Telops FAST M3k high-speed mid-wave IR camera, equipped with a 1x long working-distance lens (Telops), recorded the thermal signals of the samples in bottom-view at 5,000 fps with a spatial resolution of 30 $\mu\text{m}/\text{pixel}$. Note that we measure the temperature distribution of the black paint layer (\approx substrate-droplet or substrate-air interfacial temperature) due to the IR transparency of the substrate. Droplets of de-ionized (DI) water were generated at the tip of a needle (gauge 30 and 34), connected to a syringe pump (New Era NE-1000). Droplets with diameters of 1.6 ± 0.05 mm and 1.8 ± 0.05 mm detached due to gravity from needles mounted at heights between 8 mm and 30 mm, leading to impact velocities ranging from 0.2 m/s to 0.6 m/s ($We \approx 1 \sim 10$), as determined from the analysis of side-view high-speed sequences of droplets just prior to impact. Applying voltage to the thin Cr layer, the substrates were heated to

$50^{\circ}\text{C}\pm 0.5^{\circ}\text{C}$ or $65^{\circ}\text{C}\pm 0.5^{\circ}\text{C}$ by Joule heating prior to impact. These substrate temperatures ensure an acceptable signal-to-noise ratio during thermal imaging while preventing substrate degradation. These temperatures are lower than the boiling point of water to avoid contact boiling at the contact line region and to provide stable spreading and receding contact lines. Each experiment was repeated at least three times to ensure good reproducibility of the results. The substrate was allowed to reach its steady-state temperature between the successive impact events.

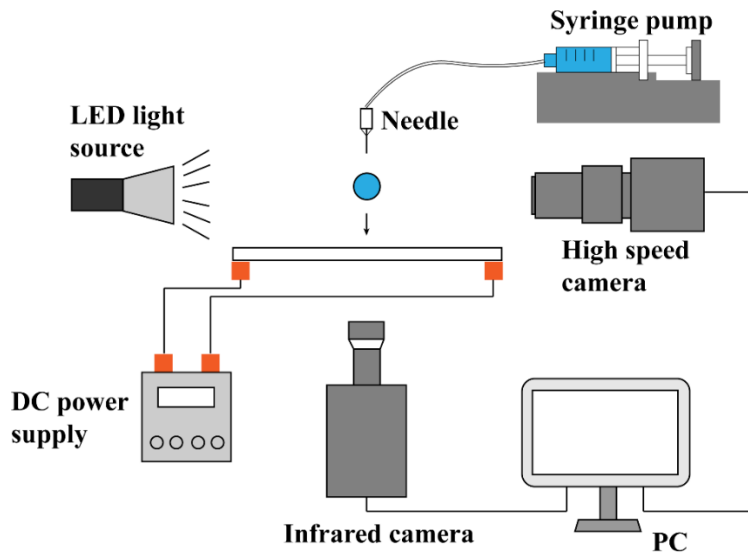


Figure 3-2 Schematic of the experimental setup

3.2.3 Heat transfer analysis and data processing

In order to obtain the local heat flux distribution from the heater to the fluid, an unsteady energy balance was applied at each pixel element, coupled with a transient heat transfer simulation within the calcium fluoride to consider the bottom heat transfer. The pixel element was defined as the portion of the heater that is mapped to one pixel in the image of the IR camera ($30\times 30\ \mu\text{m}^2$) with a thickness comprising the Teflon AF, chromium, and black paint. Then the conservation equation was applied to each pixel element, and the simulation was coupled to solve the bottom heat transfer between the pixel element and the substrate, shown as Figure 3-3.

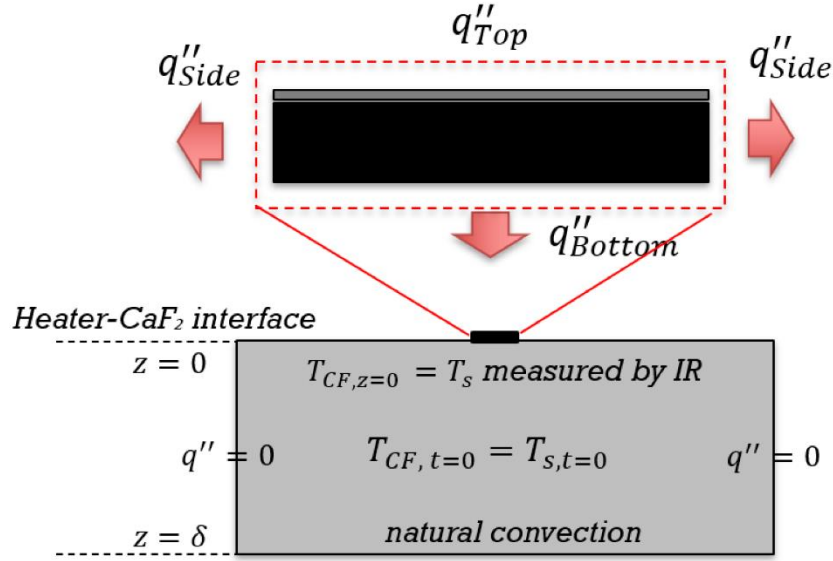


Figure 3-3 Schematic of the heat transfer analysis

The energy conservation equations applied to each pixel element can be expressed as ¹²⁴:

$$Q_{Top} = Q_J - Q_{Store} - Q_{Side} - Q_{Bottom}. \quad (3.1)$$

The calculation of the heat flux is based upon two assumptions:

1. The heat generation from Joule heating is homogenous within the entire chromium layer.
2. The temperature of the heater (including the chromium, the black paint, and the Teflon AF) is uniform across the heater thickness and within each pixel element.

These assumptions and simplifications result in the following expression for the heat flux at the top of the pixel element (*i.e.*, heat flux to air or the droplet):

$$q''_{Top} = \frac{q_J}{A_s} - \frac{Q_{Store}}{B_{Pix}^2 \cdot \Delta t} - q''_{Side} - q''_{Bottom}. \quad (3.2)$$

The chromium and black paint serve as a resistive heater. The heat generated in the Cr thin film by Joule heating can be estimated as:

$$q_J = I_S^2 R_{eCr}. \quad (3.3)$$

To obtain the electrical resistance of the Cr layer for each individual sample, an energy balance was applied prior to droplet impact (*i.e.*, at steady state). The energy balance contains natural convection and thermal radiation exchange at the upper surface of the sample and all other terms discussed in Eq. (3.2). Along with the measured electrical current, we determined a total heater resistance of 8-10 Ω for all samples.

The heat stored in the pixel element was calculated using the temperature change of the element with time:

$$Q_{Store} = B_{Pix}^2 (\delta_{Teflon} \rho_{Teflon} C_{Teflon} + \delta_{Cr} \rho_{Cr} c_{p,Cr} + \delta_{BP} \rho_{BP} c_{p,BP}) (T_{x,y,\tau+1} - T_{x,y,\tau}). \quad (3.4)$$

In order to minimize the signal noise, a weighted averaging of the pixel temperature in time was performed:

$$T_{x,y,\tau} = 0.25T_{x,y,\tau-1} + 0.5T_{x,y,\tau} + 0.25T_{x,y,\tau+1}. \quad (3.5)$$

Heat is conducted to the neighboring pixel elements at the four sides of each element. The application of the 2D heat diffusion equation leads to

$$q''_{Side} = -(k_{Teflon} \delta_{Teflon} + k_{Cr} \delta_{Cr} + k_{BP} \delta_{BP}) \left(\frac{\partial^2 T_S}{\partial x^2} + \frac{\partial^2 T_S}{\partial y^2} \right), \quad (3.6)$$

with

$$\frac{\partial^2 T_S}{\partial x^2} \approx \frac{T_{x+1,y,\tau} - T_{x,y,\tau}}{\Delta x^2} + \frac{T_{x-1,y,\tau} - T_{x,y,\tau}}{\Delta x^2}, \quad (3.7)$$

$$\frac{\partial^2 T_S}{\partial y^2} \approx \frac{T_{x,y+1,\tau} - T_{x,y,\tau}}{\Delta y^2} + \frac{T_{x,y-1,\tau} - T_{x,y,\tau}}{\Delta y^2}. \quad (3.8)$$

As only five different pixel elements (the one of interest and 4 neighboring) are used for the calculation of the surface heat flux, it is very prone to noise, as the heat conduction term is extremely sensitive to the spatial signal noise of the input temperature field. Similar to ref. ¹³⁷, we thus applied a Gaussian filter to the temperature signal, which can suppress the sensitivity. The size of the filter was $n = 5$ and the standard deviation was $\sigma_n = 2.5$.

To obtain q''_{Bottom} , the instantaneous temperature profile of the calcium fluoride window was predicted using a transient finite volume-based three-dimensional simulation using the recorded interfacial temperature distribution, shown in the bottom part of Figure A3. The simulation solves the 3D transient heat equation:

$$\frac{dT_{CF}}{dt} = \frac{k_{CF}}{\rho C_p} \left(\frac{\partial^2 T_{CF}}{\partial x^2} + \frac{\partial^2 T_{CF}}{\partial y^2} + \frac{\partial^2 T_{CF}}{\partial z^2} \right). \quad (3.9)$$

We assign the measured substrate temperature to be the temperature boundary condition at the top surface of the calcium fluoride window $T_{CF,z=0} = T_{s,\tau}$. This temperature value updates every 0.002s, as the temperature measurement result is updated by a new frame. The bottom boundary condition is considered the natural convection condition $q''_{z=\delta} = h_{air}(T_{CF,z=\delta} - T_{air})$. An isothermal boundary condition is imposed on the four external walls.

The natural convection heat transfer coefficient at the bottom surface of the calcium fluoride is predicted using McAdams's correlation for natural convection from a downward-facing horizontal plate:

$$h_{air} = \frac{Nu \cdot k_{air}}{L}, \quad (3.10)$$

$$Nu = 0.27 \cdot Ra_L^{1/4}, \quad (3.11)$$

$$Ra = \frac{g\beta(T_s - T_{air})L^3}{\gamma_{air}\alpha_{air}}, \quad (3.12)$$

$$L \equiv \frac{A_s}{P}. \quad (3.13)$$

Then the heat flux at the interface between the calcium fluoride and the heater assembly can be calculated as:

$$q''_{Bottom} = k \left. \frac{\partial T_{CF}}{\partial Z} \right|_{z=0} \quad (3.14)$$

To validate the in-house code of the finite volume-based three-dimensional (3D) simulation coded in Matlab, we compare our simulation result with that solved by Ansys Fluent, assigning the same function-based temperature boundary condition. This boundary condition mimics the temperature distribution of the substrate of a spreading droplet as recorded by the IR camera, which contains a low-temperature circle-shaped region expanding with time. In addition, we also compare the above results with a 1D simulation (through-plane conduction only) and the pseudo-1D heat flux estimation used in some previous studies^{124, 138}, which regards the substrate as an insulation layer without considering its sensible heat. The heat flux from the substrate to the droplet/air region is calculated by the four methods at the symmetry axis of the imitated liquid-solid interface is shown in Figure 3-3.

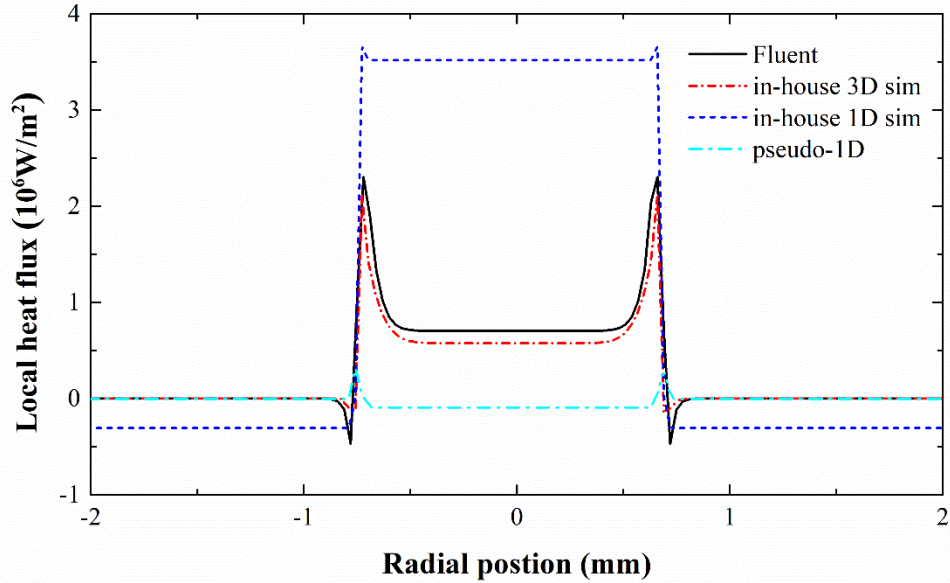


Figure 3-4 Comparison of the calculated heat flux using Ansys Fluent, the in-house 3D simulation, the in-house 1D simulation, and the pseudo-1D method

The in-house simulation has a very good agreement with Ansys Fluent with a maximum deviation less than 16% for all temperature and heat flux values. However, the 1D simulation overpredicts the heat flux by a large amount (up to a factor of 2), which indicates that the horizontal temperature distribution in the substrate is non-uniform, and thus cannot be neglected in the heat flux calculation. The pseudo-1D method underpredicts the heat flux by approximately 85% due to the absence of sensible heat transferred to the droplet from the calcium fluoride substrate. Our analysis method improves the accuracy compared to the pseudo 1D method used in previous studies by a factor of 5^{124, 138}. In conclusion, the in-house simulation method shows comparable performance to the commercial software Ansys Fluent and it improves the accuracy compared to previous methods.

The equivalent droplet diameter was measured in a software called Tracker based on the high-speed snapshots prior to impact. We first identified the diameters in horizontal and vertical directions (D_x and D_y). Then, the equivalent diameter was calculated to be $D_{eq} =$

$\sqrt{0.5(D_x^2 + D_y^2)}$. Finally, the calculated D_{eq} was used as the droplet diameter D in the Weber number calculation and the analytical model in section 3.3.1.

3.2.4 Uncertainty analysis

The contact angle measurements were conducted using sessile-drop technique¹³⁹, followed by the analysis of the droplet figure in a software called ImageJ. We estimate an uncertainty of $\pm 2^\circ$ for all the contact angles measurements.

The impact velocity and initial droplet size measurements were derived from analyzing the pixel variance of the droplets in high-speed videos using a software called Tracker. We estimate an error of ± 2 pixel/s for the impact velocity and ± 2 pixels for the droplet size, which results in an uncertainty of the droplet diameter of less than 1%. The uncertainties of impact velocity and Weber number are estimated to be 1.9% to 3.2% and 3.6% to 10.3%, respectively.

The nominal resolution of the temperature readouts of the IR camera sensor is 25 mK. The IR-measured temperature was calibrated for all the samples using a thin film RTD sensor (Omega, Pt100) with an accuracy of $\pm 0.1^\circ\text{C}$. The readouts were related to the temperature values measured by the RTD using quadratic curve fittings. Combining these errors together, the uncertainty of the IR temperature measurement is $\pm 0.3^\circ\text{C}$.

In the custom-written MATLAB code for calculating temporal heat flux distributions, we applied a Gaussian filter to smoothen the temperature signal and suppress its sensitivity on the heat flux distribution. The use of this Gaussian filter can influence the heat flux results by up to 11%.

However, the effect should be exactly the same for all the cases since the same heat flux analysis method is applied. In addition, the electrical resistance of the heated is determined by an energy balance prior to the droplet impact, resulting in an uncertainty in the reported heat flux values of

0.2%. As a result, all the heat flux values in Figure 3-6, Figure 3-7, and Figure 3-12 to Figure 3-14 have the same uncertainty of 11.2% and error bars are omitted for the sake of clarity.

3.3 Results and Discussions

3.3.1 Droplet impact on a smooth hydrophobic surface

Figure 3-5 presents the images from the droplet impact process in side-view (a), along with the corresponding temperature profiles of the substrate in the bottom-view (b) and the calculated local heat flux distributions (c). The liquid-solid interface can be identified by the lower surface temperature and higher heat flux ($\sim 10^6$ W/m²). The heat flux in the region surrounding the droplet is significantly smaller, at $\sim 10^4$ W/m². For both the spreading and receding regimes, the liquid-solid interface temperature continuously increases and the heat flux decreases. At $t = 3.9$ ms, the droplet reaches the maximum spreading diameter and the local heat flux near the contact line region is significantly lower compared to the earlier times. The contact line velocity is zero at this moment, leading to negligible convective heat transfer. During receding, we observe a lag in the temperature field (*i.e.*, the temperature extends beyond the contact line), whereas the heat flux distribution remains primarily associated with the solid-liquid contact area and decreases both in magnitude and extent. Eventually, as the droplet lifts off the surface, the heat flux approaches zero while the temperature has not recovered to its original value and shows a radial distribution. Based on our observations, for the Weber number range 1 to 10, the droplets completely rebound for $We > 1.4$. In general, the spreading stage has larger heat flux magnitudes than the receding stage, caused by a lower droplet temperature. It is also noticeable that a higher contact line heat flux occurs before the droplet reaches the maximum diameter. Similar observations were also reported by others^{117, 124}.

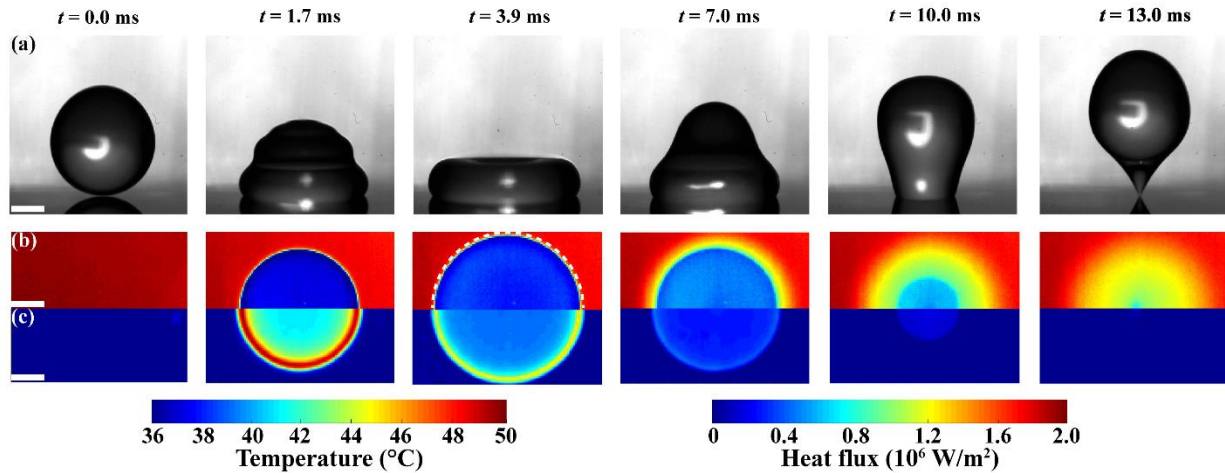


Figure 3-5 Experimental result using synchronized high-speed optical and IR imaging of a droplet impacting a smooth hydrophobic surface at $We = 1.6$ and substrate temperature of 50°C : (a) High-speed camera snapshots of the droplet shape, (b) corresponding temperature, and (c) heat flux distributions. Scale bars are 0.5 mm. The white dashed line in (b) at 3.9 ms marks half of the maximum spreading area that is used to calculate the area-weighted total heat fluxes.

The local heat flux near the three-phase contact line is strongly influenced by the direction of motion of the contact line (receding or advancing contact line) and its velocity¹²²⁻¹²³. In our experiments, the complete rebound of the droplets enables an extensive range of the receding contact line velocities, as shown in Figure 3-6 (a). During spreading, the local heat flux at the contact line has a quadratic relationship with the advancing contact line velocity, as expected¹¹. However, the local heat flux near the contact line during receding is more complex. The receding contact line retracts over a pre-cooled surface, generally leading to a smaller local heat flux. Starting at maximum spreading, where the contact line velocity is close to zero, we notice that the contact line heat flux decreases in a stepwise mode as the contact line velocity decreases during receding. This process can be explained by the radially distributed temperature field ($t = 7.0$ ms to $t = 13.0$ ms in Figure 3-5 (b)). The contact line moves towards the center region where the temperature is lower, suppressing the conduction and evaporation heat transfer. Moreover, the interplay of varying contact line velocity (0 to 0.15~0.2 m/s) and an uneven, time-dependent

temperature distribution leads to a transition mode with this stepwise reduction in the contact line heat flux. At the late receding stage, the contact line heat flux is small and nearly constant.

To quantify the transient heat transfer performance of the entire impact process, we calculated the area-weighted average heat flux within the maximum spreading area of the droplet, shown in Figure 3-6 (b) (for the outline of the maximum spreading area, please refer to panel $t = 3.9$ ms in Figure 3-5 (b)). At the early spreading stage, the heat flux increases rapidly and peaks before the droplet reaches the maximum spreading diameter. This offset in maxima can be attributed to the interplay of transient substrate temperature, effective contact area, and contact line velocity.

Compared to the maximum spreading stage, the droplet has an initially lower temperature during early spreading. Although the liquid-solid interface has not expanded to the maximum, the higher temperature difference between the substrate and the droplet enables the highest overall heat flux to occur during these earlier times (in our case at $t = 2.0$ ms), rather than at maximum spreading. Similar observations have been reported previously^{11, 124}. During the receding process, the heat flux decreases monotonically and finally approaches zero as the liquid-solid interface diminishes due to the complete rebound.

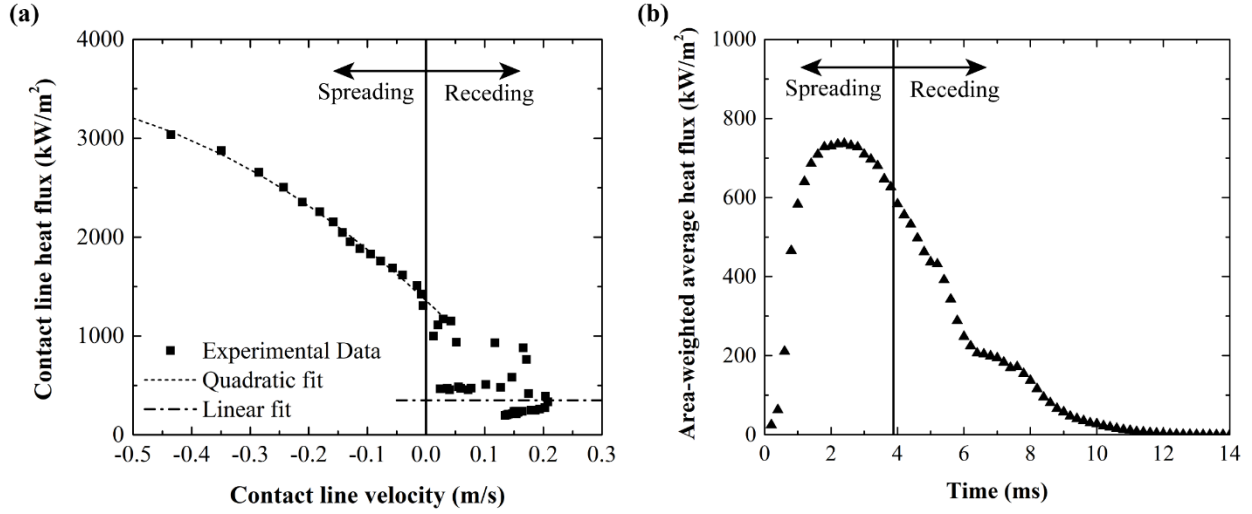


Figure 3-6 The heat flux evolution of droplet impact at $We = 1.6$ and substrate temperature at $50 \pm 0.5^\circ\text{C}$. (a) The contact line heat flux (maximum heat flux within ± 3 pixel from the contact line) plotted against the corresponding contact line velocity. (b) Transient behavior of the heat flux normalized by the maximum spreading area. The uncertainty in heat flux values is universally 11.2%. Error bars are omitted for the sake of clarity.

After understanding the time-dependent heat transfer performance during the droplet impact process, we now explore the variables that control the total transferred heat using analytical and experimental methods. According to Herbert *et al.*¹¹, the conduction heat transfer accounts for over 70% of the total heat transfer. Thus, we neglect evaporation and establish an analytical model based on the single-phase heat transfer assumption. Due to the short contact time, the advection inside the droplet is also neglected. We consider the droplet and substrate as two semi-infinite solid bodies at different initial temperatures, which allows us to predict the heat transfer based on one-dimensional energy equations. The energy equations in the substrate s and the liquid droplet l are expressed as

$$\frac{\partial T_s}{\partial t} - \alpha_{ts} \frac{\partial^2 T_s}{\partial z^2} = 0, \quad (3.15)$$

$$\frac{\partial T_l}{\partial t} - \alpha_{tl} \frac{\partial^2 T_l}{\partial z^2} = 0, \quad (3.16)$$

where α_{ts} and α_{tl} are the thermal diffusivity of the calcium fluoride substrate (ignoring the heater coating) and the droplet.

The initial and boundary conditions for the two equations are, $T_s(t = 0) = T_{s0}$, $T_l(t = 0) = T_{l0}$, and $T_s(z = -\infty) = T_{s0}$, $T_l(z = \infty) = T_{l0}$.

The temperature at the solid-liquid interface is assumed to be equal,

$$T_s(z = 0) = T_l(z = 0) = T_{interface}. \quad (3.17)$$

Then, a time-independent interface temperature can be solved analytically ¹⁴⁰,

$$T_{interface} = \frac{\sqrt{(k\rho c_p)_l}T_{l0} + \sqrt{(k\rho c_p)_s}T_{s0}}{\sqrt{(k\rho c_p)_l} + \sqrt{(k\rho c_p)_s}}, \quad (3.18)$$

where k , ρ , and c_p represent the thermal conductivity, density, and heat capacity. The predicted interface temperature depends only on the initial temperature and the physical properties of the two bodies. Then, the heat flux at the interface can be solved on either side using

$$q''(t) = k \frac{\partial T_s}{\partial z} \Big|_{z=0} = k(T_{s0} - T_{interface})/\sqrt{\pi\alpha t}. \quad (3.19)$$

The total transferred heat can be obtained by integrating the heat flux over the residence time t_r as

$$Q = \int_0^{t_r} q''(t)\pi r(t)^2 dt. \quad (3.20)$$

The spreading diameter in our experiment agrees well with the expression ⁴¹

$$r(t) = \frac{27}{8} D\beta_{max} \frac{t}{t_r} \left(1 - \frac{t}{t_r}\right)^2, \quad (3.21)$$

where β_{max} is the maximum spreading ratio and D is the diameter of the impacting droplet. The total transferred heat is then calculated as

$$Q = C_1 \beta_{max}^2 t_r^{0.5}, \quad (3.22)$$

$$C_1 = 0.194 \left(\frac{\pi}{\alpha_s} \right)^{-0.5} k_s (T_s - T_{interface}). \quad (3.23)$$

After applying the scaling law of maximum spreading ratio $\beta_{max} \propto We^{0.25}$ proposed by Clanet *et al.*¹⁴¹ and the residence time $t_r \propto \sqrt{\rho D^3 / \sigma}$ proposed by Richard *et al.*¹⁴², the total transferred heat scales as

$$Q \propto \frac{D^{1.25} v}{\sigma^{0.75}}. \quad (3.24)$$

where v is the impact velocity, and σ is the surface tension of the liquid droplet. In this study, only water is used for the droplet to assist in droplet lift-off, so σ equals to the surface tension of water. Hence one can expect

$$Q \propto D^{1.25} v. \quad (3.25)$$

The experimental results of total transferred heat versus $D^{1.25} v$ are given in Figure 3-7 and show good agreement with the predicted scaling law with R^2 values of 0.968 and 0.974 for substrate temperatures of 50°C and 65°C, respectively. The total transferred heat is measured by integrating the temporal total heat flux over the residence time. A small dip of the total transferred heat can be noticed at $D^{1.25} v \approx 0.11-0.13$ for both surface temperatures, which is attributed to the occurrence of the entrapped bubbles.

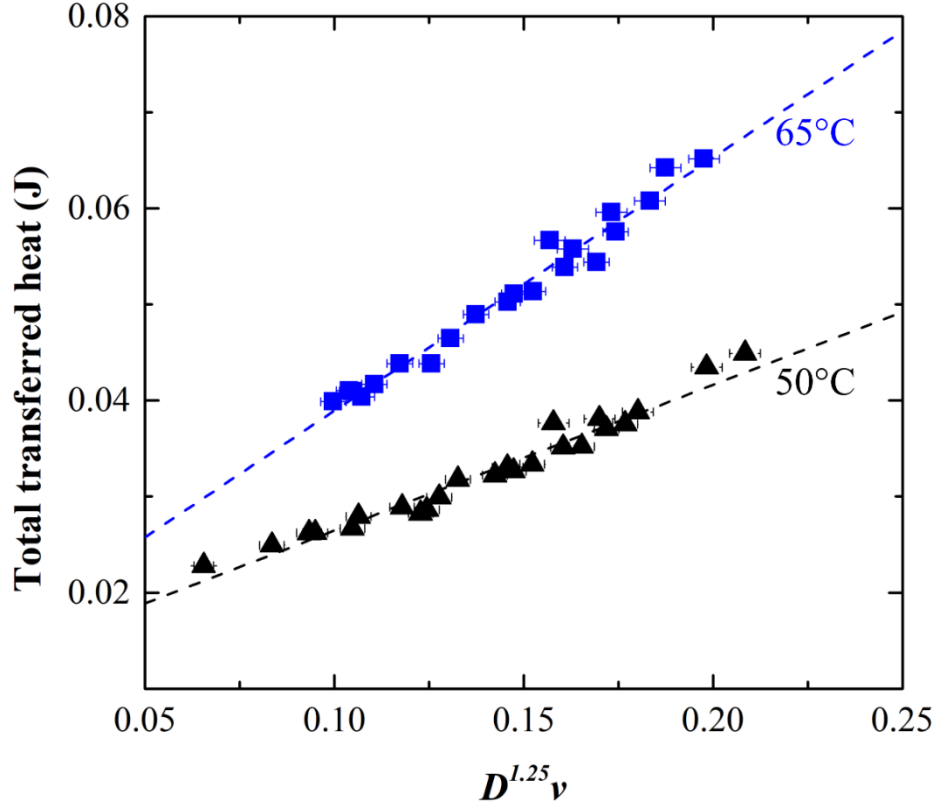


Figure 3-7 The total transferred heat at substrate temperatures of $50 \pm 0.5^\circ\text{C}$ (black triangle) and $65 \pm 0.5^\circ\text{C}$ (blue square) and the corresponding $D^{1.25}v$ value. The dashed lines are the linear curve fittings of the two data sets, with R^2 value 0.968 (black) and 0.974 (blue). Droplets at two sizes, $D=1.6 \pm 0.05$ mm and $D=1.8 \pm 0.05$ mm at impact velocities from around 0.2 m/s to 0.6 m/s were tested.

In addition, we also calculated the total transferred heat based on Eq. 3.22 using the expression of maximum spreading ratio and residence time proposed by other studies¹⁴³⁻¹⁴⁴. In Eq. 3.25, for the maximum spreading we used the relatively simple scaling given Clanet *et al.*¹⁴¹ to estimate the heat transfer of our impacting droplets. To evaluate the validity and accuracy of this choice, we compare our modeling and experimental results to more sophisticated spreading models. In Liang *et al.*¹⁴³, the empirical expression for the maximum spreading diameter and residence time of the droplet are given as $\beta_{max} = 0.788 We^{0.306}$ and $t_r = 1.032 We^{0.494}$, respectively.

Substituting these expressions into Eq. 3.22, *i.e.*, total transferred heat $Q = C_1 \beta_{max}^2 t_r^{0.5}$, we would obtain

$$Q \propto We^{0.859}. \quad (3.26)$$

Using this scaling, the experimental data is plotted against $We^{0.859}$ at substrate temperatures of 50°C and 65°C is shown in Figure 3-8 (a). In contrast to the excellent agreement that we obtained in Figure 3-7, we see that the data points do not converge to a single line, indicating that above expression (Eq. 3.26) is not suitable for predicting the dependence of the total transferred heat on the impact parameters. This result shows that the droplet size has a stronger influence on the heat transfer than suggested by using the scaling laws from Liang *et al.*

We also tested a more complicated scaling as given by Laan *et al.* ¹⁴⁴:

$$\beta_{max} = Re^{0.2} P^{0.5} (A + P^{0.5}), \quad (3.27)$$

where $P = WeRe^{-0.8}$ and $A = 1.24 \pm 0.01$. Using the expression of t_r by Richard *et al.* ¹⁴², the total transferred heat should scale with $\beta_{max}^2 D^{1.5}$. The result using this scaling is provided in Figure 3-8 (b). Compared to the empirical expression in Liang *et al.*, this expression shows some improvement (R^2 values of 0.901 and 0.915 for substrate temperatures of 50°C and 65°C, respectively) in predicting the tendency of the total transferred heat. However, the expression by Clanet *et al.* ¹⁴¹ and Richard *et al.* ¹⁴² are not only surprisingly simple, but also provide the best agreement with the experimental data.

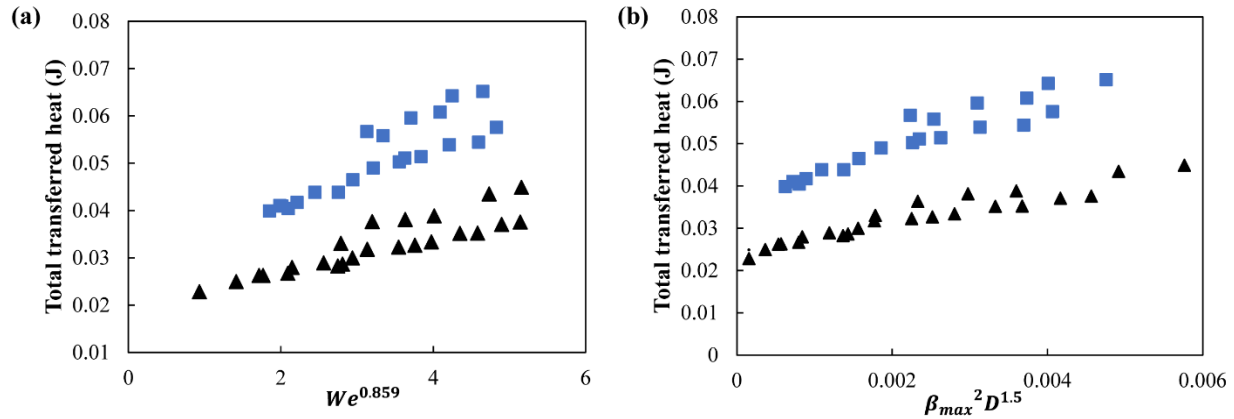


Figure 3-8 Comparison of scaling models for the total transferred heat at substrate temperatures of $50 \pm 0.5^\circ\text{C}$ (black triangle) and $65 \pm 0.5^\circ\text{C}$ (blue square) for (a) $We^{0.859}$ as derived from Liang *et al.*¹⁴³ and (b) $\beta_{max}^2 D^{1.5}$ from Laan *et al.*¹⁴⁴

3.3.2 Bubble entrapment and inner contact line heat transfer

The bubble entrapment of an isothermal droplet impact is shown in Figure 3-9 (a). As the droplet impacts the solid surface, a capillary wave forms and propagates along the droplet during spreading¹⁴⁵. At $t = 4.3$ ms, the oscillation creates a cylindrical air cavity located at the center of the drop, *i.e.*, the droplet has a toroidal shape at maximum spreading. For a specific range of impact velocities, the bottom of the air cavity connects with the impact microbubble and forms a dry zone at the center of the droplet, while the upper region of the cavity continues retracting. At $t = 5.1$ ms, the air cavity can be identified to be a conical shape, which indicates the formation of the dry zone and the inner contact line. At $t = 5.5$ ms, as the top part of the air cavity closes, an entrapped bubble is formed and attaches to the surface at the center region of the droplet. In the meantime, a jet is emitted due to the reconnection of the liquid film and the sudden pressure change in the bubble. This entrapped bubble, which approximately remains the same size as the droplet retracts, ruptures after $t = 12.9$ ms as the primary outer contact line and secondary inner contact line of the bubble meet.

On a heated surface, the droplet dynamics are slightly changed, as shown in Figure 3-9 (b) and (c). At a substrate temperature of 50°C, the air cavity is smaller than for the isothermal case. As a result, at $t = 5.5$ ms, the entrapped bubble is smaller in size while a tiny jet is still visible above the droplet. As shown in Figure 3-9 (c), when the substrate temperature increases to 65°C, the air cavity originally appears to be a thin cylinder instead of a cone, leading to a much smaller size of the entrapped bubble in the later time step. We can conclude that the bubble size decreases for a given impact Weber number as the substrate temperature increases.

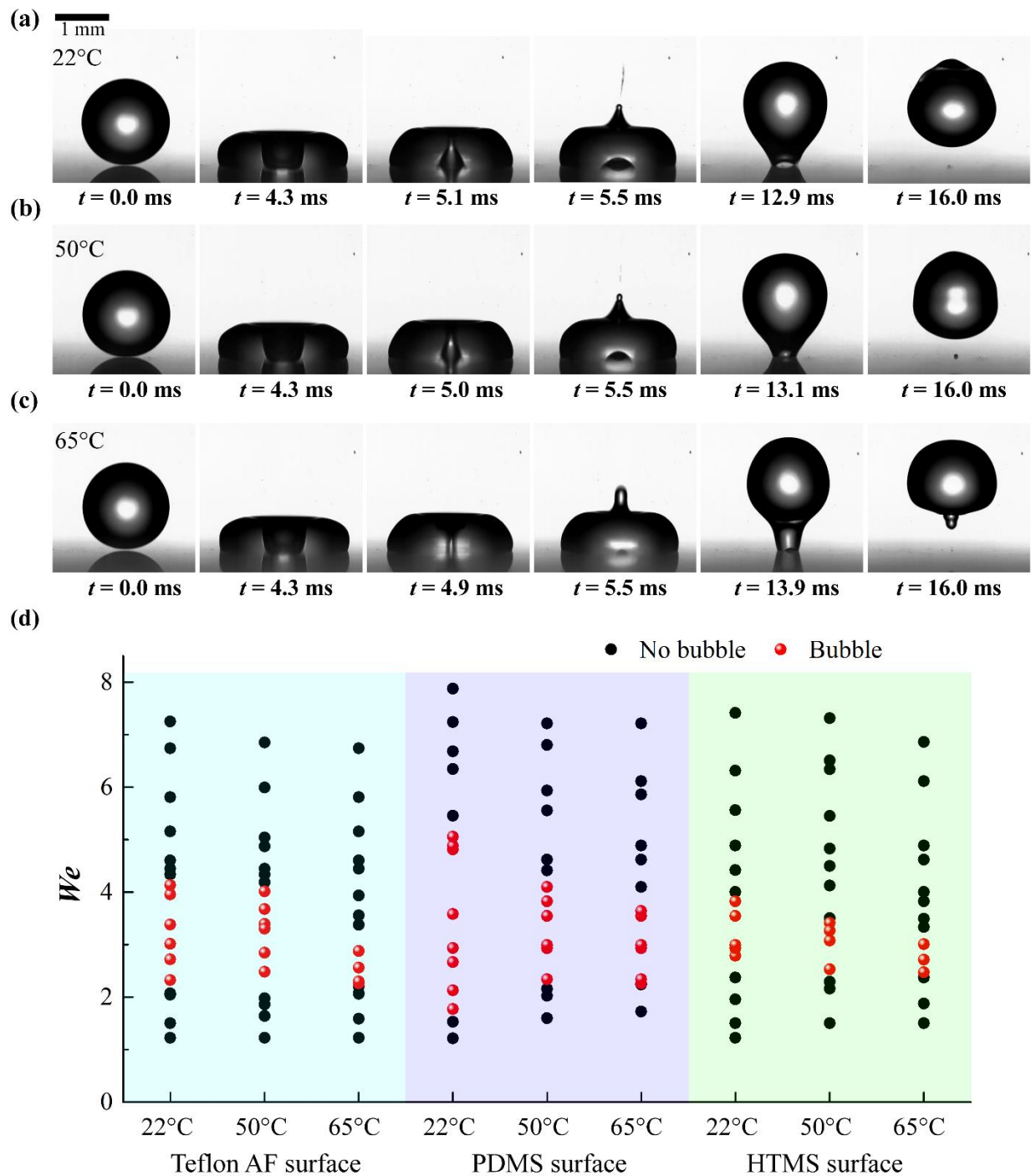


Figure 3-9 Bubble entrapment during droplet impact on a smooth Teflon AF surface with $We = 3.0$ at substrate temperatures of (a) 22°C, (b) $50 \pm 0.5^\circ\text{C}$, and (c) $65 \pm 0.5^\circ\text{C}$. (d) Bubble entrapment behavior at different Weber numbers, substrate temperatures, and surface chemistries. The contact angles of the PDMS surface are $\theta_{eq} = 104^\circ$, $\theta_{ad} = 110^\circ$, and $\theta_{re} = 87^\circ$. The contact angles of the HTMS surface are $\theta_{eq} = 100^\circ$, $\theta_{ad} = 103^\circ$, and $\theta_{re} = 84^\circ$. As a reminder, contact angles on Teflon AF are $\theta_{eq} = 115^\circ$, $\theta_{ad} = 126^\circ$, and $\theta_{re} = 111^\circ$.

To investigate the influence of temperature on bubble occurrence on hydrophobic surfaces, we compared droplet impact dynamics on the Teflon AF coating to polydimethylsiloxane (PDMS) and hexadecyltrimethoxysilane (HTMS) coatings. The PDMS surface was prepared by spin-coating a 3- μm -thick diluted PDMS mixture (Sylgard 184 monomer, cross-linker, and Toluene at a ratio of 10:1:50) on the Teflon AF substrates and curing it at 110 °C for 1 h. The HTMS surface was prepared by vapor depositing a mixture of HTMS and Toluene at a ratio of 1:9 on the Teflon AF substrates and curing it at 90 °C for 4 h. Figure 3-9 (d) summarizes the impact conditions for the occurrence of bubble entrapment. For all the three hydrophobic surfaces we investigated, the bubble entrapment occurs for $2.5 < We < 4.1$ at room temperature. It is noticeable that the PDMS surface has the largest range ($1.8 < We < 5.0$) for the bubble occurrence at room temperature among the three surfaces, while this range is different from the observations in Chen *et al.*¹²⁸. The Weber number range for the bubble entrapment decreases at higher substrate temperatures for all three coatings.

The general dynamics of bubble entrapment on the three hydrophobic surfaces (Teflon AF, PDMS, and HTMS) are provided in Figure 3-10. The impact Weber numbers are selected based on the stable occurrence of the entrapped bubble. The bubble can be around 0.6 mm in diameter on the Teflon AF surface, while on the PDMS and HTMS surface, it only reaches around 0.2 to 0.3 mm in diameter. Thus, the majority of non-isothermal bubble entrapment experiments are conducted on the Teflon AF surface, serving the purpose of investigating the local heat transfer behavior of the inner contact line and the total heat transfer effect from the bubble.

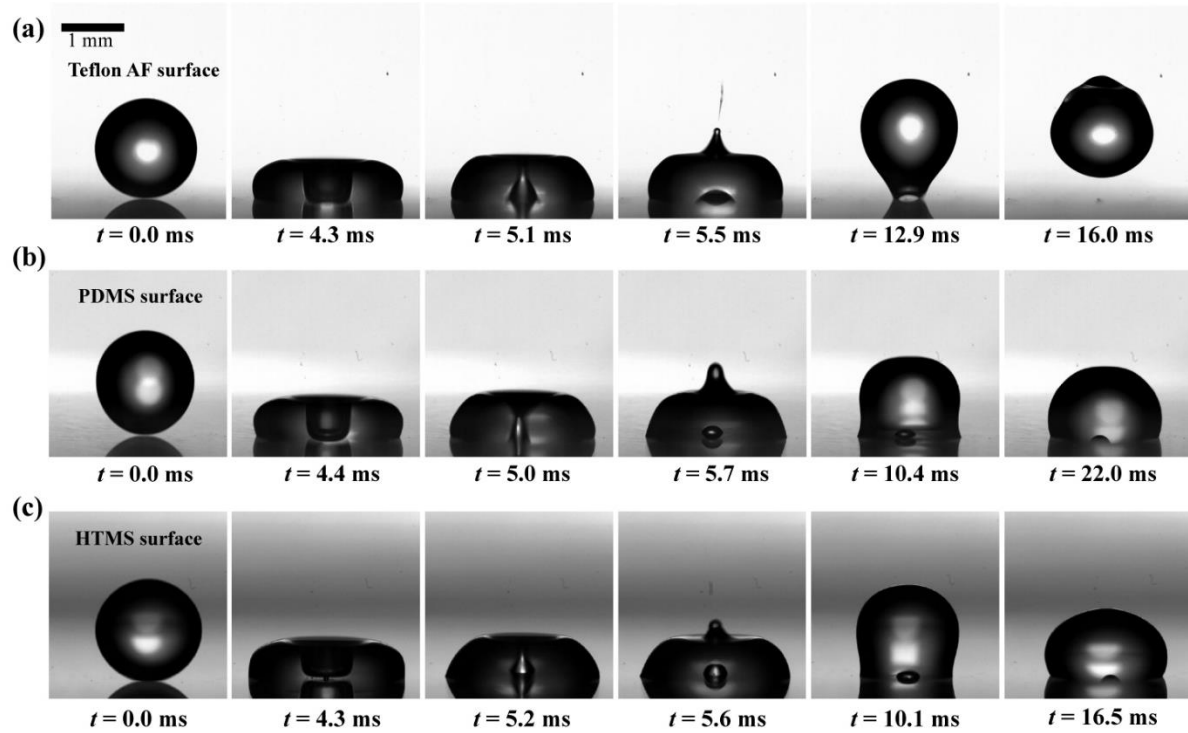


Figure 3-10 Bubble entrapment during droplet impact on different hydrophobic surfaces at room temperature (22°C). (a) Teflon AF surface at $We = 3.0$, (b) PDMS surface at $We = 2.5$, (c) HTMS surface at $We = 3.4$.

Compared to the PDMS and HTMS surfaces, Teflon AF has the largest entrapped bubble size, enabling more accurate measurements of the heat transfer behavior of the inner contact line and bubble region using IR imaging. Figure 3-11 highlights the influence of the bubble entrapment on the interfacial temperature and heat flux distribution. As shown in Figure 3-11 (a)-(c), at $t = 4.2$ ms, the aforementioned cone-shaped air cavity is developing inside the droplet. From the bottom view, we can distinguish a small high-temperature spot near the center of the droplet, surrounded by a low-temperature region. This spot is formed due to the presence of the impact microbubble generated within the first 100 μs after impact^{130, 146}. Interestingly, a similar high-temperature spot was not observed in Figure 3-5 or for most droplet impacts with $We < 2.0$. The impact bubble size is dependent on the impact velocity and the initial air disc may develop into multiple microscopic bubbles due to surface irregularities and hence be smaller than the spatial resolution of the camera sensor^{130, 147-148}. As shown in the heat flux panel (Figure 3-11 (c)), the

heat flux at the center is close to zero, surrounded by a high heat flux region. Two phenomena are responsible for this high heat flux region: the contact line of the impact bubble increases the local evaporation rate, and the developing millimetric air cavity causes a strong downward-facing convective flow inside the droplet. At $t = 4.8$ ms, a large cylindrical air cavity with a dry-out region on the surface is visible in the shadowgraph image and reflected in the IR image. Due to the low conductivity of the entrained air, the interface temperature in this central dry-out region is 4-5°C higher than in the surrounding liquid-covered area. At $t = 5.4$ ms, the bubble is trapped as the upper part of the cavity reconnects. Compared to the initial air cavity observed at $t = 4.8$ ms, the inner contact line around the entrapped bubble is smaller, indicating a retraction of the contact line during the evolution of the bubble. The formation of the bubble stabilizes the inner contact line, leading to a higher heat flux at the contact line region. During the later time steps ($t = 6.6$ ms, 8.0 ms, 8.6 ms), the droplet (*i.e.*, outer contact line) keeps retracting while the inner contact line remains stable. The heat flux near the inner contact line region decreases more slowly than the primary contact line, as the interface temperature near the inner contact line is stable while the primary contact line moves towards the low-temperature region, *i.e.*, the center region. Consequently, the region of the highest heat flux transitions from the outer contact line to the inner contact line for $t > 6.6$ ms.

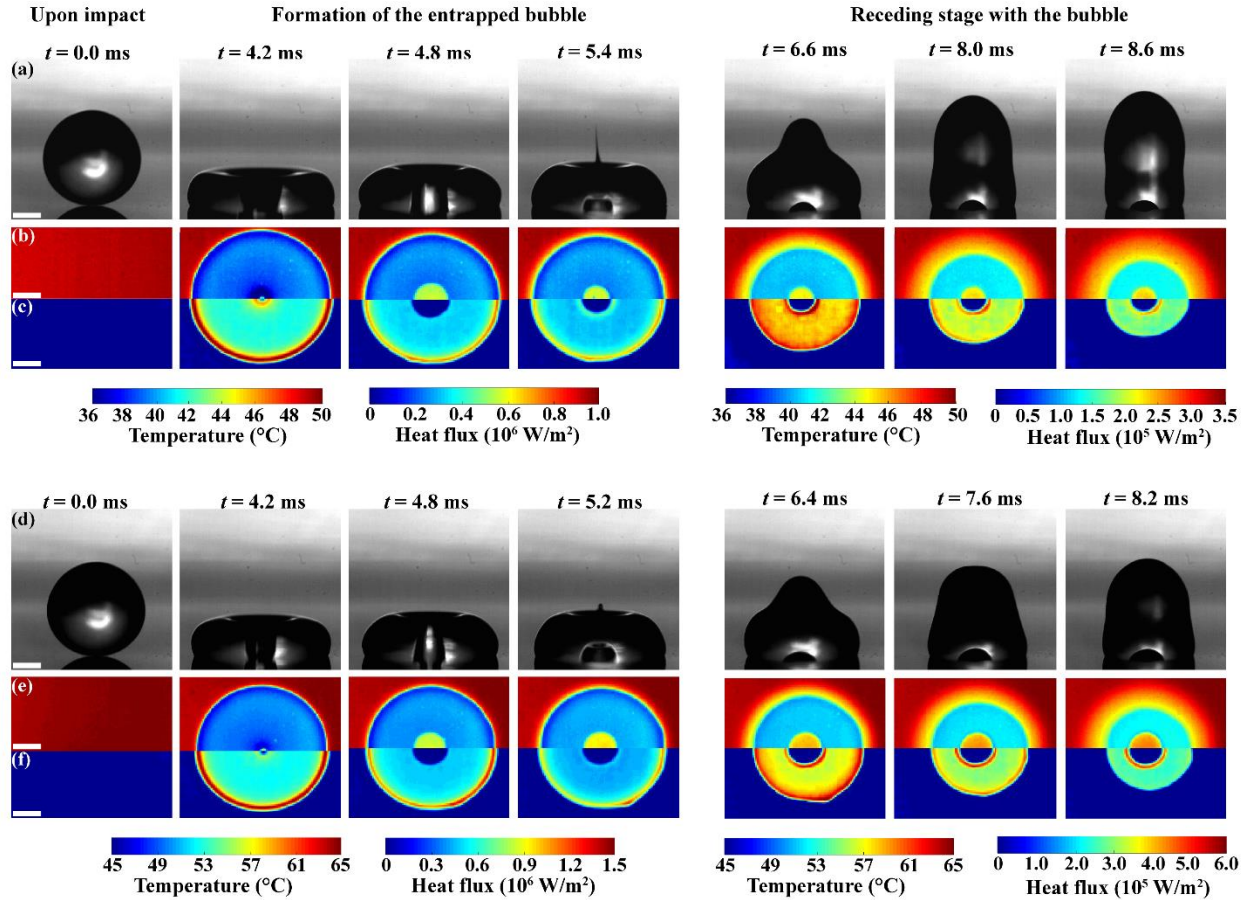


Figure 3-11 Experimental result for bubble entrapment during droplet impact on heated surfaces (a,d) side-view images of the droplet shape, and (b,e) corresponding temperature, and (c,f) heat flux distributions. (a-c): $We = 4.0$, substrate temperature $50 \pm 0.5^\circ\text{C}$; ((d-f): $We = 2.8$, substrate temperature $65 \pm 0.5^\circ\text{C}$. Scale bars are 0.5 mm.

The droplet and bubble dynamics of the second example (d-f) in Figure 3-11 are slightly different from the first one because of the smaller impact Weber number. According to Figure 3-9(d), the bubble entrapment exists only in a very narrow range of $2.1 < We < 3.0$ at a substrate temperature of 65°C . Similar to the example at 50°C , the impact microbubble is visible at $t = 4.2$ ms, before the central dry-out region forms. However, the dimple on the top surface of the droplet is less pronounced than in the previous example (a-c) due to the lower We number of 2.8 (*vs.* 4.0). After the cylindrical air cavity forms, nearly no retraction of the inner contact line is observed; neither from the high-speed optical nor the IR images. Furthermore, the upper part of this cone-shaped cavity is significantly narrower than the bottom part, which indicates a faster

retraction at the top of the droplet. At the same time, the bulk of the droplet, which spreads to a slightly smaller maximum diameter, provides less retraction force from the side to move the inner contact line and the bottom part of the cavity. Hence, the dry-out region retains a larger size during the reconnection, leading to a larger entrapped bubble. Similar to the previous example, the heat flux remains high at the inner contact line but continuously decreases at the outer contact line. At the late receding stage ($t = 8.2$ ms), the heat flux enhancement of the outer contact line vanishes, while the inner contact line remains at a significantly higher value than the bulk of the droplet.

The temporal evolution of the local heat flux near the secondary inner contact line and the primary outer contact line are presented in Figure 3-12. For both substrate temperature conditions, the heat flux near the primary contact line decreases rapidly while the change near the inner contact line region is much slower. These findings agree well with the qualitative observations made regarding Figure 3-11. The local heat flux near the inner contact line surpasses the primary contact line at $t = 6.2$ ms for the substrate temperature of 50°C and at $t = 6.6$ ms for the substrate temperature of 65°C . In Figure 3-12 (a), the inner contact line shows a local maximum in heat flux at around $t = 5.5$ ms. This sudden increase of the local heat flux is caused by the retraction of the inner contact line when the upper part of the cavity reconnects and the bubble forms. The retraction leads to an advancing inner contact line and enhanced convective heat transfer. This phenomenon matches our discussions about the heat flux at a moving contact line in Section 3.3.1. However, for the substrate temperature of 65°C , this jump in heat flux is absent due to a relatively stable inner contact line. The different heat transfer behaviors of the two contact lines indicate that a receding contact line of the droplet causes a faster reduction in the local heat flux than a stable contact line. Although a moving contact line

adds convective heat transfer as compared to a stationary one, the receding contact line suffers from a decreasing temperature gradient (bulk droplet vs. interfacial temperature) as it moves towards the center's low-temperature region. The lower substrate temperature leads to a smaller conduction and evaporation heat transfer, which at these small contact line velocities dominate the local heat transfer behavior.

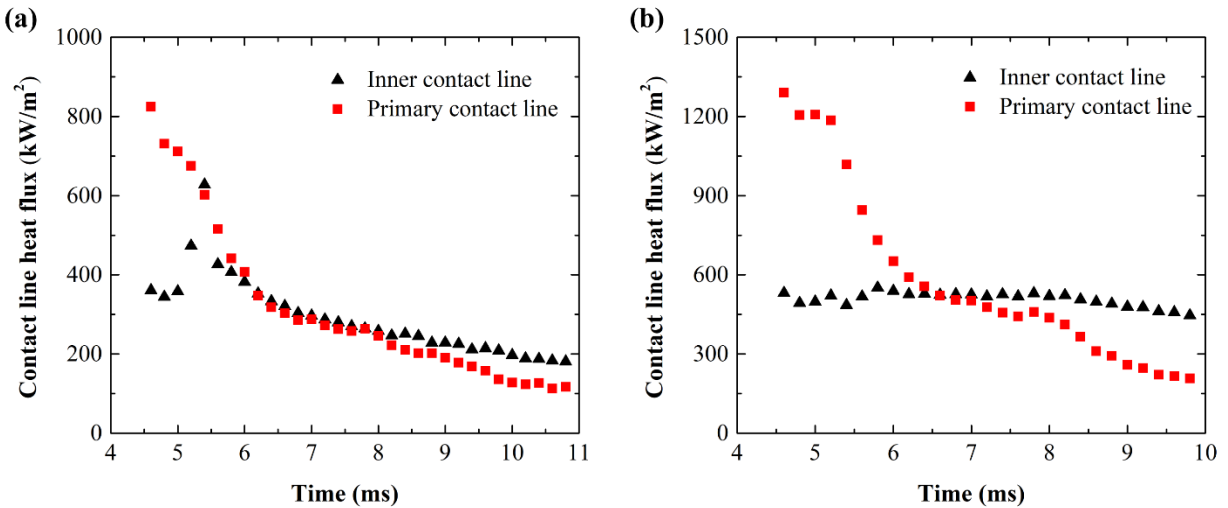


Figure 3-12 The heat flux at the inner contact line (black triangles) and the primary outer contact line (red squares). Plotted are the average heat flux values of the right and left side of the contact lines along the symmetry axis. (a) $We = 4.0$, substrate temperature $50 \pm 0.5^\circ\text{C}$, (b) $We = 2.8$, substrate temperature $65 \pm 0.5^\circ\text{C}$.

The entrapped bubble also influences the overall heat transfer potential of the droplet. Because the bubble occurs only during the receding stage, the heat transfer mechanism of the spreading stage will be the same as discussed in the previous chapter. During the receding stage, however, the entrapped bubble reduces the solid-liquid contact area, which reduces the total conduction heat transfer rate. On the other hand, due to the existence of the inner contact line, the contact line length is increased, and evaporation is enhanced. As a result, the bubble leads to a combined effect of decreased conduction heat transfer and increased evaporative heat transfer. This poses the question: Which effect dominates? Figure 3-13 compares the total transferred heat during droplet impact with the entrapped bubble to a droplet without the bubble. The total transferred

heat Q of the droplet with bubble entrapment is approximately 5.6% and 7.1% lower than the impact without the bubble at surface temperatures of 50°C and 65°C, respectively. For this comparison, all experiments were conducted in a very narrow Weber number range near the upper limit of bubble occurrence, as outlined in Figure 3-9 (d). Once the bubble entrapment was observed near the upper limit, the impact height was increased ever so slightly to obtain droplet impact without bubble entrapment, minimizing the influence that otherwise arises from different Weber number impacts (such as larger spreading diameter, higher contact line velocity, *etc.*), allowing the direct comparison between the two cases. Based on the scaling law of $Q \propto D^{1.25}v$, the effects of the impact Weber number difference on the total transferred heat are predicted to be within 1.9% and 2.0% at the substrate temperature of 50°C and 65°C, respectively, which is smaller than the measured heat transfer deviation. Thus, the existence of the entrapped bubble is the dominating reason for the large difference in total transferred heat.

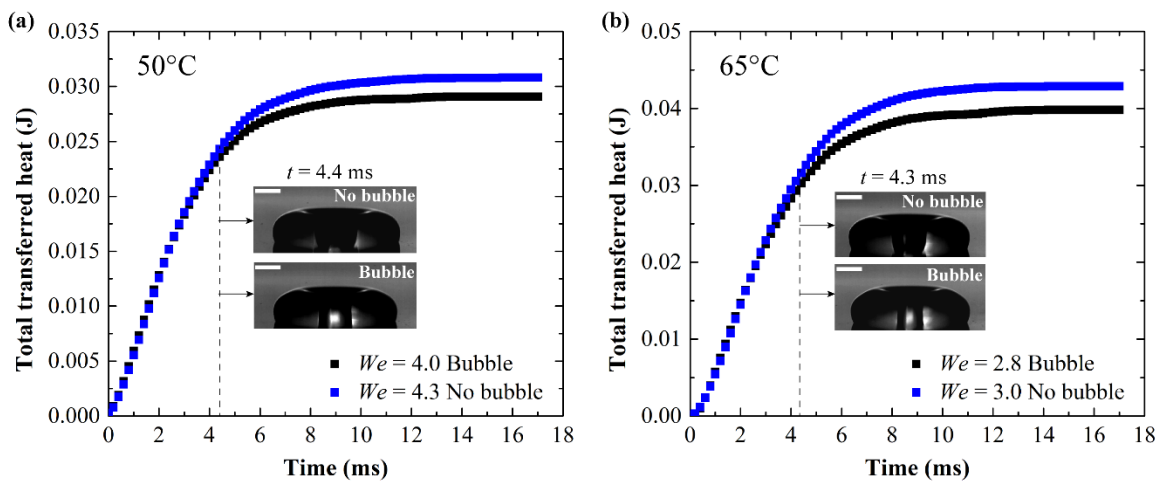


Figure 3-13 The transient evolution of total transferred heat during droplet impact with and without an entrapped bubble at (a) 50±0.5°C substrate and (b) 65±0.5°C substrate. The droplet impact experiments with the bubble entrapment were conducted near the upper limit of the Weber number range of bubble occurrence. Then the impact height was increased ever so slightly to obtain a droplet impact condition without bubble entrapment.

Before the dry-out region forms, the difference in the total transferred heat between the two cases is negligible, which confirms the validity of our comparison. After the dry-out region is formed, the two lines diverge quickly. Hence, the loss of the interface area has a more significant influence on heat transfer than the increase in the contact line length. This finding confirms the statement in Section 3.3.1 that the conduction heat transfer dominates the total heat transfer. It is also noticeable that a small increase occurs for both black (“with bubble”) lines at around $t = 12.0$ ms. This small increase in total transferred heat is attributed to the rupture of the entrapped bubbles, which causes the formation of a small liquid-solid interface on the previous high-temperature bubble region.

To better understand the individual contributions of conduction, convection, and evaporation, we post-processed the data to exclude one of the components. As the evaporative heat transfer dominates the local heat transfer at the contact line ¹⁴⁹, we disregarded the heat flux near the inner contact line after the cavity occurred from our analysis, shown in Figure 3-14. Since the inner contact line is stationary, convective heat transfer can be neglected. When compared to the no bubble case, the reduction in total transferred heat between these two cases can then be attributed to a loss in conduction heat transfer, caused by the reduced liquid-solid contact area, which is estimated to 6.9% and 9.3% of the total heat transfer at substrate temperatures of 50°C and 65°C, respectively. These results indicate that the added evaporative heat transfer by creating the inner contact line contributes approximately 1.3% and 2.2% to the total heat transfer, respectively, at the two substrate temperatures.

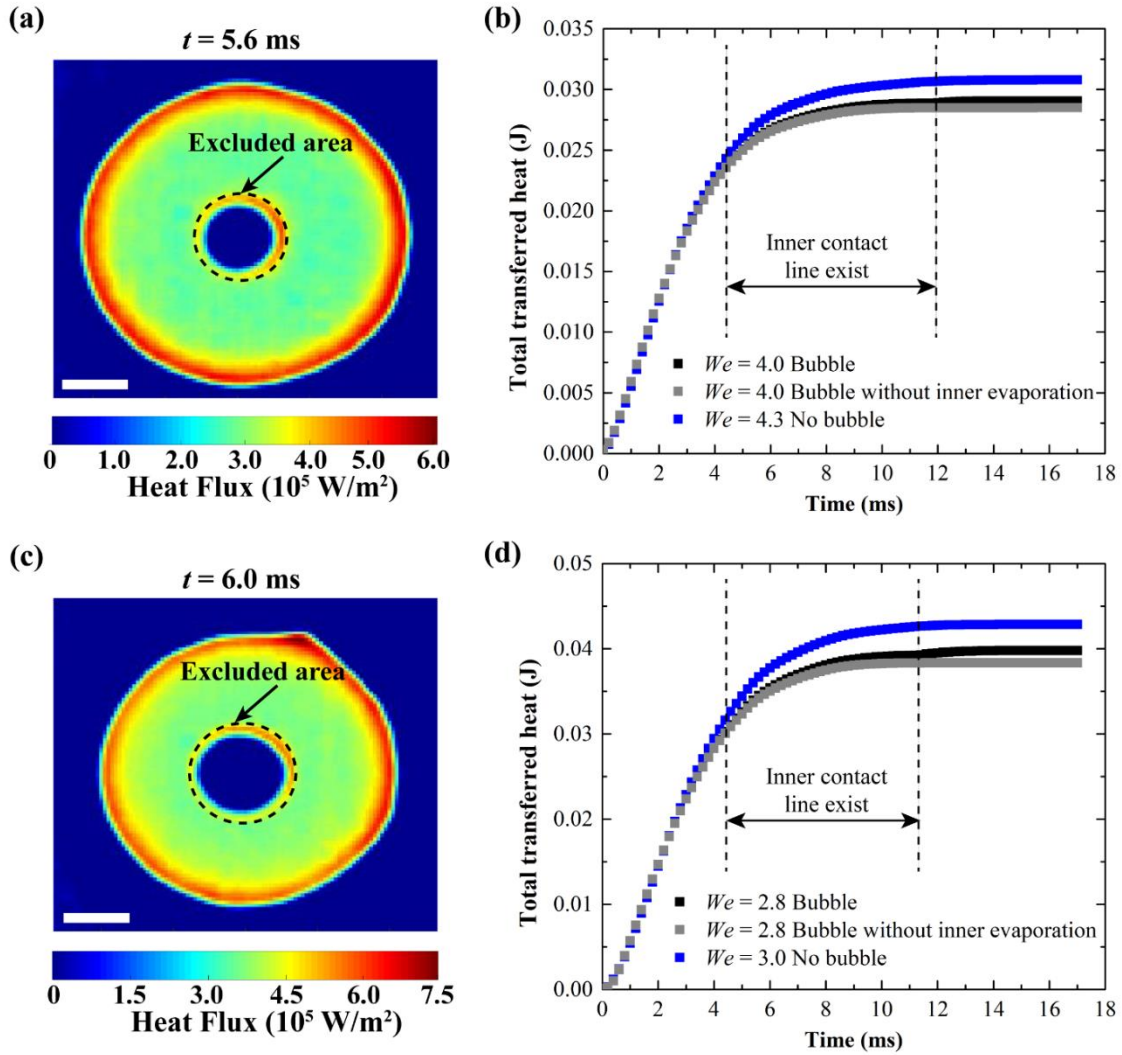


Figure 3-14 The heat flux distribution in bottom view for bubble entrapment at (a) $We = 4.0$ and substrate temperature of $50^{\circ}\text{C} \pm 0.5^{\circ}\text{C}$, (c) $We = 2.8$ and substrate temperature of $65^{\circ}\text{C} \pm 0.5^{\circ}\text{C}$; The total transferred heat during the droplet impact with a trapped bubble, with trapped bubble excluding the inner evaporation, and without the entrapped bubble at a substrate temperature of (b) $50^{\circ}\text{C} \pm 0.5^{\circ}\text{C}$ and (d) $65^{\circ}\text{C} \pm 0.5^{\circ}\text{C}$.

Another interesting topic that follows from our observations is the diffusion and saturation limit inside the entrapped bubble. Distinct from the primary contact line, where the evaporated vapor has an infinite outer space to diffuse or mix into, the inner contact line has only a limited space for vapor diffusion. When the vapor concentration inside the air bubble approaches saturation, the evaporation inside the bubble will be suppressed. Eventually, as evaporation becomes negligible, the inner contact line should have a similar local heat flux as the rest of the droplet.

However, this phenomenon cannot occur for bubble entrapment inside a bouncing droplet due to the short time scales associated with droplet rebound. To circumvent this limitation, we repeated some experiments where the droplet was prevented from completely rebounding by intentionally contaminating the sample surfaces. The contamination was deposited by repeating the droplet impact at the same sample location more than 20 times without cleaning. As a result, the droplet retracted to only approximately 50% of its maximum spreading diameter and then remained pinned. Figure 3-15 shows the heat flux distributions near the bubble region at different times and the temporal evolution of the local heat flux near the inner contact line. In both conditions, the heat flux becomes smaller at a longer residence time, as expected. For substrate temperatures of 50°C and 65°C, the inner contact line heat flux reaches a similar value as the surrounding regions at around $t = 110$ ms and $t = 140$ ms, respectively, indicating saturation of the bubble cavity. These observations indicate that approximately 0.1 seconds are sufficient to suppress evaporation at the inner contact line.

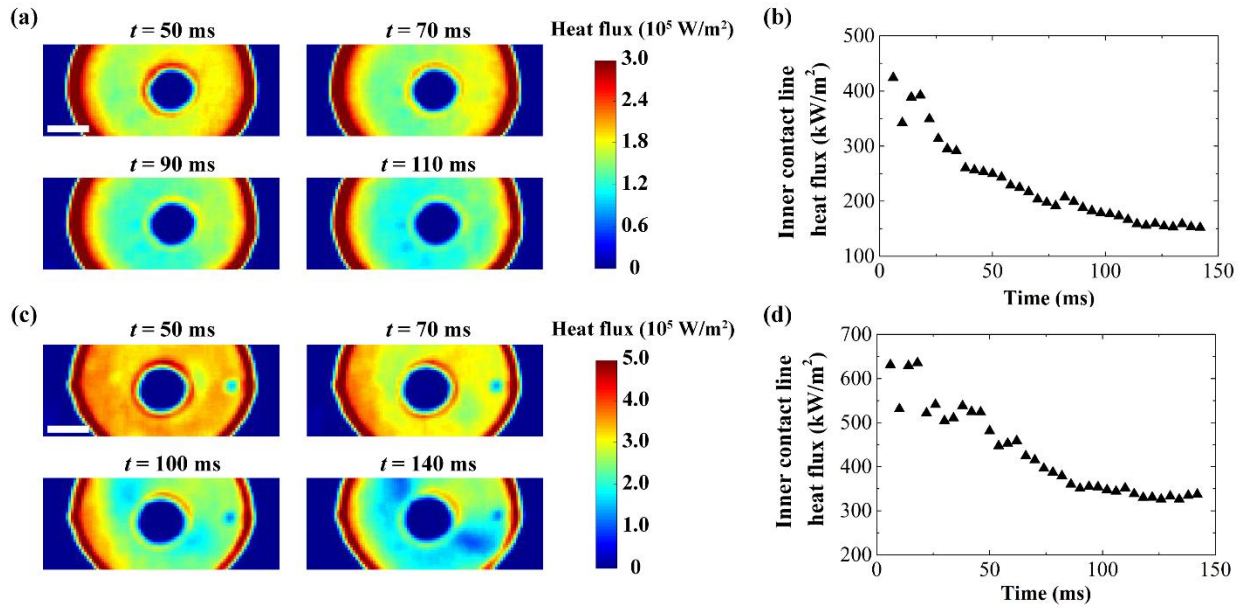


Figure 3-15 Heat flux distributions near the bubble and inner contact line regions. The color bar of the images is based on the heat flux value of the inner contact line region. The scale bars are 0.5mm. (a), (b) The heat flux

distributions at different times after impact and the transient maximum heat flux near the inner contact line region with an initial substrate temperature of 50°C at $We = 2.6$. Note the different time scale as compared to Figure 3-12. (c), (d) Same data, but for an initial substrate temperature of 65°C at $We = 2.4$.

3.4 Surface roughness effect

The surface roughness has a significant influence on the droplet dynamics during impact. In particular, a higher surface roughness slows down the spreading velocity and reduces the maximum spreading diameter¹⁵⁰, which leads to a reduced heat transfer area. As shown in Eq. 3.22, the total transferred heat is strongly dependent on the maximum spreading factor of the droplet. Hence, the total transferred heat of a droplet impacting a smooth surface is expected to be larger than impacting a rough surface based on the different hydrodynamics. Furthermore, the liquid-solid interfacial resistance is expected to differ: for a non-wetting Cassie-Baxter surface, the interfacial resistance increases due to the small air pockets trapped inside the microstructures and should consequently reduce the heat transfer capacity¹⁵¹. On the other hand, for a wetting Wenzel state, the roughness increases the liquid-solid interface contact area and decreases the Kapitza resistance, which should lead to an enhanced heat transfer rate¹⁵².

To explore the effect of surface roughness on the heat transfer during droplet impact, we fabricated a rough Teflon AF surface to compare it with the original smooth surface. The rough sample uses a spin-coated 8 μm thick layer of black paint (Testors 18PK, Black Enamel, 1149TT) as the IR transducer. The surface roughness of Testor black paint is significantly higher than the SPB 100 black paint that we used for the previous experiments. On top of the black paint layer, a 150 nm thin chromium film was deposited using physical vapor deposition, serving as the heater. The Teflon AF was then spin-coated using the same method as the original smooth sample. The surface topographies of the two Teflon AF surfaces were measured by atomic force microscopy (AFM) and are shown in Figure 3-16 (a). The rough surface has a much larger

surface roughness in both R_a and R_z : For the smooth surface, we find $R_a = 0.3 \text{ nm}$, $R_z = 1.9 \text{ nm}$, whereas the rough surface has $R_a = 85 \text{ nm}$, $R_z = 0.4 \text{ }\mu\text{m}$. The contact angles of this rough Teflon surface are $\theta_{eq} = 116^\circ$, $\theta_{ad} = 128^\circ$, and $\theta_{re} = 71^\circ$ (as a reminder, for the smooth surface, $\theta_{eq} = 115^\circ$, $\theta_{ad} = 126^\circ$, and $\theta_{re} = 111^\circ$). The contact angles indicate that the water on the rough Teflon AF surface is in a partially wetting Cassie-Baxter state.

Figure 3-16 (b) shows the maximum spreading factor of droplets impacting on the smooth and rough surfaces at room temperature. As we expect, the droplet on the smooth surface has a larger spreading factor than on the rough surface at the same impact Weber number. The higher friction on the rough surface leads to a larger viscous dissipation, which reduces the kinetic energy available for the droplet to overcome the capillary force and spread. As the Weber numbers increase, the difference in maximum spreading diameter decreases.

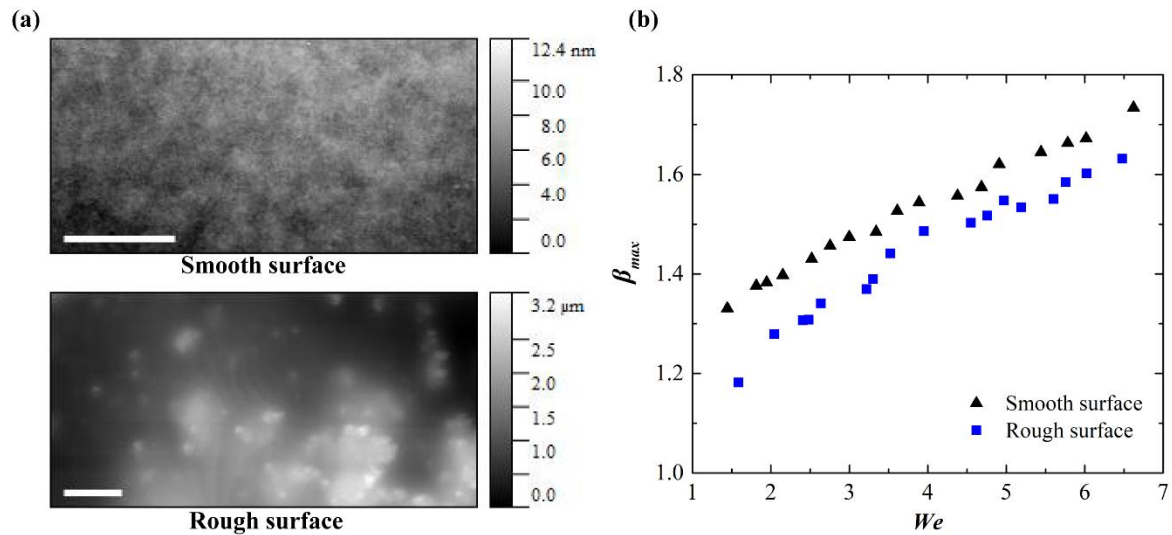


Figure 3-16 Surface topography and droplet spreading on the smooth and rough Teflon AF surfaces. (a) AFM surface topography images of the smooth Teflon AF surface (top) and the rough Teflon AF (bottom), with scale bars of $5\mu\text{m}$. (b) The maximum spreading diameter, β_{max} , of droplet impact on the two surfaces at different impact Weber numbers.

The influence of surface roughness on the interfacial thermal resistance is quantified by comparing the area-weighted average heat flux (similar to Figure 3-6) and surface temperature change of the two surfaces, and plotted in Figure 3-17. The smooth surface exhibits a higher average heat flux during spreading and higher maximum heat flux at both impact Weber numbers. These results indicate that the interfacial thermal resistance of a smooth surface is smaller due to a better contact of the liquid droplet with the substrate. At maximum spreading ($t=4.0$ ms), since less heat has been transferred to the droplet, the interfacial temperature on the rough surface is higher than on the smooth surface, meaning heat transfer (or substrate cooling) is not as efficient. While the average heat flux decreases rapidly on the smooth surface as the droplet starts retracting, the average heat flux decreases slower on the rough surface due to the higher interface temperature and lower retraction velocity. At longer times, however, due to droplet pinning on the rough surface (the droplet retracts to only 60% of the maximum spreading diameter), the rough surface has a higher average heat flux and a lower substrate temperature.

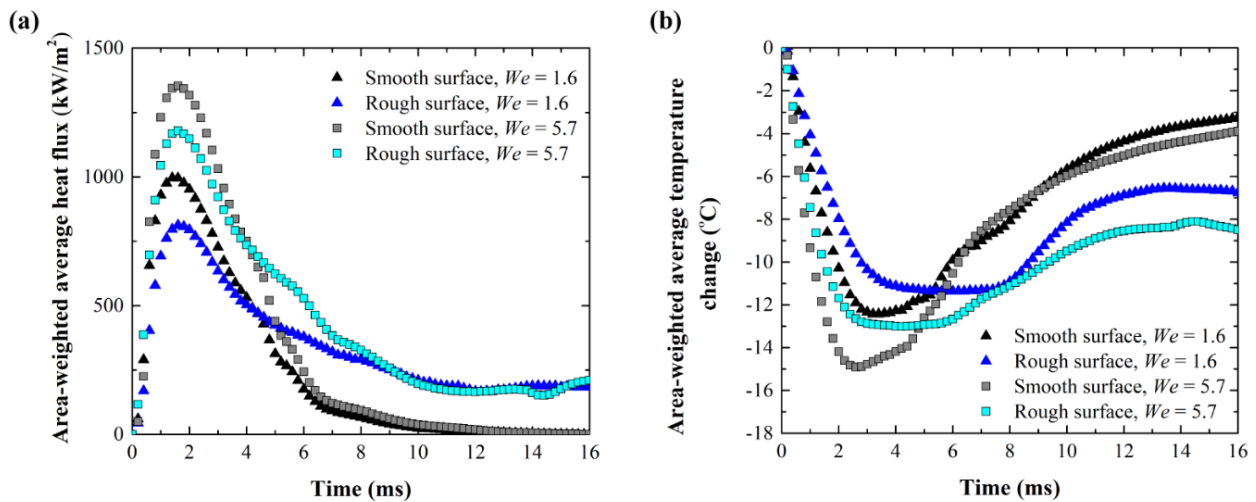


Figure 3-17 Droplet impact on smooth and rough Teflon AF surfaces with an initial surface temperature of $65 \pm 0.5^\circ\text{C}$ (a) Transient behavior of the area-weighted average heat flux. (b) Change of the area-weighted average temperature.

3.5 Conclusion

This study experimentally investigated low Weber number droplet impact on heated hydrophobic surfaces. The experiments were performed using synchronized high-speed optical and high-speed IR imaging to capture the droplet dynamics and the corresponding heat transfer process at the liquid-solid interface. We can draw the following conclusions:

- 1) For droplet impact on a smooth hydrophobic surface, the local contact line heat flux increases quadratically with increasing contact line velocity. At the early receding stage, the local heat flux and contact line velocity go through a transition. At the late receding stage, the contact line heat flux is nearly constant and smaller in magnitude than during spreading.
- 2) For a given initial substrate temperature, a scaling law $Q \propto D^{1.25}v$, based on 1-D transient conduction, is proposed and experimentally validated for the total transferred heat for fully rebounding droplets on smooth hydrophobic surfaces.
- 3) The hydrodynamics and heat transfer of receding-stage bubble entrapment are explored. Higher substrate temperatures narrow the Weber number range where bubbles occur. Due to the low thermal conductivity of air, the substrate temperature underneath the bubble is significantly higher than the surrounding liquid-covered area. During receding, the local heat flux at the inner contact line remains stable but continuously decreases at the retracting outer contact line. At the later stages of receding, the heat flux at the inner contact line surpasses that of the primary outer contact line. Despite enhanced evaporation at the contact lines, the total heat transfer Q is reduced by 5.6% and 7.1% at surface temperatures of 50°C and 65°C, respectively, for droplets with bubbles due to a

reduced liquid-solid contact area. This highlights the dominance of conduction to the overall heat transfer.

- 4) Surface roughness leads to a smaller maximum spreading and consequently a smaller heat transfer area compared to a smooth surface. Furthermore, heat transfer is reduced due to a larger interfacial thermal resistance on the rough surface. However, at longer times, due to pinning, the total transferred heat is larger on the rough surface than on the smooth one.

Overall, for droplet impact on heated hydrophobic surfaces, we show that the heat transfer at the contact line is related to its velocity. However, on a global (*i.e.*, droplet) scale, conduction heat transfer dominates. Due to the relatively low temperatures and short time scales, the contribution of evaporation to the overall heat transfer is minimal. Both the occurrence of an entrapped bubble and an increase in surface roughness decrease heat transfer due to a reduced liquid-solid contact area.

Chapter 4: Droplet Impact and Leidenfrost

Dynamics on a Heated Post

This chapter is based upon a manuscript currently (as of 09/09/2022) under revision with the *International Journal of Heat and Mass Transfer* (Li, Junhui, and Patricia B. Weisensee.

“Droplet impact and Leidenfrost dynamics on a heated post”).

4.1 Introduction

Research on droplets impacting heated surfaces is motivated by various applications such as spray cooling^{40, 106} and internal combustion engines¹⁰⁷⁻¹⁰⁸. During such non-isothermal droplet impact, the hydrodynamics and heat transfer are strongly influenced by the surface temperature¹⁰. At the lowest temperatures, droplet dynamics and phase change are mostly decoupled, with contact-line-dominated evaporation taking place after droplet deposition^{105, 119}. When the surface temperature is higher than the liquid saturation point, the droplet undergoes nucleate boiling and the phase change can have a pronounced effect on droplet dynamics and heat transfer characteristics¹⁵³. Surface cooling is most efficient in this temperature range. Ultimately, if the surface temperature is higher than the Leidenfrost temperature, T_L , the droplet remains separated from the hot solid surface by a developing vapor layer, which acts as a thermal barrier and significantly reduces the heat transfer¹²⁻¹³. The droplet dynamics and T_L are influenced by a number of parameters, including wettability¹⁵⁴⁻¹⁵⁵, surface roughness¹⁸, solid surface thermal conductivity¹⁵⁶, ambient pressure¹⁵⁷⁻¹⁵⁸, and types of fluids¹⁵⁹. For example, for droplet impact on a hydrophilic surface, T_L is increased when compared to a non-wetting counter-part, since the viscous dissipation from a larger contact area requires higher superheat to trigger rebounding dynamics and a stable film boiling state¹⁵⁴. On the other hand, T_L and the cooling capacity

decrease at substrate with a higher thermal conductivity, due to a higher interface temperature that increase the vapor thickness ¹⁵⁶.

In addition to the temperature, the substrate morphology strongly contributes to the behavior of the impacting droplet ¹⁶⁰. Micro and nanostructured surfaces have been widely studied to explore their influence on heat transfer and T_L ¹⁴⁻¹⁹, as introduced in Chapter 1.3. While small-scale structures influence the impact dynamics through a modification of the vapor dynamics beneath the droplet, a structure with a similar dimension to the droplet induces a complete deformation of the entire droplet shape and thus significantly changes the droplet impact behavior ¹⁶¹. The pinning force caused by sharp edges and the additional contact area between the structure and the liquid also influences the droplet profile ¹⁶²⁻¹⁶³. Several studies investigated the hydrodynamics for droplet impact on solid stand-alone structures at isothermal conditions where heat transfer is neglected ^{161, 164-166}. For example, Ding *et al.* ¹⁶⁷ studied the droplet impact dynamics on single-post superhydrophobic surfaces and found that the rebound and breakup morphologies are dependent on impact Weber number and the ratio between droplet and post diameters. For droplet impact on a cubic pillar, air entrapment around the pillar side faces occurs and varies with the exact impact location on the pillar ¹⁶⁵.

In the case of a heated substrate, one would expect this gas entrapment and the altered rebound and breakup dynamics to have a significant influence on the heat transfer between droplet and substrate by serving as nucleation sites for vapor bubbles, preventing or promoting droplet departure, and influencing the Leidenfrost temperature. Furthermore, for impact on a millimetric cylindrical post, the relatively large structure is expected to not only increase the liquid-solid interfacial area, but also decrease the conduction resistance in the bulk liquid after droplet deposition, effectively enhancing heat transfer rates. Additional advantages of using millimetric

structures made of metal as compared to silicon or nanoparticle-based microstructures are their superior durability, ease of manufacturing, and seamless integration with existing metallic components. However, to the best of the authors' knowledge, the combined effect of droplet impact dynamics, heat transfer, and Leidenfrost dynamics on a heated large-scale structure remains unknown. In this chapter, we thus investigated non-isothermal droplet impact and Leidenfrost dynamics on a single post structure on an aluminum surface, which is easily fabricated using traditional machining methods, and compared them to impact on a flat surface. The droplet lifetime and the Leidenfrost temperature were analyzed. Typical droplet impact and boiling modes, as well as the breakup morphologies, were observed and classified for Weber numbers ranging from 10 to 120 and surface temperatures between 120 °C and 330 °C. The cooling effect of the droplets on the substrates was also quantified by measuring the transient temperature distribution at the bottom of the thin substrates using high-speed infrared (IR) imaging. In addition, droplet dynamics and heat transfer characteristics on an inclined surface were compared to highlight the important contribution of pinning at the post structure on enhancing the cooling efficiency.

4.2 Experimental method

4.2.1 Sample preparation

In this study, two types of aluminum substrates were used: a flat substrate and a (single) post substrate. Both substrates were machined using a Bantam Desktop CNC Milling Machine with a flat-end mill and have a thickness of 1.1 mm (± 0.03 mm). The two substrates share the same surface roughness $R_a = 0.5$ μm and $R_z = 2.1$ μm , as measured by a profilometer (KLA-Tencor Alpha-Step D-100). The equilibrium contact angle of water on the aluminum substrates at room temperature is $\theta_{\text{eq}} = 82^\circ \pm 2^\circ$. The advancing and receding contact angles are measured to be θ_{adv}

$= 108^\circ \pm 2^\circ$, and $\theta_{\text{rec}} = 23^\circ \pm 2^\circ$, respectively. For the post substrate, a cylindrical structure (1 mm \pm 0.03 mm in height and 1 mm \pm 0.03 mm in diameter) was machined at the center of the substrate. The bottom (back side) of the substrates were spray-coated with a ≈ 5 μm thin layer of black paint (Krylon Latex Enamel), which serves as a transducer for IR temperature measurements. No other coatings, which are often prone to degradation¹⁶⁸⁻¹⁶⁹, were applied, as to best represent possible industrial applications, such as spray cooling for metal quenching¹⁷⁰ and in-wheel motor in electric vehicle¹⁷¹.

4.2.2 Experimental setup

A schematic of the experimental setup is shown in Figure 4-1. The aluminum substrates were placed on two heating blocks made from copper, which were embedded with cartridge heaters (1/8" Diameter, 120V, 10W) to provide stable heating power to the substrate. The substrate temperatures ranged from 90°C to 330°C, as measured with a surface-mounted resistance temperature detector (RTD). Thermal insulation was applied surrounding the heated blocks to reduce heat losses and to keep the temperature stable. The side-view shadowgraph images of the impacting droplets were recorded at 1000 to 5000 frames per second (fps) using a Photron Mini AX200 high-speed camera with a Canon MP-E 65 mm f/2.8 1-5X Macro Lens at a spatial resolution of 3.3 $\mu\text{m}/\text{pixel}$. A Telops FAST M3k high-speed mid-wave IR camera, equipped with a 1x long working distance lens (Telops), recorded the thermal signals of the substrates in bottom view at 100 fps to 500 fps with a spatial resolution of 30 $\mu\text{m}/\text{pixel}$. Note that we measured the temperature distribution of the black paint layer (\approx substrate bottom surface temperature) and assumed a uniform temperature through the sample prior to impact due to the high thermal conductivity and small thickness of the aluminum substrates. In reality, there is a small lag in the thermal profile at the bottom of the substrate compared to the droplet-substrate interface ($t \sim$

0.1s), which is not relevant for the purpose of this study. Droplets of de-ionized (DI) water were generated at the tip of a needle (gauge 25) connected to a syringe pump (New Era NE-1000). Droplets with a diameter of 2.7 ± 0.05 mm detached due to gravity from needles mounted at heights between 3 mm and 200 mm, leading to impact velocities ranging from 0.5 m/s to 1.8 m/s ($We \approx 1.5 \sim 120$), as determined from the analysis of side-view high-speed sequences of droplets just prior to impact. The corresponding Weber numbers, defined as $We = \rho \frac{Dv^2}{\sigma}$, where ρ , σ are the density and surface tension of water at room temperature, D is the droplet diameter, and v is the droplet velocity right before impacting the surface, are between 1.5 and 120.

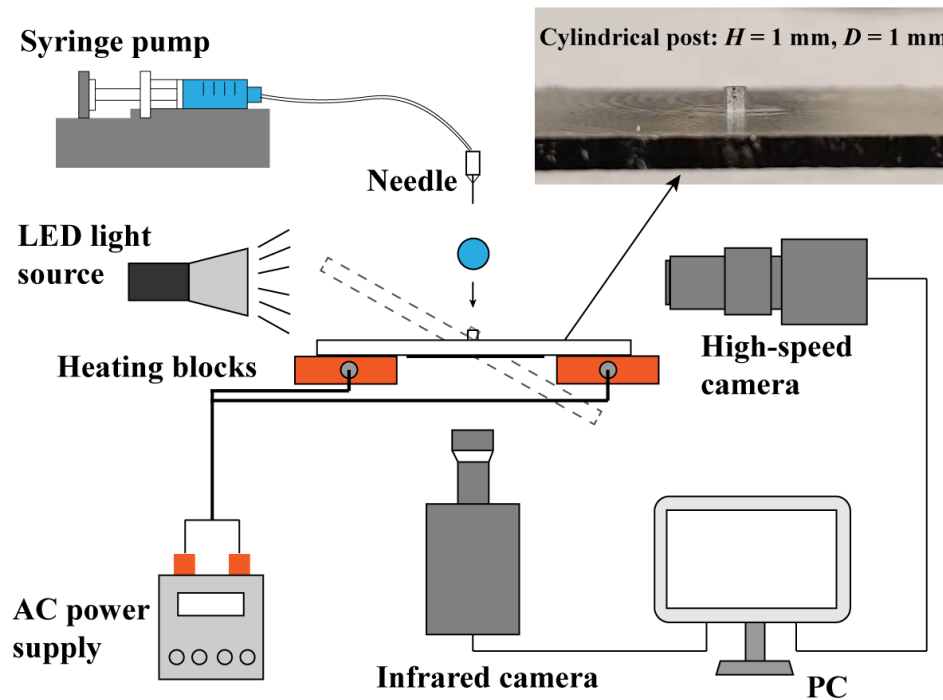


Figure 4-1 Schematic of the experimental setup

4.2.3 Uncertainty analysis

The impact velocity and initial droplet size measurements were derived from analyzing the pixel variance of the droplets in the high-speed videos using the software “Tracker”. We estimate an error of ± 2 pixels for the droplet size, which causes an uncertainty in the droplet diameter of less

than 1%, and ± 2 pixel/s for the impact velocity. As a result, the uncertainties of the impact velocities are estimated to be 0.5% to 2.0%.

The nominal resolution of the temperature readout of the IR camera sensor is 25 mK. The IR-measured temperature was calibrated for all the samples using a thin film RTD sensor (Omega, Pt100) with an accuracy of $\pm 0.1^\circ\text{C}$. The readouts were related to the temperature values measured by the RTD using quadratic curve fittings. Combining these errors together, the uncertainty of the IR temperature measurement is $\pm 0.3^\circ\text{C}$. Each experiment was repeated at least three times (five times for IR) to ensure good reproducibility of the results. The substrate was allowed to reach its steady-state temperature between the successive impact events for single-droplet impact experiments.

4.3 Results and Discussions

4.3.1 Droplet lifetime and Leidenfrost temperature

The droplet evaporation lifetimes at different initial substrate temperatures, T_s , for the flat and post substrates are given in Figure 4-2. In general, as expected¹⁰, the droplet lifetime decreases with an increasing initial substrate temperature before onset of film boiling. For substrate temperatures lower than 105°C , the post substrate shows 10% to 20% shorter droplet lifetimes. In this temperature range, heat transfer is primarily conduction-limited and droplet lifetimes are dictated by droplet evaporation near the triple-phase contact line¹⁰⁵. Due to the small receding contact angle on the bare aluminum surfaces, which prevents the droplet from retracting, evaporation occurs primarily after the droplet has pinned¹⁷². The difference in droplet lifetime is mainly caused by a larger liquid-solid interface area and a lower thermal resistance of the aluminum post (as compared to bulk liquid water), which leads to higher droplet temperatures and faster evaporation¹⁶². For temperatures between 110°C and 150°C , as the droplet enters the

nucleate boiling regime, the heat transfer from vaporization at the liquid-solid interface becomes increasingly important. As the substrate temperature increases, the difference in evaporation times for the different surfaces becomes vanishing small. Droplet dynamics and the cooling capacity in the nucleate boiling regime will be discussed in more detail in Section 4.3.3. Here, we can identify that the substrate temperatures that provide the minimum droplet lifetime for both types of substrates are around 150°C, which correspond to the critical heat flux (CHF) temperature¹⁷³.

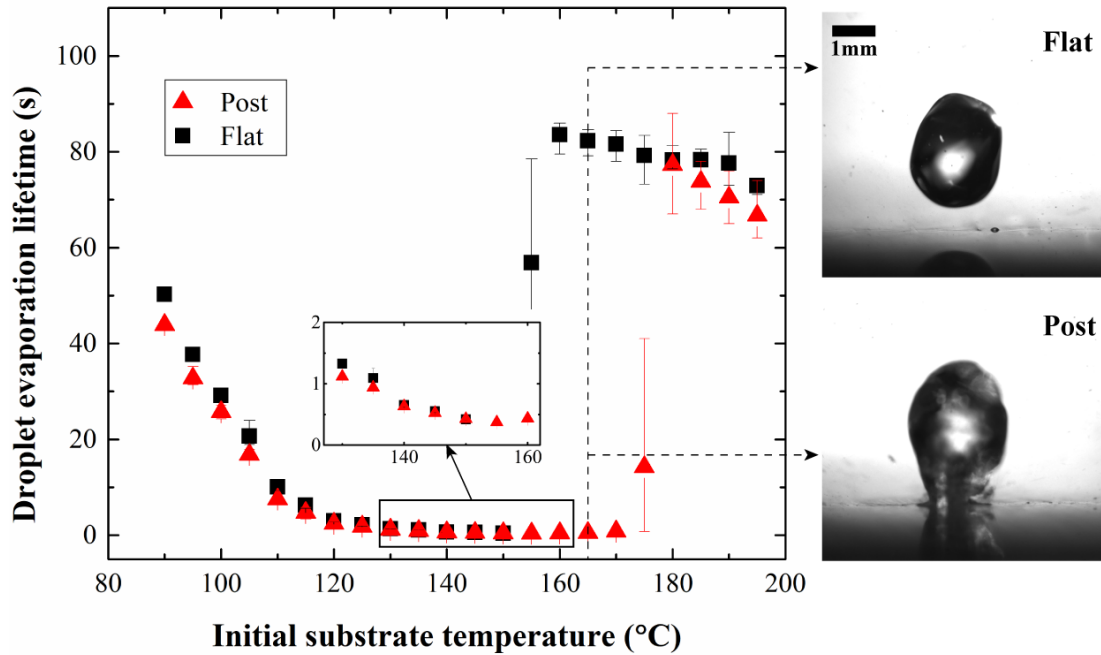


Figure 4-2 Droplet evaporation lifetime on the post and flat substrates at different initial substrate temperatures for $We \approx 1.5$. The snapshots compare typical droplet shapes at $T_s = 165^\circ\text{C}$.

The sudden increase in evaporation time at higher temperatures indicates the transition to film boiling, with a Leidenfrost temperature $T_L \approx 160^\circ\text{C}$ for the flat substrate and $T_L \approx 180^\circ\text{C}$ for the post substrate, respectively. The higher T_L for the post substrate is attributed to a special boiling behavior, which can be understood by looking at typical droplet shapes at $T_s = 165^\circ\text{C}$, as shown in Figure 4-2. At this temperature, the droplet on the flat surface has entered the film boiling

regime, in which a continuous vapor layer separates the liquid droplet from the hot substrate. This vapor layer acts as a thermal insulator, enabling a droplet lifetime of approximately 80s (compared to less than 0.5s at 150°C). On the post substrate, however, the droplet remains pinned around the post structure and remains in partial contact with the horizontal base surface. Atomization is observed around the contact line region, indicating strong vaporization at the base. The droplet shows a “candle” shape without lifting off the post and completely vaporizes in around 0.5s.

Figure 4-3 shows the detailed droplet dynamics on the two substrates at $T_s = 165^\circ\text{C}$. On the flat surface, after the spreading process ($t = 5.0$ ms), the droplet slowly de-wets the surface and fully lifts off around $t = 60.0$ ms. Then the droplet enters the Leidenfrost (film boiling) regime and departs from the initial impact location. The vapor layer in the Leidenfrost regime blocks the heat transfer and extends the droplet lifetime to around 80 s. On the post substrate, the droplet covers the post after impact and the liquid film always covers the post structure ($t = 5.0$ ms). After $t = 50.0$ ms, the droplet shows a “candle” shape until it fully evaporates. Due to a thin liquid layer and strong local vaporization, atomization is observed around the contact line region (seen in the video). The droplet remains pinned at the post structure and vaporizes quickly with a lifetime around 0.6 s.

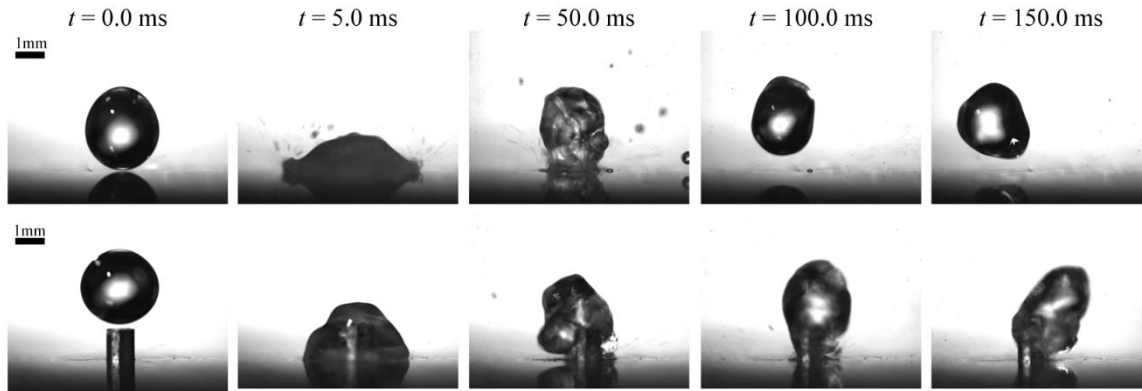


Figure 4-3 Image sequence of droplet impact on a flat (top) and a post (bottom) substrate at $T_s = 165^\circ\text{C}$.

This interesting boiling behavior on the post substrate is attributed to a mixed boiling mode of the droplet. On the base substrate surrounding the post, the temperature is higher than the Leidenfrost temperature of the flat surface (160°C). The liquid-solid interface there is consequently in the film boiling mode, in which the droplet detaches from the surface. However, since the post is entirely engulfed by the droplet, its temperature is decreased by the surrounding water body, allowing for nucleate boiling rather than film boiling towards its top. The temperature decrease along the post can be estimated using an analytical model based on the heat conduction equation. Figure 4-4(a) shows the schematic of the boundary conditions. Several assumptions can be made to simplify the problem. First, we assume a 1-dimensional (1D) temperature distribution along the vertical direction due to the aluminum's high thermal conductivity and the axisymmetric design. Second, the sidewall and top surfaces experience (nucleate) boiling and have the same constant heat convection boundary condition, which can be estimated using the lifetime, total energy (sensible and latent heat), and contact area of the droplet. Third, an isothermal boundary condition with the temperature equal to the initial steady-state substrate temperature is assumed at the bottom of the post. Additionally, we assume temperature-independence of thermophysical properties.

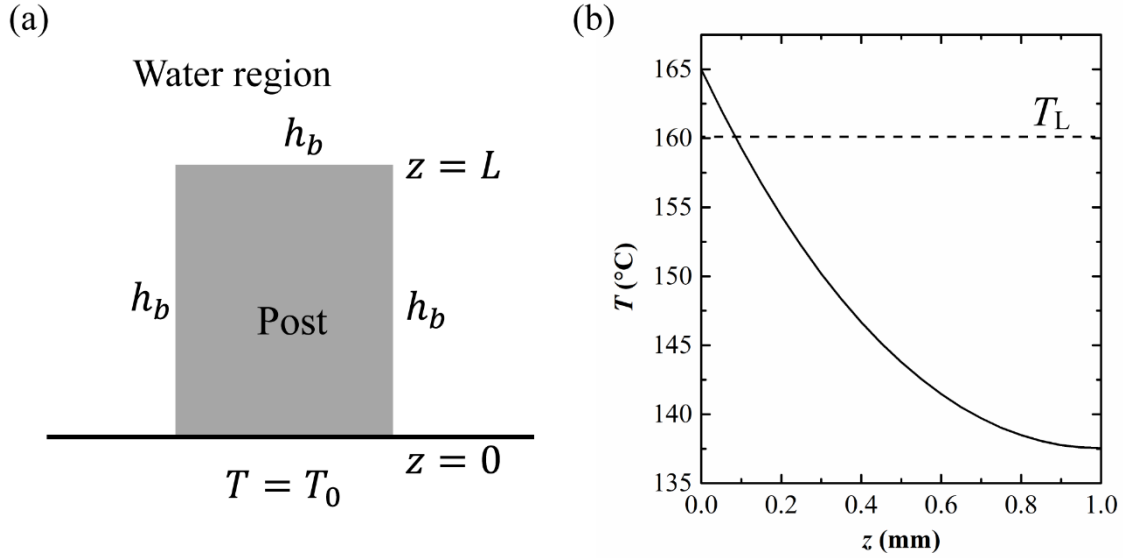


Figure 4-4 Analytical model to estimate the temperature distribution along the cylindrical post. (a) The boundary conditions of the 1D heat equation. (b) Estimated temperature distribution along the post for $T_s = 165^\circ\text{C}$ using Eq. 4.4. The dashed horizontal line represents the Leidenfrost temperature of the flat surface.

With these assumptions, the 1D heat conduction equation along the post can be written as,

$$k \frac{\partial^2 T}{\partial z^2} - h_b(2\pi R)(T - T_{sat}) = \frac{1}{\alpha_t} \frac{\partial T}{\partial t}, \quad (4.1)$$

where k is the thermal conductivity of the aluminum post, h_b is the heat transfer coefficient of the solid-liquid interface, R is the radius of the post, T_{sat} is the saturation temperature of water, and α_t is the thermal diffusivity of the aluminum post. The second term on the left hand side represents the heat convection from the sidewalls of the cylindrical post, which is determined solely by the local wall superheat ($T - T_{sat}$), since h_b is assumed to be constant.

From a previous study¹⁷⁴, we know that the time scale of this transient process can be estimated as

$$\tau^* \approx \frac{1}{\alpha(m^2)} \approx 0.01s, \quad (4.2)$$

where $m = \sqrt{2h_b/kR}$ is the fin parameter. This characteristic time scale of conduction is much smaller than the droplet lifetime (> 0.3 s), which means the temperature of the post becomes stable at very early times of droplet evaporation. Therefore, the heat conduction along the post can be simplified to a steady-state problem, and Eq. 4.1 can be written as

$$\frac{d^2\theta}{dz^2} - m^2\theta = 0, \quad (4.3)$$

where $\theta = \frac{T-T_{sat}}{T_S-T_{sat}}$ is the non-dimensional temperature. The general solution of Eq. 4.3 is

$$\theta = ae^{mz} + be^{-mz}, \quad (4.4)$$

where a and b are constants. The boundary condition at the bottom surface is isothermal, *i.e.* $\theta = 1$ at $z = 0$. The convection boundary condition on the top surface can be converted to a one-dimensional form, $k \frac{d\theta}{dz} = C_A h_b \theta$ at $z = L$, where C_A is the area constant that has a value of πR^2 but a unit of 1. With these boundary conditions, the constants become:

$$a = \frac{kme^{-mL} + C_A h_b e^{-mL}}{2km \cosh(mL) - 2C_A h_b \sinh(mL)}, \text{ and} \quad (4.5)$$

$$b = \frac{kme^{mL} - C_A h_b e^{mL}}{2km \cosh(mL) - 2C_A h_b \sinh(mL)}. \quad (4.6)$$

Equation (4.4) along with eqs. (4.5) and (4.6) can then be used to calculate the temperature distribution along the post. Figure 4-4(b) shows the temperature profile of the post for $T_S = 165^\circ\text{C}$ and $h_b \approx 8 \times 10^4 \text{ W}/(\text{m}^2\text{K})$, which is estimated using the average contact area and the droplet lifetime at this temperature. This substrate temperature is higher than the (flat surface) Leidenfrost temperature, while the temperature drop along the post can be over 20°C , leading to mixed boiling modes along the post height: film boiling at its base and nucleate boiling at the

top. The large nucleate boiling area creates plenty liquid-solid interfaces around the post structure, which, due to the hydrophilic nature of aluminum, provide providing a pinning force that prevents the droplet from fully detaching from the post. As a result, the droplet body experiences competing effects from gravity, the lifting force from the bottom surface due to rapid vaporization, and the pinning force from the post surface, which eventually lead to the observed candle-like shape. The droplet always remains attached to the substrate and thus possesses a much shorter lifetime compared to the droplet on the flat surface.

4.3.2 Boiling regimes and droplet breakup

Figure 4-5 presents time-series images for six different droplet impact and boiling modes on the post surface. Deposition is observed for droplet impact with substrate temperatures lower than 130°C, in which the droplet surface remained smooth, and no bubble or atomization occurred as the droplet spread to its maximum diameter ((a), $t = 5.0$ ms). In the deposition mode, no breakup occurred for the entire Weber number range studied in this work. However, as indicated in some previous studies, one can expect droplet breakup in the deposition mode once $We > 160$ ¹⁵⁵. At higher substrate temperatures, atomization (*i.e.*, the emergence of small satellite droplets) can be observed as the droplet spreads to its maximum diameter, shown in Figure 4-5 (b), (c), and (d). There are two different sources for these small droplets. At relatively lower substrate temperatures ($T_s < 200^\circ\text{C}$), the vapor layer cannot fully levitate the spreading liquid film, which causes the generation of bubbles near the contact line region. These bubbles quickly burst and lead to atomization around the rim during spreading, as shown in (b), $t = 5.0$ ms. This low-temperature atomization is known to appear more easily on hydrophilic surfaces, such as the uncoated aluminum used in this work⁴³. When substrate temperatures are higher ($200^\circ\text{C} < T_s < 300^\circ\text{C}$), the small droplets are mainly ejected from the central region (c and d), indicating that

only the central area of the droplet contacts the solid surface^{143, 175}. The atomization is eliminated when the substrate temperature is higher than 310°C and the droplet enters rebound (e) or rebound with breakup (f) regimes. The droplet immediately enters the film boiling regime and the vapor layer prevents the droplet from contacting the solid surface. In addition to temperature, the Weber number plays an important role in determining the breakup behavior of the droplet. For the same substrate temperature, the droplet breaks up when the impact Weber number is larger than a certain threshold. Comparing (e) and (f), we can conclude that a higher Weber number provides a larger spreading diameter, preventing the droplet from recoiling back to a single body.

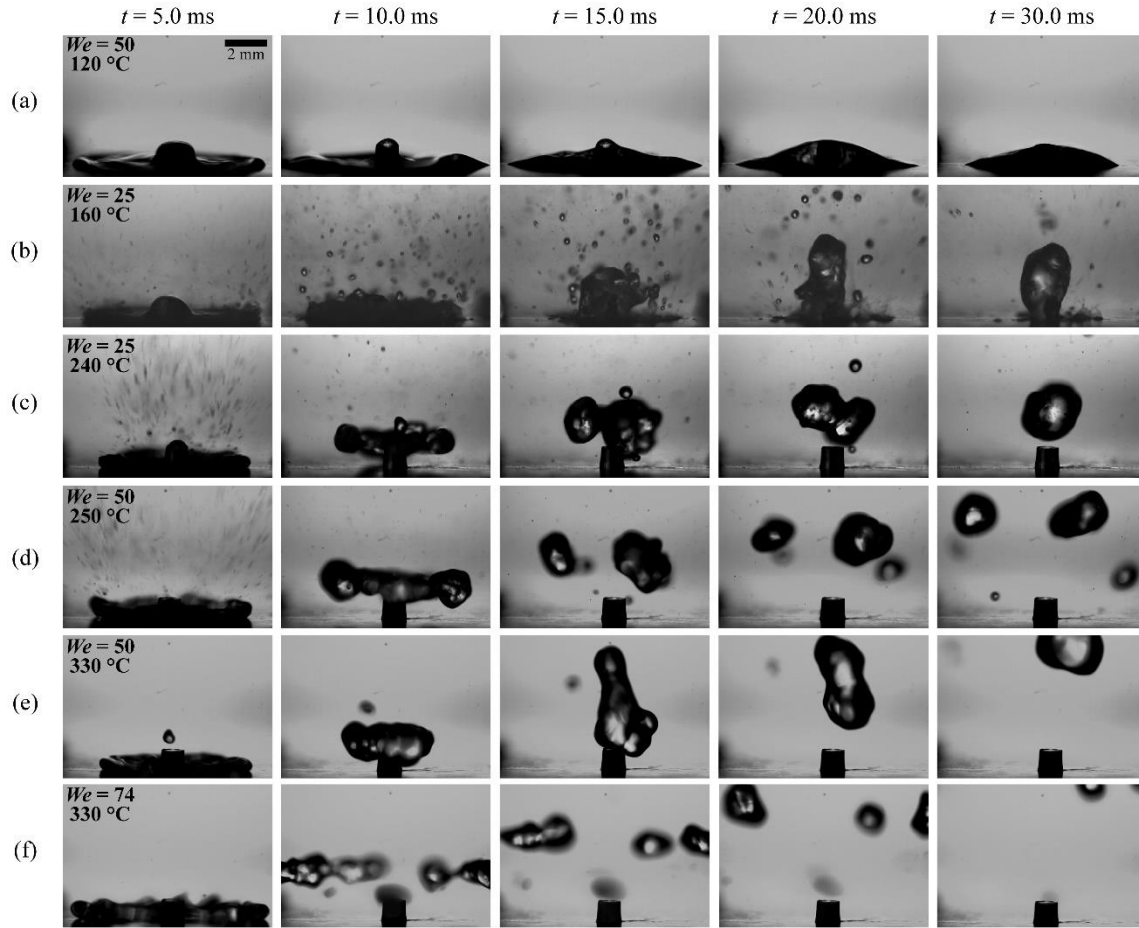


Figure 4-5 Typical water droplet dynamics and boiling modes on the post substrate. (a) Deposition at $We = 50$, $T_S = 120^\circ\text{C}$; (b) Atomization at $We = 25$, $T_S = 160^\circ\text{C}$; (c) Rebound with atomization at $We = 25$, $T_S = 240^\circ\text{C}$; (d) Breakup with atomization at $We = 50$, $T_S = 250^\circ\text{C}$; (e) Rebound at $We = 50$, $T_S = 330^\circ\text{C}$; (f) Breakup at $We = 74$, $T_S = 330^\circ\text{C}$.

As seen above, the droplet impact and boiling behaviors strongly depend on Weber numbers and surface temperatures, which can be best quantified using a We - T_S regime map, as shown in Figure 4-6 for droplet impact on the post and flat substrates, respectively. Compared to the flat substrate, the regime map of the post substrate shows two major differences. First, the temperature limit for the “rebound with atomization” regime (orange dashed lines) is higher than for the flat substrate, which is attributed to the additional nucleate boiling sites around the post surface, as explained in the previous section. Second, the droplet breakup (black dashed lines) occurs at a lower Weber number on the post substrate, especially at the temperature ranges of

170°C to 200°C and 290°C to 330°C. This observation indicates that the post structure enhances droplet breakup at multiple temperature ranges. On the post substrate, interestingly, droplet dynamics switch forth and back between breakup and rebound regions at Weber numbers ranging from 50 to 60 and at temperatures between 190 °C and 230 °C. This phenomenon is much weaker on the flat surface.. Around 210°C, rebound is sustained to higher Weber numbers than expected. This counterintuitive influence of the post structure on droplet breakup requires a detailed analysis of the droplet dynamics.

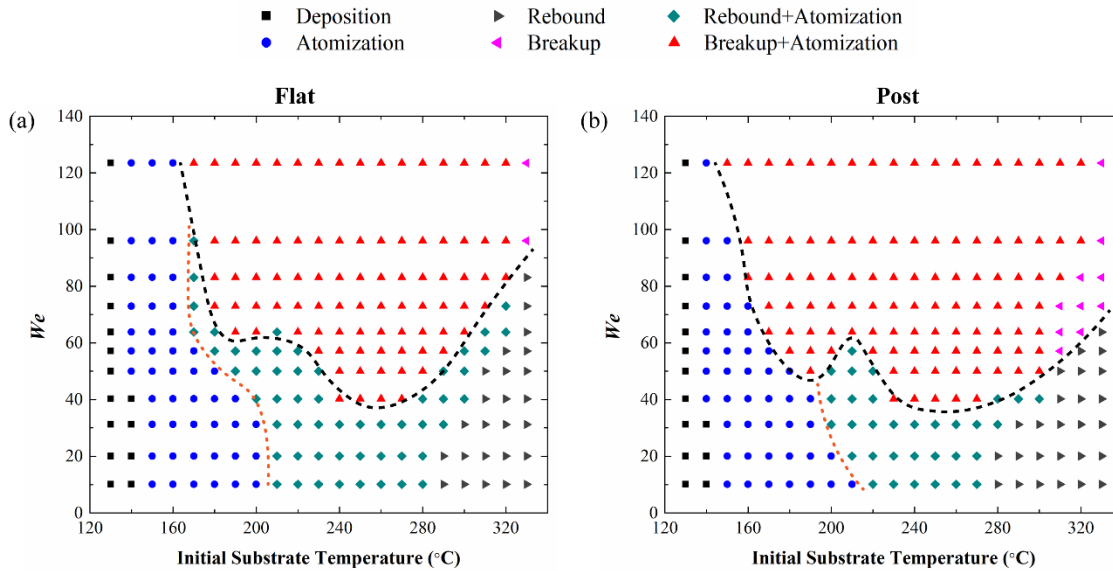


Figure 4-6 $We-T_s$ regime maps for droplet impact on (a) a post substrate and (b) a flat substrate. Six different impact and boiling modes are observed. The orange dashed line is a visual guide for the transition between droplet rebound and non-rebound regimes. The black dashed line represents the transition between rebound and breakup regimes.

Figure 4-7 provides insights into the breakup-rebound-breakup transition on the post substrate.

Shown is the temporal evolution of droplet dynamics in side and top views, as well as schematic representations of the processes. The three droplets impact the substrate with the same We number, but at different T_s . At the lower temperature ($\approx 190^\circ\text{C}$), the center of the droplet, which touches the post, experiences nucleate boiling, pinning it in place due to its high wettability, as discussed in Section 4.3.1, while the spreading rim is supported by the vapor layer.

Consequently, the rim experiences very little resistance during spreading, leading to the development of a thin liquid film with decreasing thickness. The shear layer instability with air, which increases as the film thickness decreases, eventually leads to break-up (Figure 4-7(a))¹⁷⁶⁻¹⁷⁷. This droplet pinning along with the low-temperature breakup mode leads to the main droplet being attached to the post and satellite droplets surrounding it. At high temperatures ($> 230\text{ }^{\circ}\text{C}$), the post substrate supports the transition boiling regime where only the central region shows atomization^{45, 178} during spreading (**Error! Reference source not found.** Figure 4-7(c), $t = 4.0$ ms). However, the central region quickly turns to film boiling before 6.0 ms, as the surface temperature recovers due to continuous heat supply from the substrate. The large droplet detaches from the post structure during the spreading process. Outward inertial forces and the generated vapor work together to drive the liquid film away from the post and create a large central cavity, shown in (c) at $t = 6.0$ ms. Then, as the liquid film disconnects, the whole droplet breaks up into several small droplets, leaving the center post dry. In between these two breakup modes, a transition mode exists ($200 < T_s < 220^{\circ}\text{C}$), in which the droplet does not break up and lifts off the post structure as a whole (Figure 4-7 (b)). In this mode, the droplet is also in the transition boiling regime, but it takes longer for the liquid film to detach from the central post region due to a lower substrate temperature. Instead of a detachment from the post during the spreading process, the liquid now de-wets the post during the receding stage. As the rim retracts, the vapor generation at the post is too weak to provide sufficient outward momentum to counteract the inertia from the retracting liquid. Therefore, as the droplet starts to recoil due to capillary forces, the droplet fully reconnects and lifts-off. Although this discontinuity of breakup can be found only in a small range of We numbers, it reveals that the interplay between surface morphology and temperature plays a critical role in determining droplet dynamics.

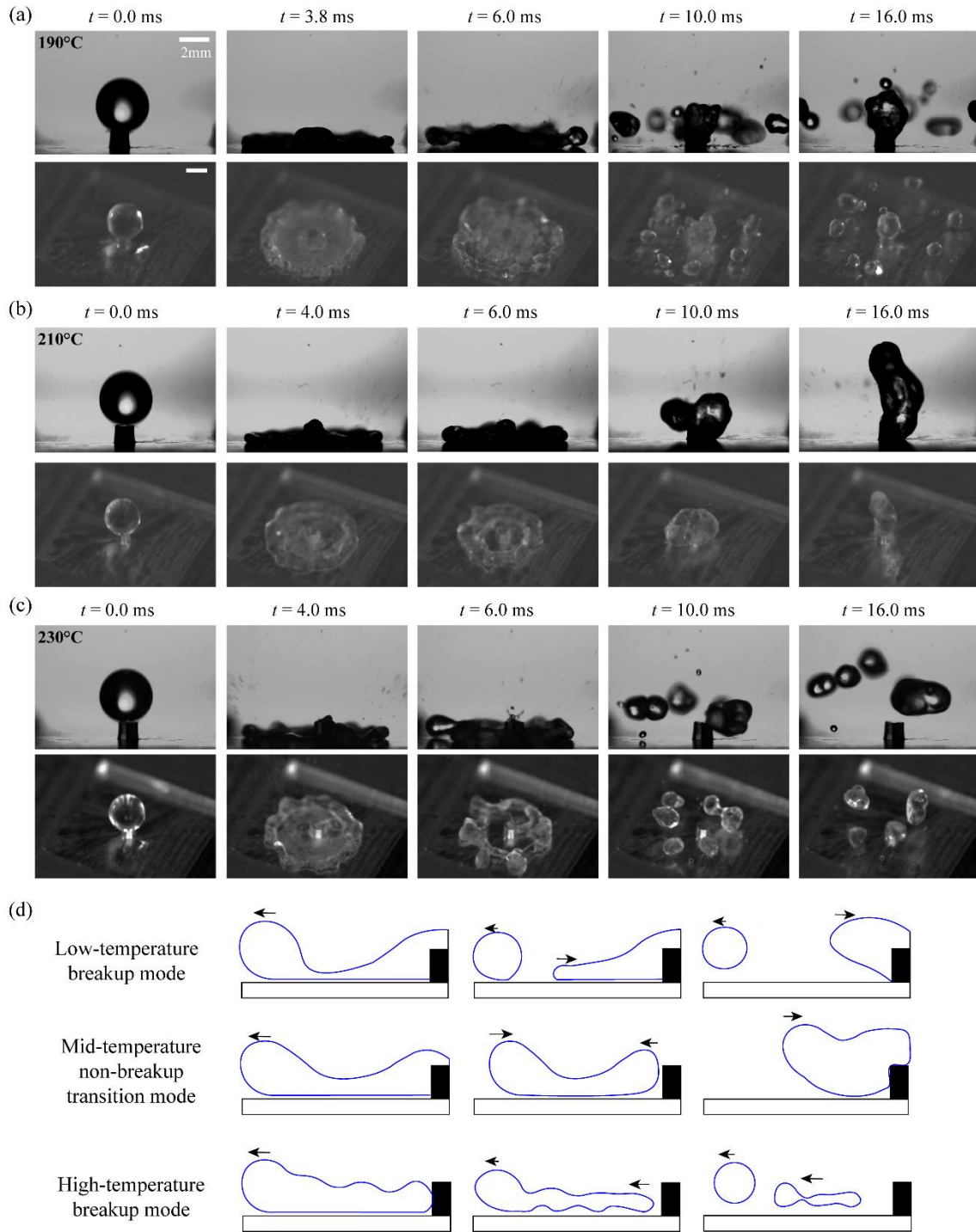


Figure 4-7 Comparison of droplet (breakup) dynamics for different substrate temperatures (all at $We \approx 57$). (a) Low-temperature breakup mode at $T_s = 190^\circ\text{C}$. (b) Mid-temperature non-breakup transition mode at $T_s = 210^\circ\text{C}$. (c) High-temperature breakup mode at $T_s = 230^\circ\text{C}$. (d) Schematics of the different breakup mechanisms.

After investigating the two different breakup mechanisms on the post surface, we can now revisit the $We-T_s$ regime map (Figure 4-6) and better understand the transitions in droplet modes for the flat and post surfaces, respectively. The post substrate shows an earlier breakup (smaller We) between 170°C and 200°C, which corresponds to the low-temperature breakup mode. For the temperature range of 290°C to 330°C, the high-temperature breakup mode also causes breakup at a lower We . Figure 4-8 shows the droplet dynamics on the flat and post surfaces at 180°C and 320°C, respectively. On the flat substrate, the droplet spreads to a certain maximum diameter ((a) $t = 6.0$ ms) and then fully recoils and lifts off. On the post substrate, however, the droplet spreads to a slightly larger maximum diameter ((b) $t = 6.0$ ms) and finally ends up with a central droplet attached to the post surrounded by satellite droplets ((b), $t = 16$ ms). We hypothesize that the volume of the post at the center causes the droplet to stretch to a larger spreading diameter than on the flat surface, which leads to a thinner film that enhances the breakup. Figure 4-8 (c) and (d) correspond to the high-temperature breakup mode. On the flat substrate, the droplet maintains a thin liquid layer across the entire width of the spread droplet, as shown in (c) $t = 6.0$ ms. This thin liquid layer prevents the disintegration of the liquid body, which enables non-breakup rebound. However, on the post substrate, we notice a separation of the liquid film and eventual breakup where the post “pierces” the liquid film. This separation is caused by the vapor generation at the post surface that leads to a cavity expanding radially from the center ((d) $t = 6.0$ ms).

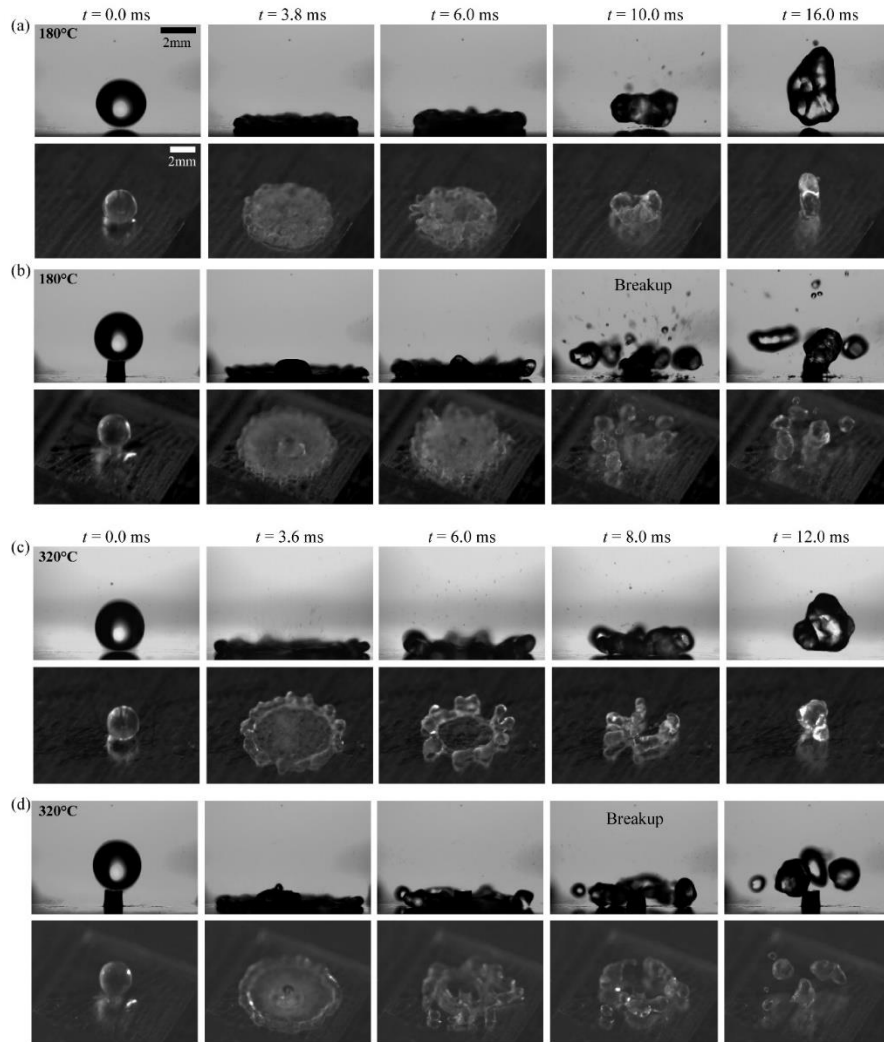


Figure 4-8 Image sequence of the droplet impact at $We \approx 57$ on (a) a flat substrate at $T_S = 180^\circ\text{C}$, (b) a post substrate at $T_S = 180^\circ\text{C}$, (c) a flat substrate at $T_S = 320^\circ\text{C}$, and (d) a post substrate at $T_S = 320^\circ\text{C}$. The top view snapshots are recorded at an angle of approximately 20° from the vertical.

4.3.3 Cooling capacity in the nucleate boiling regime

After discussing the droplet hydrodynamics, we now turn our focus to the more practical aspect of this study: quantifying the influence of the post on the droplet's ability to efficiently cool the surface. Measuring the transient surface temperature of impacting droplets is a common approach for quantifying the cooling capacity of different surfaces¹⁷⁹⁻¹⁸⁰. In this study, we recorded the back-side (bottom) surface temperature of the substrates using high-speed IR

thermography to compare their respective cooling efficiencies. The bottom surface temperature, although it experiences a lag in response time, provides a better metric to quantify the cooling capability due to its better resemblance to real-world droplet impingement applications (such as quenching) and has been used by a number of previous studies¹⁸¹⁻¹⁸³. As shown in Figure 4-2, the droplet lifetime on the two substrates becomes very similar for $120^{\circ}\text{C} < T_s < 150^{\circ}\text{C}$. The measurement of the bottom surface temperature can thus provide better and direct evidence to compare the cooling capacities between the two substrates in the nucleate boiling regime.

Figure 4-9 shows the area-weighted average temperature evolution of the impact area ($8\text{ mm} \times 8\text{ mm}$) at the bottom of the substrates for four different initial temperatures. We choose the non-dimensional time $t^* = t/t_0$, where t_0 is the time of full evaporation on the post substrate (compared to Figure 4-2), to present the temperature history. For all four cases, the temperature decreases rapidly as the droplet impacts the surface and gradually recovers due to a continuous heat supply from the two heating blocks and the reduced heat loss to the vanishing droplet. A larger temperature drop indicates that the droplet removes more heat from the substrate and hence has a higher cooling capacity. The post surface has a 40% and 22% higher maximum temperature drop for $T_s = 110^{\circ}\text{C}$ and $T_s = 130^{\circ}\text{C}$, respectively. However, as the initial substrate temperature increases, the difference in cooling capacity becomes negligible between the post and flat surfaces ($< 8\%$ difference in temperature drop). These results match those of the droplet lifetime shown in Figure 4-2, where droplets evaporate faster on the post than the flat substrate at 110°C and 130°C , but have a similar lifetime at 150°C . The two substrates show a tremendously different temperature history at 165°C , though, which is attributed to the Leidenfrost effect on the flat substrate where the vapor layer significantly blocks the heat transfer. As discussed in

Section 4.3.1, the post enables droplet pinning at this temperature, leading to a significantly enhanced cooling capacity.

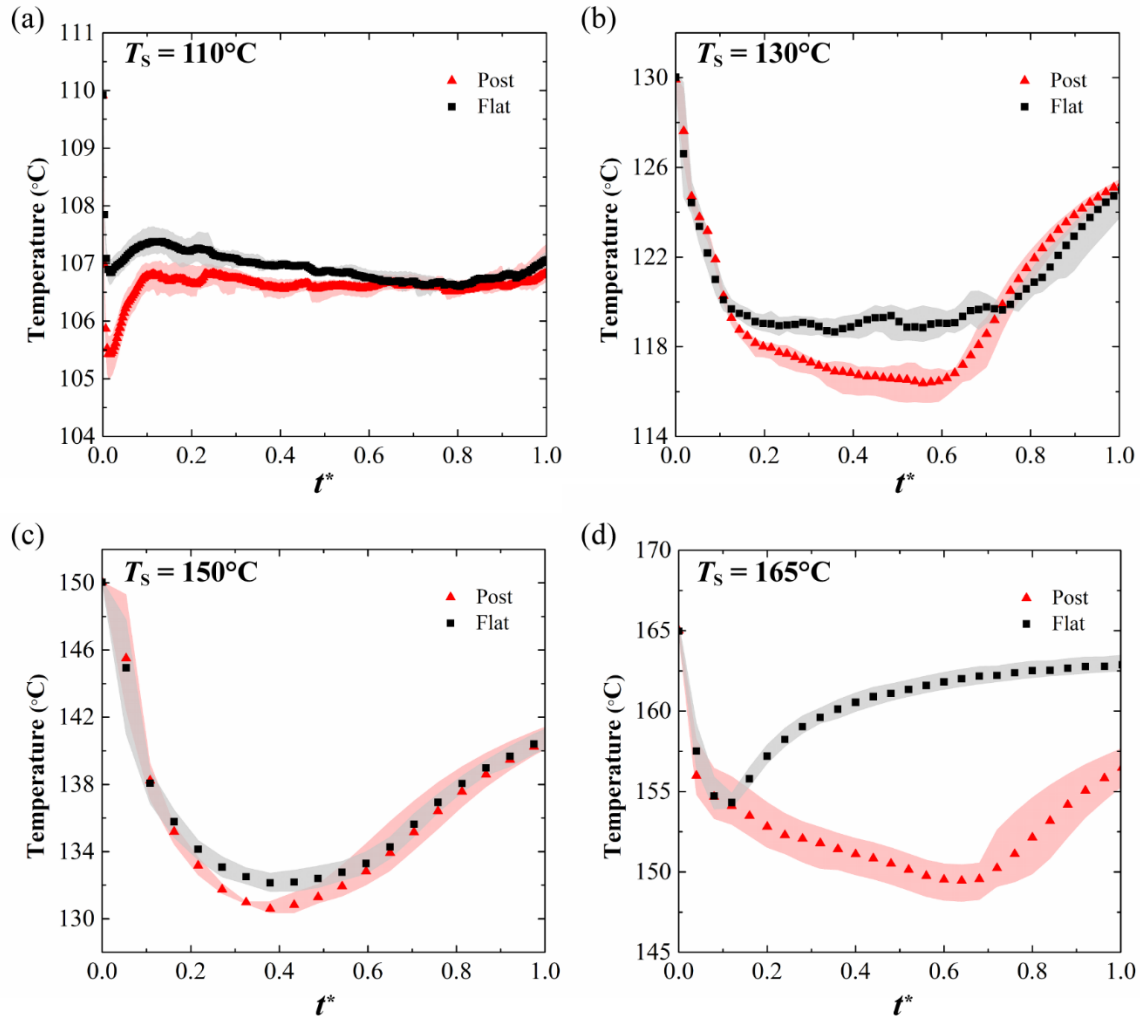


Figure 4-9 Area-weighted average bottom-surface temperatures for (a) $T_s = 110^\circ\text{C}$, (b) $T_s = 130^\circ\text{C}$, (c) $T_s = 150^\circ\text{C}$, and (d) $T_s = 165^\circ\text{C}$. within the droplet lifetime on the post substrate. The x-axis is the non-dimensional time $t^* = t/t_0$, where t is the real time and t_0 is the droplet lifetime on the post substrate. For all the experiments, droplets were initially at room temperature ($\approx 25^\circ\text{C}$) and impacted the substrates with $We \approx 20$.

To investigate the differences of the temperature curves in the nucleate boiling regime, and especially the nearly identical profiles in Figure 4-9 (c), we analyze the bubble generation and the droplet profile through high-speed imaging, shown in Figure 4-10. At $T_s = 110^\circ\text{C}$ (Figure 4-10 (a)), the droplet on the flat substrate experiences a gentle nucleate boiling, in which the

generation and coalescence of small vapor bubbles lead to a slight deformation of the droplet shape but no significant lateral expansion, *i.e.*, the total projected contact area remains approximately constant. On the contrary, the droplet on the post substrate generates larger vapor bubbles and undergoes a foaming process as the bubbles accumulate and attach to the post, which ultimately leads to an expansion of the droplet-solid contact line ($t^* = 0.1$). The physical mechanism behind this foaming is not yet fully understood¹⁸⁴. It has been suggested that small amounts of dissolved ionic salt in the water prevent bubble coalescence due to electrostatic effects and changes in surface tension¹⁸⁵. In the present case, the post structure provides additional nucleation sites for the bubbles that can pin to the side wall of the post as they growing ($t^* = 0.1$ and $t^* = 0.3$). As a result, the vapor pushes the liquid-solid contact line away from the post, leading to a much larger apparent liquid-solid interface area compared to the flat substrate, where foaming is absent (compare at $t^* = 0.1$). This increase in the contact area enhances the heat transfer, leading to the observed shorter droplet lifetime (Figure 4-2) and lower surface temperature (Figure 4-9) on the post substrate.

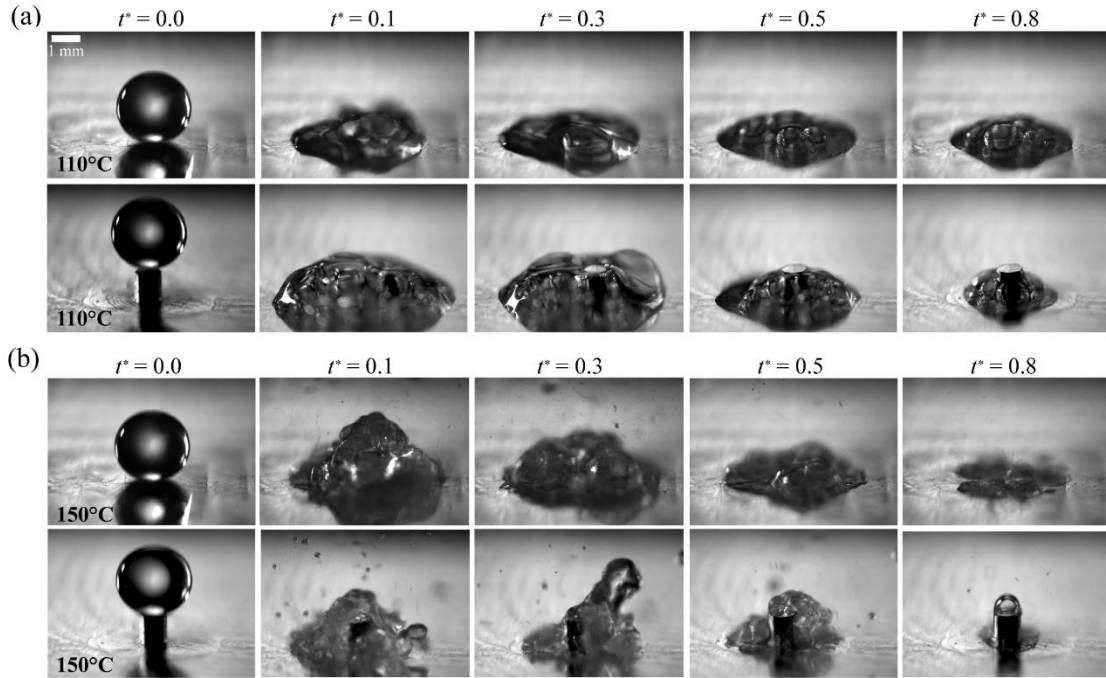


Figure 4-10 High-speed snapshots of the bubble generation and boiling behavior at (a) $T_s = 110^\circ\text{C}$ and (b) $T_s = 150^\circ\text{C}$. The view is tilted from the horizontal by approximately 5° for better visualizations of the post structure and the bubbles inside the droplet.

At $T_s = 150^\circ\text{C}$ (Figure 4-10 (b)), the boiling is vigorous and chaotic on both substrates. The droplet surface is deformed heavily by the intense vapor generation and the atomization near the liquid rim. Except for a slightly more centered droplet on the post substrate, the boiling behavior for the two substrates is quite similar. Due to the distortion of the droplet, the post structure is partially exposed, reducing the influence of the (nominally) additional liquid-solid contact area compared to the flat substrate. This observation explains the minimal difference in the substrate temperatures shown in Figure 4-9 (c). In conclusion, the bubble generation and boiling behavior on the two substrates become increasingly alike between $T_s = 110^\circ\text{C}$ and 150°C , which eventually leads to similar droplet lifetimes and temperature drops at $T_s = 150^\circ\text{C}$.

As mentioned above, the post surface modifies droplet dynamics and nominally has a higher contact, or heat transfer, area than the flat surface. On the other hand, the cylindrical post (= fin)

also poses an additional thermal conduction resistance. A basic heat transfer analysis can help better determine the most influential factors and quantify the cooling capacity enhancement of the post structure.

For the flat surface, we can estimate the convection heat transfer to the droplet with

$$q_{flat} = h_b A_{sl} (T_S - T_{sat}), \quad (7)$$

where A_{sl} is the average solid-liquid interfacial area of the droplet on the flat surface and h_b is the same convection coefficient that we used in Section 4.3.1. The heat transfer rate on a post substrate can be estimated as

$$q_{post} \approx h_b A_p (T_{top} - T_{sat}) + h_b (2\pi RL) (T_{ave} - T_{sat}) + h_b (A_{sl} - A_p) (T_S - T_{sat}), \quad (8)$$

where A_p is the top surface area of the post, T_{top} and T_{ave} are the temperatures at the top of the post and the average temperature of the sidewall of the post, respectively, which can both be calculated using Eq. 4.4. Comparing eqs. (7) and (9) for substrate temperatures of 110°C, 130°C, and 150°C, the post substrate has 24%, 18%, and 15% higher heat transfer rates, respectively, compared to the flat substrate. These results indicate that the improvement of the heat transfer observed in Figure 4-9 stems primarily from the additional contact area between droplet and solid. Due to the high thermal conductivity of the aluminum, the conduction resistance within the post is minimal and the addition of the post can effectively enhance the cooling capacity on the substrate.

Motivated by the post's general superiority in achieving a cooling capacity for a single-droplet impact, we further explored the temperature evolution during multi-droplet impact to identify

whether the improvement can be maintained. Figure 4-11 shows the area-weighted average temperature of the bottom surface temperature at different T_s . A strong temperature drop can be identified once a new droplet impacts the substrate, followed by a recovery as the droplet evaporates. However, if the volume flow rate is much larger than the evaporation rate, the droplets can grow to a very large water body (a water pool). Then, for these flooded samples, we can expect that both the temperature drop and its recovery will be smaller due to the slow temperature change of the water pool. For $T_s = 110^\circ\text{C}$, where the volume flow rate was low enough to prevent flooding, the temperature of the post substrate was always lower than that of the flat substrate, indicating that the post structure continuously increases the heat transfer in this temperature range and enables an efficient increase in cooling capacity. For $T_s = 130^\circ\text{C}$, we can identify a higher temperature drop on the post substrate for the first two droplet impact events. After that, the sample flooded due to a higher volume flow rate compared to the 110°C -case. The flooding minimized the influence of the post and the temperature curves on the two substrates gradually became similar. At $T_s = 150^\circ\text{C}$ the heat supply to the droplet was sufficient to prevent flooding, and – similar to the 110°C -case – the post substrate showed sustained larger temperature drops than the flat substrate. For $T_s = 165^\circ\text{C}$, due to the Leidenfrost effect on the flat surface, the post substrate showed a much lower temperature, as expected. These results demonstrate that the post substrate can promote a higher cooling capacity for multi-droplet impact for as long as the substrate is not flooded.

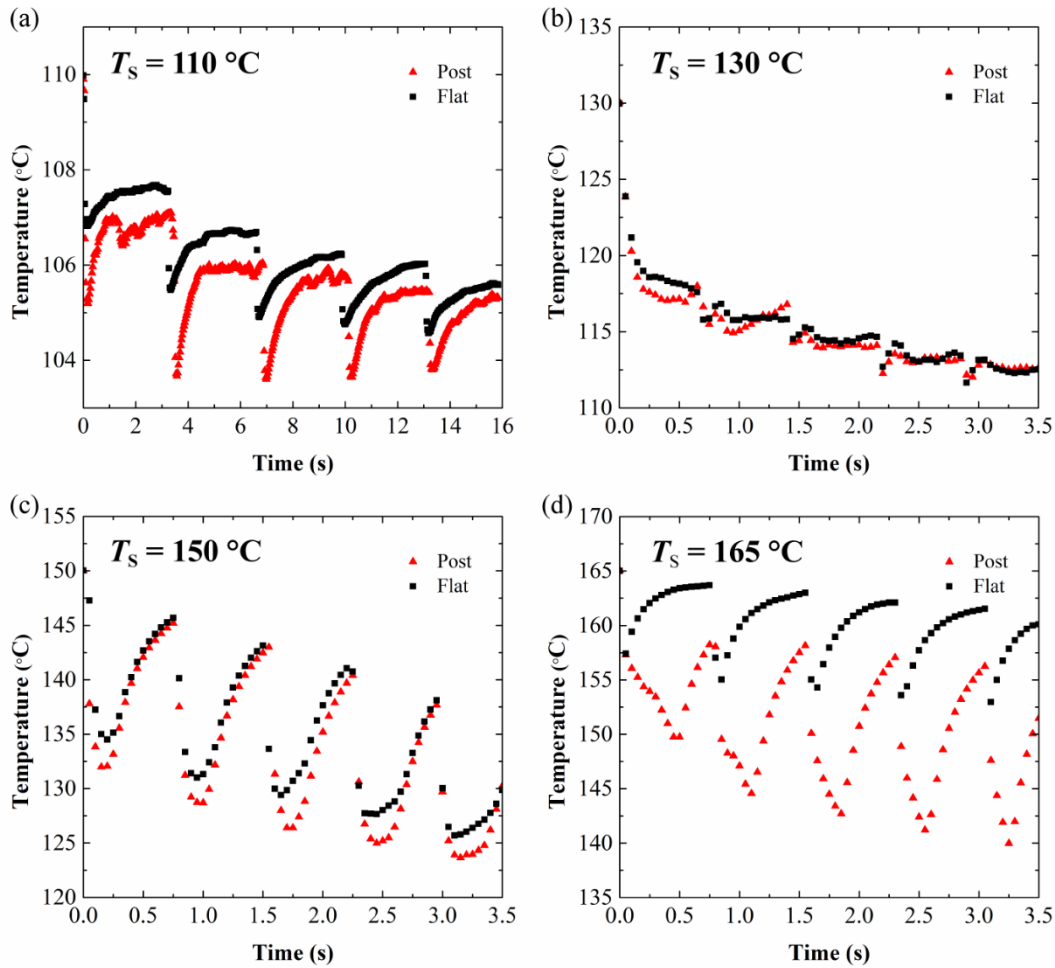


Figure 4-11 Area-weighted average bottom surface temperature for multi-droplet impact at (a) $T_s = 110^\circ\text{C}$, (b) $T_s = 130^\circ\text{C}$, (c) $T_s = 150^\circ\text{C}$, and (d) $T_s = 165^\circ\text{C}$. The volume flow rate is $31.5\text{ }\mu\text{L/s}$ for 110°C , and $137.5\text{ }\mu\text{L/s}$ for all other cases. For all the experiments $We \approx 20$.

4.3.4 Droplet impact on inclined surfaces

So far, the hydrodynamics and the cooling capacity of the two surfaces were investigated on horizontal substrates with perpendicular droplet impingement. However, in real applications, droplets often impact solid walls at various inclination angles¹⁸⁶. Previous studies have explored the hydrodynamics of non-isothermal droplet impact on inclined surfaces, including the influence of Leidenfrost effects¹⁸⁶⁻¹⁸⁷, wettability effects¹⁸⁸, and surface roughness effects¹⁸⁹. On a smooth surface, the inclination can cause the droplet to slide or bounce off the substrate, decreasing the local heat transfer at the initial impact location¹⁸⁷. For a post substrate, which

already positively influences impact and heat transfer characteristics when placed horizontally, one can expect even stronger benefits when mounted at an angle.

We investigated droplet impact on the two substrates inclined at 30° from the horizontal and at different initial temperatures. Figure 4-12 provides snapshots of droplet dynamics and the back-side temperature distribution for droplet impact at an initial temperature of $T_s = 145^\circ\text{C}$. As discussed above, there is a slight delay in the IR signature due to the time associated with heat diffusion through the substrate. Nonetheless, the temperature profile still provides an adequate representation of the local cooling as the droplet moves across the top of the surface. On the flat substrate, as expected, the droplet slides down the incline during the spreading and recoil process and finally falls off the substrate. The temperature profile shows an elongated cold spot and that keeps shifting to the left (downhill). On the post substrate, the droplet first spreads asymmetrically due to gravity with the uphill portion of the droplet pinned to the post structure ($t = 20.0$ ms). Then, driven by capillary forces and the pinning provided by post, the droplet returns to the impact location and symmetrically covers the post structure ($t = 44.0$ ms). The temperature profile shows a low-temperature region that evolves radially with time, indicating effective cooling around the impact area.

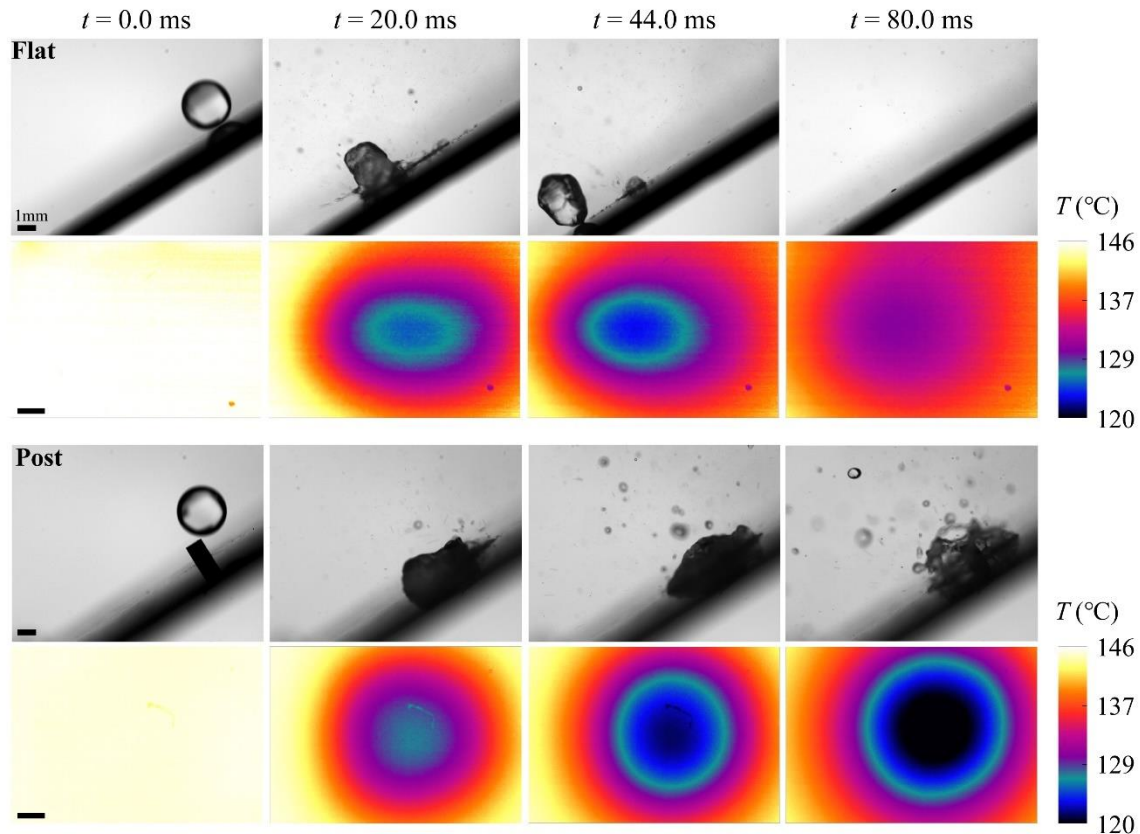


Figure 4-12 High-speed and IR imaging sequence of droplets impacting on the post and flat substrates inclined at 30° at an initial temperature of $T_s = 145^\circ\text{C}$.

Figure 4-13 provides the droplet dynamics and the backside temperature distribution for droplet impact at the initial temperature of $T_s = 160^\circ\text{C}$. Similar to the case of 145°C from Figure 4-12, on the flat substrate, the droplet again slides down the substrate ($t = 10.0$ ms), but then directly bounces off the surface ($t = 25.0$ ms). The back-side temperature briefly decrease around the impact region, followed by a quick recovery after the droplet bounces off the surface ($t = 50.0$ ms). The flat substrate fails to maintain a reasonable cooling performance. On the post substrate, the droplet attaches to the left side of the post due to the mixed effects of pinning and gravity ($t = 10.0$ ms). Compared to a symmetric shape at $T_s = 145^\circ\text{C}$, this asymmetric shape indicates that the base surface almost enters the film boiling regime, where the droplet is levitated by the vapor layer and pins only to the post. Then the droplet remains attached to the left side of the post and

quickly vaporizes ($t = 25.0$ ms, $t = 50.0$ ms). The corresponding temperature profile shows a well-defined low-temperature region, which indicates an effective cooling performance around the impact area.

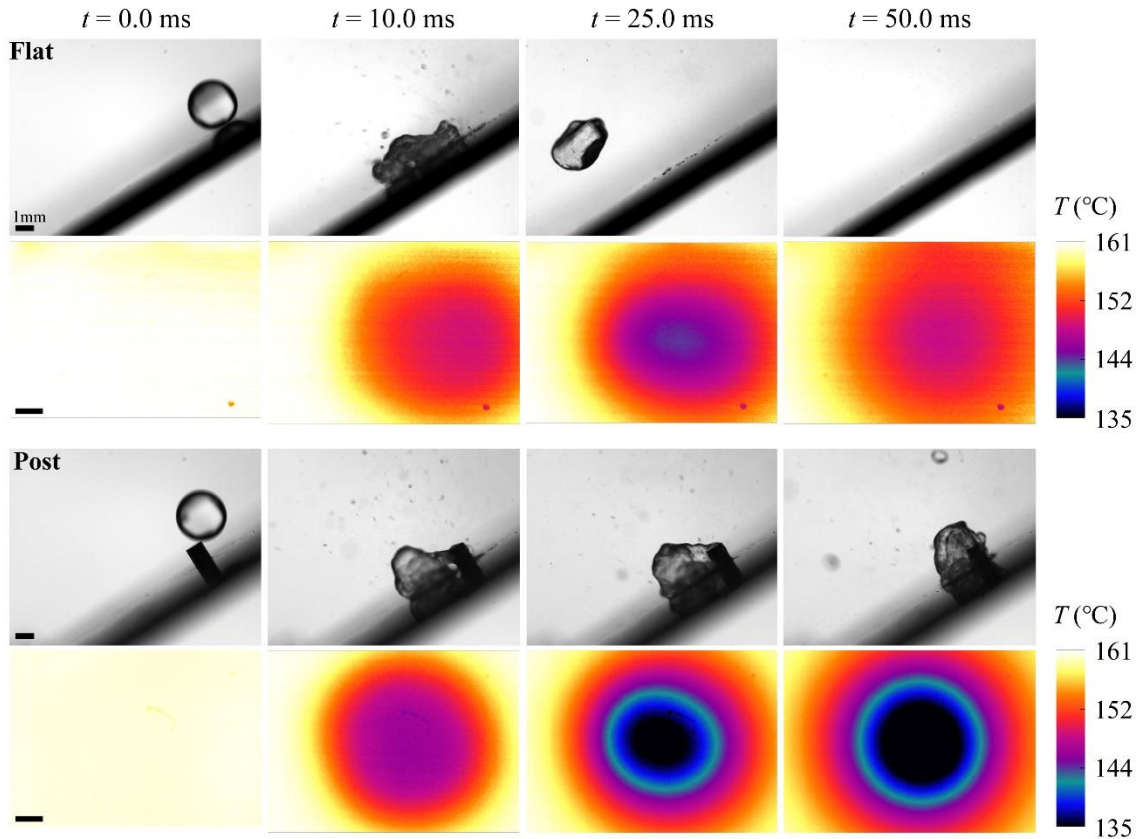


Figure 4-13 High-speed and IR imaging sequence of droplets impacting on a flat and a post substrate inclined at 30° at an initial temperature of $T_S = 160^\circ\text{C}$.

The area-weighted average temperature history of the impact area ($8\text{ mm} \times 8\text{ mm}$) is presented in Figure 4-14. At $T_S = 145^\circ\text{C}$ (nucleate boiling regime), the post increases the maximum temperature drop by 51%. However, at a similar substrate temperature on a horizontal surface (Figure 4-14(c)), the improvement from the post is minimal. At 160°C (film boiling regime), the enhancement in cooling capacity is even stronger: the post increases the maximum temperature drop on the inclined surface by 180%. The mixed boiling mode and pinning on the post prevent the droplet from sliding/bouncing off the substrate. This result shows that for both the nucleate

boiling and transition boiling regimes, the post structure can significantly increase the local heat transfer of the droplet impacting an inclined surface.

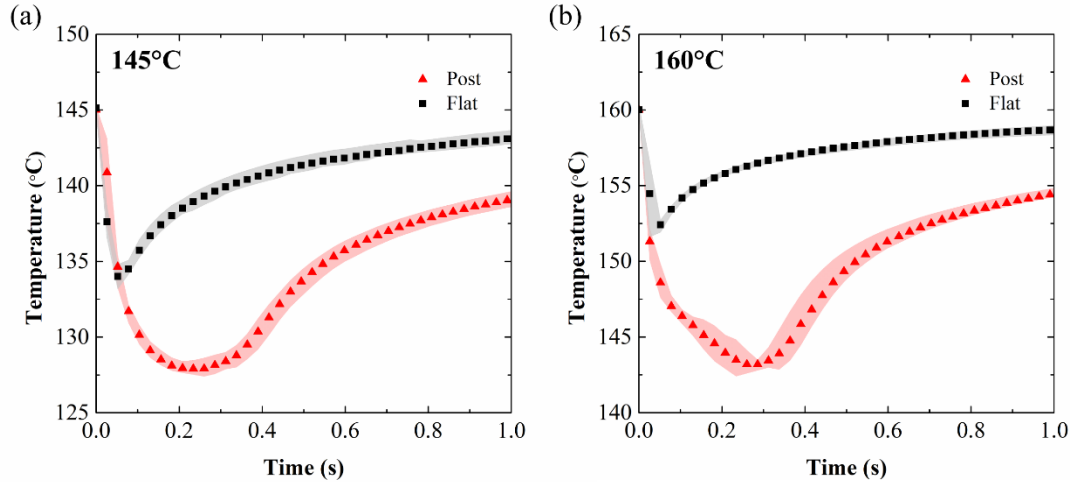


Figure 4-14 Temporal evolution of the area-weighted average bottom surface temperature for the two surfaces at (a) $T_S = 145^\circ\text{C}$ and (b) $T_S = 160^\circ\text{C}$ at an inclination angle of 30° from the horizontal.

So far, we have discussed droplet dynamics and cooling capacities for droplets centrally impacting the post right. In real-world droplet impingement applications, however, off-center impact is more likely, for which the benefit of the post structure, which prevents sliding and bounding of the droplet, might be diminished. To provide guidelines on the applicability of millimetric surface patterning, we also investigated the off-center impact on the post substrate. For an impact location uphill from the post, we can expect that the droplet will be trapped by the post structure as its sliding downward toward the post. For an impact location downhill from the post, it is easily conceivable that the post can only pin the droplet if there is contact, *i.e.*, if the droplet is able to touch the post upon spreading. Hence, we tested the droplet impact with downhill impact locations, shown in Figure 4-15. The off-center distance Δx is measured as the horizontal distance from impact location to the center of the post (on the base surface). We found that the post structure can still prevent the sliding and bouncing of the droplet for $\Delta x \leq 1.6$ mm

downhill (recall, droplet diameter $D = 2.7$ mm). Compared to a center impact at the same substrate temperature (Figure 4-12), the droplet during off-center impact is initially more deformed, with an uphill “tail” towards the post ($t = 20.0$ ms). However, eventually the pinning force is able to pull the bulk of the droplet back towards the post ($t = 40.0$ ms), where the droplet remains attached to the post structure and evaporates ($t = 80.0$ ms).

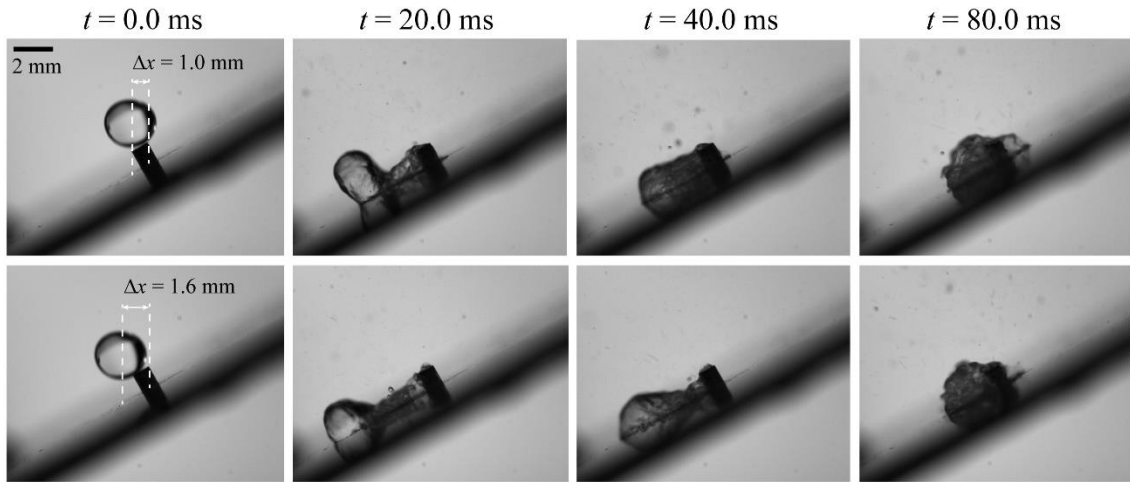


Figure 4-15 High-speed imaging sequence of off-center droplets impacting the post substrates inclined at 30° at initial temperatures of $T_s = 145^\circ\text{C}$. The horizontal distance from the impact location to the center of the post is 1.0 mm (top) and 1.6 mm (bottom).

4.4 Conclusion

This study experimentally explored hydrodynamics and heat transfer during droplet impact on a millimetric heated post. Detailed analyses have been carried out on droplet lifetime, boiling modes, and cooling capacity. We can draw the following conclusions:

The post substrate shows a 20°C higher Leidenfrost temperature compared to the flat substrate, which is attributed to a mixed boiling mode and additional pinning induced by the post.

Six different droplet impact and boiling modes were identified for initial substrate temperatures ranging from 120°C to 330°C and Weber numbers between 10 and 120: 1) deposition, 2)

atomization, 3) rebound with atomization, 4) breakup with atomization, 5) rebound, and 6) breakup. $We-T_s$ regime maps were constructed to quantify the differences in impact and boiling modes between the post and flat substrates. In general, the post enhances droplet breakup. Unexpectedly, though, a non-breakup transition region exists for the post surface within a small temperature range between the two breakup modes, which is caused by a complex interplay of inertial and pinning forces.

The post substrate is found to have a higher cooling capacity than the flat substrate between 110°C and 130°C due to a larger liquid-solid interface area and an expanding droplet profile. However, the enhancement becomes negligible at higher substrate temperatures before the droplet on flat surface transit into Leidenfrost regime.

On an inclined surface, the post substrate successfully prevents the droplet from sliding or bouncing off the substrate, which leads to a 51% to 180% increase in local temperature drop.

Overall, we show that droplet impact on a single post considerably improves the interfacial heat transfer by influencing droplet dynamics and boiling behavior. The post structure provides an enlarged contact area and a delayed Leidenfrost effect by pinning the droplet. This pinning also assists in droplet breakup and prevents the droplet from sliding off the surface for impact on an inclined substrate. These large-structured surfaces can potentially increase the cooling performance in droplet impingement cooling applications¹⁹⁰ and prevent droplet bouncing for inclined impingement surfaces¹⁹¹.

Chapter 5: Heat Transfer Mechanism of Molten Droplet Impact

5.1 Introduction

As we introduced in Chapter 1, the understanding of molten droplet impact has drawn great interest in scientific research and for industrial applications. Previous studies have investigated the droplet morphology¹⁹², spreading dynamics⁵⁵, bubble entrapment¹⁹³, and interfacial thermal resistance⁵⁷. However, little is known about the transient and microscopic heat transfer behavior between the droplet and the surface and the effect from parameters such as Weber number and surface temperature. In this study, we investigated the detailed heat transfer mechanism during molten paraffin droplet impact using synchronized high-speed optical and infrared (IR) imaging. The overall and local heat transfer, especially near the contact line region, were explored along the developing droplet profile. Controlling all other parameters, we studied the influence of impact Weber number on heat transfer and solidification dynamics. In addition, we also explored the influence of different droplet thermal conductivities by comparing paraffin wax to a droplet of Field's metal.

5.2 Experimental method

The schematic of the experimental setup is shown in Figure 5-1. Side-view shadowgraph images of the impacting paraffin droplets were recorded at 5000 frames per second (fps) using a Photron Mini AX200 high-speed camera with a Canon MP-E 65mm f/2.8 1-5X Macro Lens at a spatial resolution of 3.3 $\mu\text{m}/\text{pixel}$. A Telops FAST M3k high-speed mid-wave IR camera, equipped with a 1x long working-distance lens (Telops), recorded the thermal signals of the samples in bottom-view at 2500 fps with a spatial resolution of 30 $\mu\text{m}/\text{pixel}$. Paraffin (melting point of 55°C, Sigma-Aldrich) was maintained in its liquid state inside a syringe equipped with a heater (New

Era Pump system Inc.), which was temperature/controlled to $80\pm 0.5^\circ\text{C}$. Droplets of molten paraffin wax were generated at the tip of a needle (gauge 21), controlled by a syringe pump (New Era Pump system Inc.). Droplets with diameters of 2.2 ± 0.05 mm detached due to gravity from the needles mounted at heights between 2 cm and 6 cm, leading to impact velocities ranging from 0.5 m/s to 1.1 m/s ($We \approx 20\sim 70$), as determined from the analysis of side-view high-speed sequences of droplets just prior to impact.

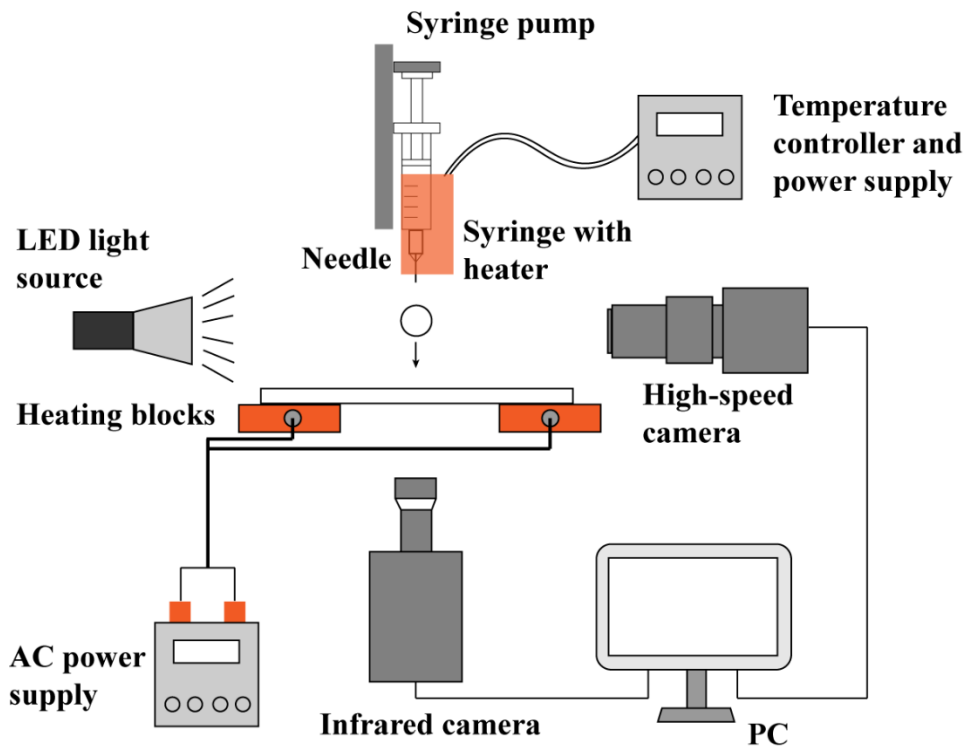


Figure 5-1 Experimental setup of molten droplet impact

The sample consisted of an IR-transparent calcium fluoride substrate (UQG Optics, thickness 1.18mm) onto which a $12\ \mu\text{m}$ thin layer of black paint (Testors 18PK, Black Enamel, 1149TT), which serves as a transducer for the thermal imaging, was spin-coated for 90 s at 1200 rpm. Note that we measured the temperature distribution of the black paint layer (\approx substrate-droplet or substrate-air interfacial temperature) due to the IR transparency of the substrate. On top of the

black paint layer, a 50 nm thin chromium film was deposited using thermal evaporation, to help block the IR signal noise from the top environment. A 100 nm thin layer of Teflon AF was then spin-coated on the Cr layer using a 1.0% Teflon AF 1601 solution with a spin time of 30 s at 2000 rpm. The equivalent static contact angle of a paraffin droplet on a Teflon AF surface at 70°C is $\theta_{eq} = 69^\circ \pm 2^\circ$.

5.3 Results and discussions

5.3.1 Transient heat transfer of paraffin droplets for impact at room temperature

Figure 5-2 shows the typical molten paraffin wax droplet dynamics during impact on a Teflon-coated surface at room temperature in side-view, along with the corresponding temperature profiles of the substrate in bottom-view and the calculated local heat flux distributions. The paraffin-substrate interface can be identified by the higher surface temperature and higher heat flux ($\sim 10^6$ W/m²). The heat flux in the region surrounding the droplet is significantly smaller, at $10^3 \sim 10^4$ W/m². During the spreading process ($t = 2.4$ ms and $t = 4.0$ ms), the droplet flattens to a liquid film, and the temperature at the droplet-substrate interface is nearly uniform. We can identify a higher heat flux near the contact line region. After the droplet reaches its maximum spreading diameter, the contact line stops moving while the capillary wave travels to the center of the droplet ($t = 6.0$ ms and $t = 7.6$ ms). Interestingly, the capillary wave induces a fluctuation in the bottom-view IR signatures and can be observed in the temperature and the corresponding heat flux distributions, despite the physical location being at the top, *i.e.*, droplet-air interface. From 6.0 ms to 7.6 ms, this capillary wave leads to a ring-shaped high temperature and high heat flux pattern, which indicates that the flow convection enhances the heat transfer. Both the temperature and the interfacial heat flux continue decreasing after the droplet pins at its

maximum diameter. At $t = 13.2$ ms, the heat flux becomes much smaller than at earlier times, which is attributed to a lower paraffin temperature near the interface and the formation of the solid-solid interface that increases the thermal resistance when the solidification front moves away from the substrate⁵⁷. After the droplet pins, the highest heat flux remains at the contact line, representing a higher solidification rate near the contact line region, which can be attributed to a thinner layer providing a lower thermal resistance.

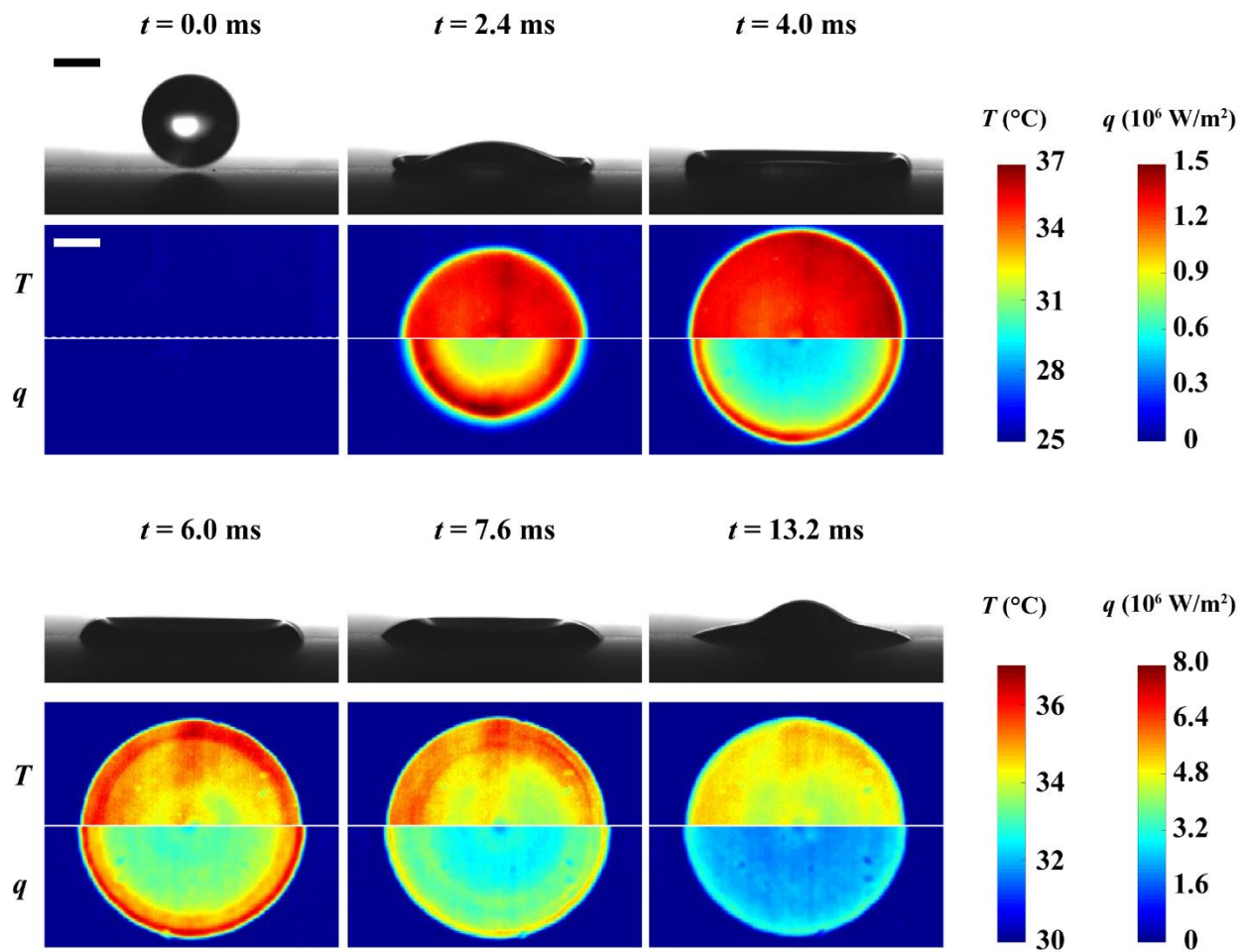


Figure 5-2 Experimental result using synchronized high-speed optical and IR imaging of a paraffin droplet impacting a Teflon AF surface at $We = 70$ at room temperature: high-speed camera snapshots of the droplet shape (top row), the corresponding temperature (middle row), and heat flux distributions (bottom row). The temperature color bar for the $t = 6.0, 7.6,$ and 13.2 ms is modified to show the temperature distribution at the interface, while the other sample area remains at room temperature (25°C). The scale bar is 1mm.

After obtaining the transient 2D profiles of temperature and heat flux, the local and overall heat transfer performance can be extracted and analyzed. Figure 5-3 shows the evolvement of the local and overall heat transfer at the paraffin-substrate interface during the impact process. Interestingly, the contact line heat flux is nearly constant during the spreading, as shown in (a). This is very different from a water droplet impact on a hot surface, where the contact line heat flux is not constant and increases as the contact line speed increases, as presented in section 3.3.1^{11, 105}. We hypothesize that at a high contact line velocity, the heat transfer originates primarily from convection (similar to impact on a heated substrate), but as the contact line slows down and the liquid solidifies, the release of latent heat becomes increasingly important and effectively compensates for the loss in sensible heating. After the droplet pins at the maximum diameter, the contact line heat flux decreases quickly as the substrate underneath the droplet heats up. In contrast, the heat flux in the central region of the droplet first decreases rapidly during spreading due to a small droplet-internal velocity and then slowly approaches a stable value after the droplet pins, which again is dictated by conduction to the thin CaF₂ substrate. However, the contact line heat flux is still higher than the other region, indicating a higher solidification rate for the later time.

Figure 5-3 (b) provides the temporal history of the area-weighted average heat flux within the maximum spreading diameter. The maximum heat flux occurs before the droplet reaches the maximum spreading diameter, similar to droplet impact on a heated surface. As the droplet pins and stabilizes, the average heat flux decreases and approaches an average heat flow of ≈ 200 kW/m² at $t \geq 12$ ms, indicating a significant amount of heat transfer even once the droplet becomes hydrodynamically stable.

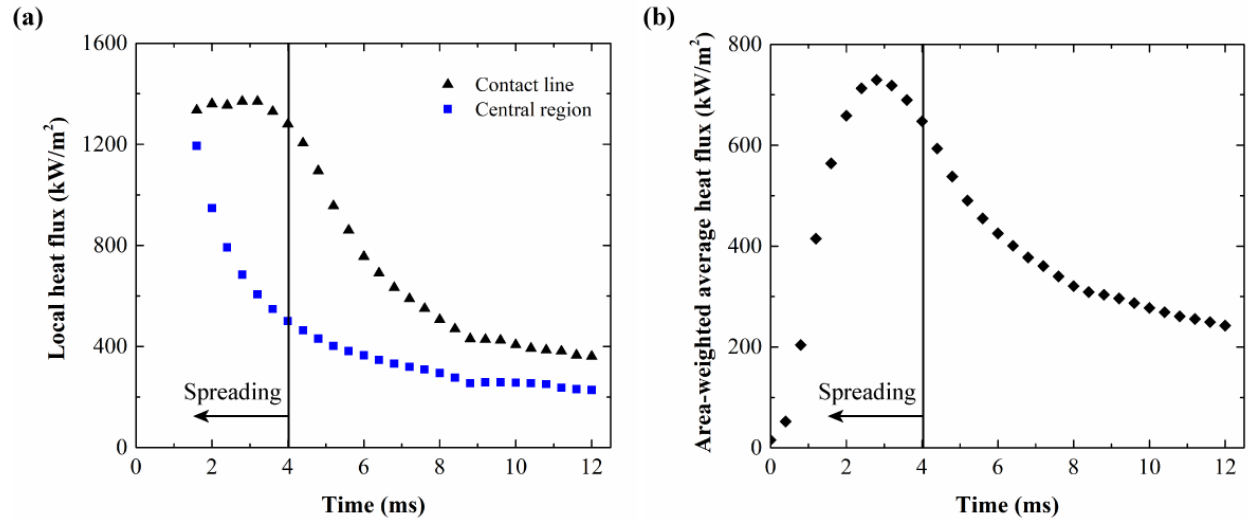


Figure 5-3 Heat flux evolution of paraffin droplet impact at $We = 70$ and a substrate originally at room temperature ($25 \pm 0.5^\circ\text{C}$). (a) Transient heat flux at the contact line and central region (1 mm^2 surrounding the impact location). (b) Transient behavior of the heat flux normalized by the maximum spreading area. The uncertainty in heat flux values is universally 10%. Error bars are omitted for the sake of clarity.

5.3.2 Effect of impact Weber number

The impact Weber number influences the droplet dynamics, especially the maximum spreading diameter, which determines the heat transfer efficiency. As we discussed before, the interfacial heat transfer is significant even after the droplet stops deforming. Hence, we measured the total transferred heat at a longer duration ($\sim 0.1 \text{ s}$) for droplet impact at different impact Weber numbers, shown in Figure 5-4 (a). For all three cases ($We = 20, 45,$ and 70), the total transferred heat continues to rise beyond $t = 100 \text{ ms}$, which shows that the droplet solidifies slowly and continues to dissipate heat to the substrate. We can also observe that a higher Weber number provides a faster increase in the total transferred heat. Two reasons for this heat transfer enhancement with higher impact velocities seem likely: a) The larger spreading diameters and/or b) different interfacial heat resistances due to higher impact pressures. To better understand the source of the heat transfer increase with increasing We , we provide the local heat flux distribution of all three cases, shown in Figure 5-4 (b). Clearly, the local heat flux values among

all three cases are identical, while the interface area is different. This result indicates that the improvement in the total transferred heat for higher We is caused solely by the larger spreading diameter of the droplet and hence larger contact (= heat transfer) area between droplet and substrate. The three curves overlap if we consider the area-weighted average heat flux (not shown here). This finding demonstrates that the overall thermal resistance is nearly independent of We , which means that the difference of contact interfacial resistances at different We reported by Shiraz D. and Chandra¹³⁶ is negligible at longer times of the solidification process.

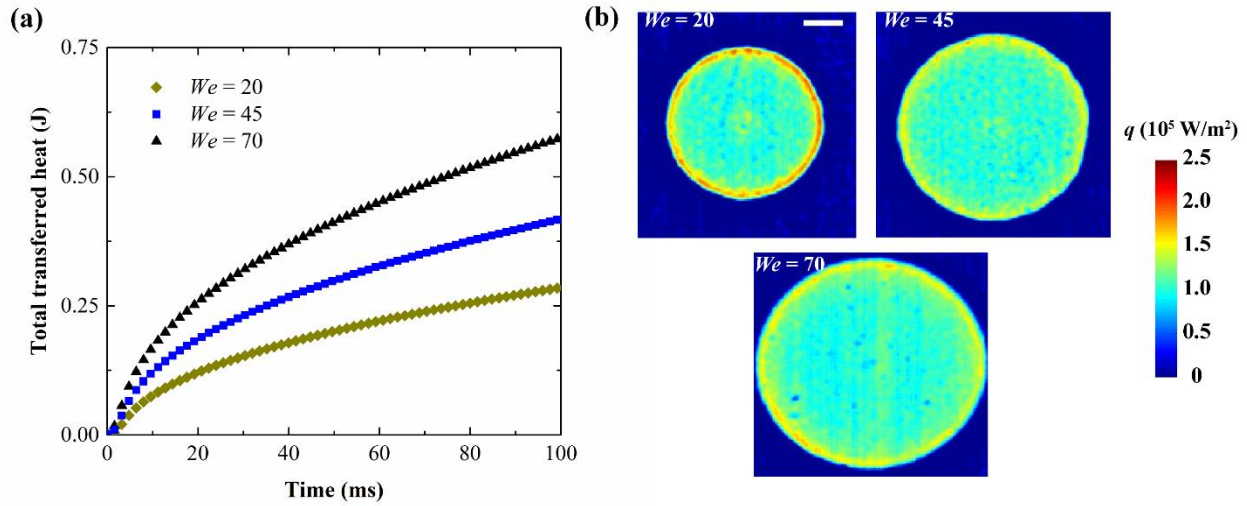


Figure 5-4 Heat transfer behavior at different impact Weber numbers. (a) The total transferred heat; (b) The transient heat flux distributions at $t = 56$ ms.

5.3.3 Effect of droplet conductivity

The heat transfer between the droplet and the substrate also strongly depends the physical properties of the droplet¹⁹⁴. Thermal conductivity is the most important property that determines the thermal resistance between the hot droplet and the cold substrate. However, the paraffin wax has a very small thermal conductivity ($\sim 0.15 \text{ W/mK}$ in liquid and $\sim 0.25 \text{ W/mK}$ in solid) that creates a large thermal barrier by itself. Hence, we repeated some experiments with Field's metal (alloy of bismuth, indium, and tin) that has a much higher thermal conductivity ($\sim 28 \text{ W/mK}$ for

both liquid and solid), but a similar melting point (62°C) as the paraffin wax. The Field's metal is heated to 100°C inside the syringe, enabling a smooth control of the droplet dispensation.

Figure 5-5 provides the results from an IR measurement at the droplet-substrate interface of a Field's metal droplet. Interestingly, from $t = 2.4$ ms to 8.0 ms, the temperature distribution is not uniform, where the central region shows a much higher temperature than the surrounding area. For the heat flux distributions at $t = 2.4$ ms and $t = 4.0$ ms, we observe that the center region yields the highest heat flux, and the contact line region is the lowest. This is very different from a paraffin droplet impact, where the temperature is almost uniform and the highest heat flux occurs at the contact line region (Figure 5-2). In Figure 5-5, from $t = 8.0$ ms to $t = 12.0$ ms, the temperature of the interface becomes more uniform than during the spreading process and the heat flux at the center region decreases to a level lower than its surrounding.

The substantial difference in the thermal behavior between the paraffin wax droplet and the Field's metal droplet is mainly caused by the difference in thermal conductivity. Due to the metal's higher thermal conductivity, the solidification, which starts from the center region (impact location)⁵⁶, can quickly propagate upward into the liquid body, providing an increase in the local heat flux for a longer time. However, for a paraffin wax droplet, heat dissipation from the traveling solidification front is hindered by the large thermal resistance in the solidified layer due to its low thermal conductivity. For paraffin, the contact line, which is shallower than the central region, shows a higher heat flux after the droplet pins, indicating a higher solidification rate there. In contrast, the contact line region of the Field's metal never experiences a local maximum in heat flux. As the center region heat flux of the Field's metal becomes lower than the surrounding after 8.0 ms, a wide region surrounding the center has a nearly uniform heat flux,

which is attributed to the partial recoil of the droplet that induces flow convection in the peripheral regions.

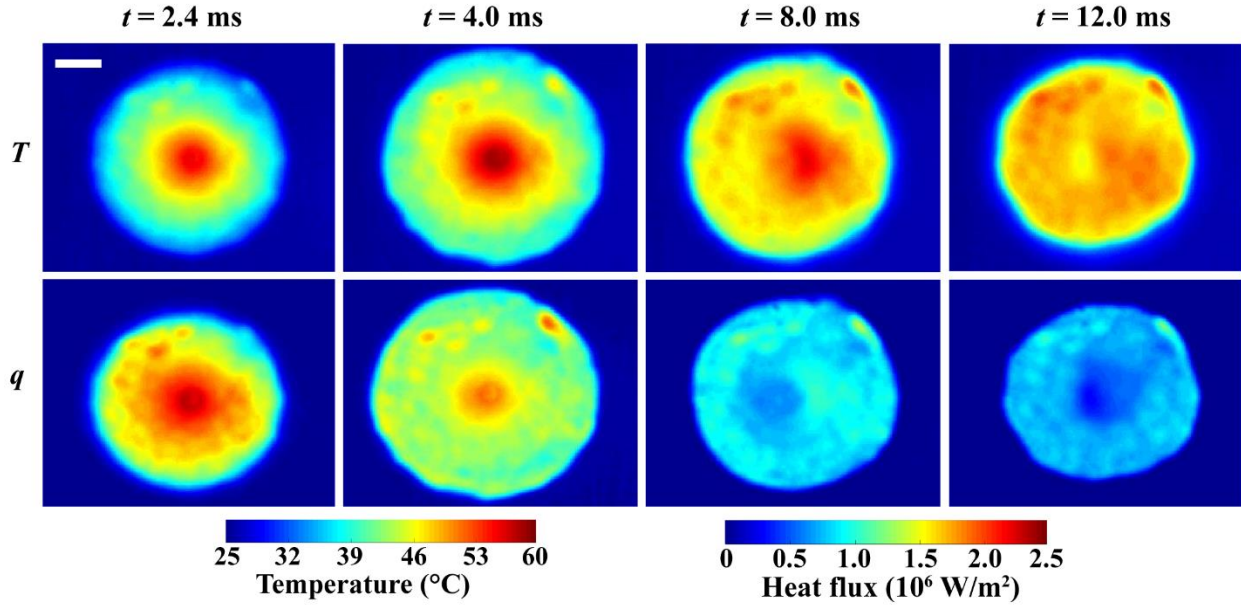


Figure 5-5 Experimental result using synchronized high-speed optical and IR imaging of a Field's metal droplet impacting a Teflon AF surface at $We = 42$ at room temperature: Temperature distributions (top row), and the corresponding heat flux distributions (bottom row).

Figure 5-6 shows the temperature history of the center region of the droplet-solid interface. After impact, the temperature first increases due to the local solidification and then decreases as the reduction of the energy, which can also be observed in Figure 5-5. Starting from $t = 14.8$ ms, the temperature increases again and continues rising after $t = 35.0$ ms. This second increase of the temperature is attributed to the recalescence of the bulk region, where the latent heat of solidification is released and transported to the interface. The high thermal conductivity of the Field's metal droplet allows a fast representation of the temperature change in the bulk region. The recalescence cannot be observed in the paraffin droplet impact process, due to the high thermal barrier of the paraffin droplet.

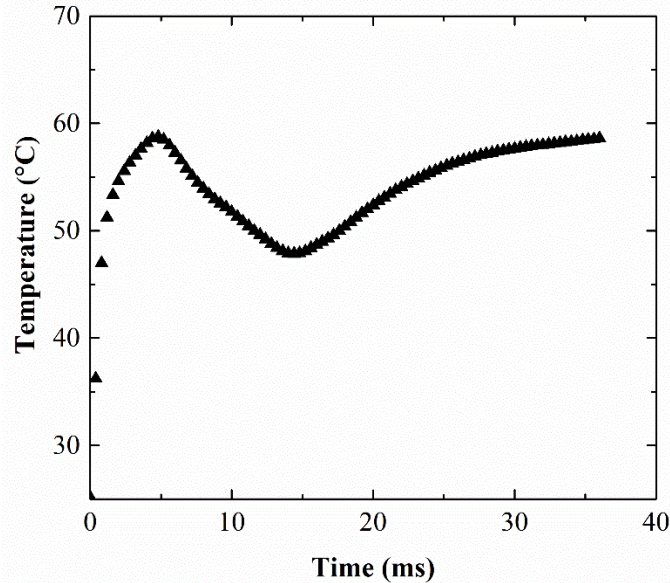


Figure 5-6 Temperature history of the center region (0.02 mm² around the impact location on the solid surface) of a Field's metal droplet impacting a Teflon AF surface at $We = 42$ at room temperature

5.4 Conclusion

This study experimentally explored the droplet dynamics and heat transfer during molten droplet impact. Detailed analyses have been carried out on the evolution of local and total heat transfer, the effect of Weber number and substrate temperature, as well as the thermal conductivity of the droplet. The contact line heat transfer is found to be nearly constant during the spreading process of the droplet impact, which is in strong contrast to (water) droplet impact on heated substrate, as presented in Chapter Chapter 3:. A higher impact Weber number improves the total transferred heat solely by an increase in spreading diameter, which demonstrates that the difference in thermal contact resistance is negligible. For a molten Field's metal droplet impact, the center region yields the highest heat flux during spreading, which indicates that the phase change starts from the impact location and develops upward into the droplet due to the higher conductivity of the metal.

Chapter 6: Conclusions and Outlook

6.1 Conclusions

Understanding the underlying physics of droplet-based two-phase thermal system is important for solving the extensive cooling requirement from electronic devices, but also enhancing the design of other industrial applications such as thermal spray coating and 3D printing. In this thesis, I have studied and analyzed various fundamental processes of droplet-based two-phase thermal management technologies.

To understand the confinement of vapor diffusion imposed by the geometric features, I studied the diffusion confinement of droplet evaporation on a supporting pillar structure. We found that raising the micropillar height from 0 to $2R$, $5R$, and $20R$ led to respectively, 26%, 35%, and 42% enhancement in the total evaporation rate of a hemispherical droplet under isothermal condition. This improvement is attributed to the diffusion transport in the downward direction that subsequently enhances evaporative transport. For droplets evaporated on heated micropillars, we found that evaporation transport was affected by a competition between the effect of increasing conduction resistance and reduced vapor diffusion confinement as the pillar height increased. For substrate temperatures 60°C , 80°C , and 98°C , the pillar heights providing the largest evaporation rates were $h = 5.5R$, $h = 3R$, and $h = 0$, respectively.

Combining the droplet evaporation with the droplet impact process, I investigated the low-Weber number droplet impact on heated hydrophobic surfaces. For the local heat flux, we found that the local contact line heat flux increases quadratically with increasing contact line velocity due to strong convection effects. At the early receding stage, the local heat flux and contact line velocity go through a transition. Denoting the drop diameter and impact velocity as D and v , we

find that the total transferred heat Q scales as $D^{1.25}v$, as validated using experiments, and is primarily conduction-dominated (evaporation plays only a minor role). For the sub-millimetric entrapped bubble that forms during receding, we find that the overall heat transfer is reduced by 5.6% and 7.1% at surface temperatures of 50°C and 65°C, respectively, as the entrapped bubble reduces the total liquid-solid interface area.

Extending my droplet impact study to a boiling mode and on a structured surface, I studied the droplet impact and Leidenfrost dynamics on a heated millimetric post. We found that the post substrate leads to a shorter droplet lifetime and a 20°C higher dynamic Leidenfrost temperature compared to a flat substrate, attributed to mixed boiling modes along the height of the post and additional pinning. The post substrate is found to have a higher cooling capacity than the flat substrate between 110°C and 130°C due to a larger liquid-solid interface area and an expanding droplet profile. On an inclined surface, the post substrate successfully prevents the droplet from sliding or bouncing off the substrate, leading to a 51% to 180% increase in local temperature drop.

Driven by the unknown heat transfer behavior during a solidifying droplet impact process, I studied the heat transfer mechanism of molten droplet impact. The contact line heat transfer is found to be nearly constant during the spreading process of the droplet impact of a low-conductivity paraffin wax droplet. The contact line region shows the highest heat flux after the droplet pins, which indicates a higher local phase change rate. The overall heat transfer is enhanced by a higher Weber number, due to a larger spreading diameter. For a molten Field's metal droplet impact, the center region yields the highest heat flux during spreading, which indicates that the phase change starts from the impact location and can develop upward into the droplet due to the higher conductivity of the metal material.

6.2 Outlook and future work

Although the research outcomes from this dissertation improve our understanding of droplet impact and phase change processes, many more unknowns are awaiting our investigation and many more thermal management technologies can be perceived. The future directions based on this dissertation can lead to a myriad of interesting and meaningful work.

For the diffusion confinement of the droplet evaporation, one possible method to further decrease the diffusion resistance is by inducing flow convection in the vapor phase. The flow convection can significantly increase the concentration gradient to enhance the evaporation rate. The flow field can be integrated with an evaporating droplet on a non-planar substrate, which may benefit from additional improvement. However, the physics of a coupled convection and diffusion evaporation process are very complex and difficult to model. Many unknowns remain. I suggest that future work should be done by exploring the detailed mechanism of decreasing vapor diffusion confinement with the existence of flow convection.

We introduced a unique feature in the droplet impact on smooth hydrophobic surfaces, the millimetric bubble entrapment. However, our understanding of this entrapment mechanism is far from sufficient. Different researchers have reported bubble entrapment with different liquids on different surfaces. However, it is not clear what actually triggers the occurrence of bubble entrapment. And more related to phenomena shown in Chapter 4, the question remains how (and why) the surface temperature affects the bubble entrapment mechanism that prevents the bubble entrapment at higher temperature. These two questions deserve future studies for a complete analysis and explanation of the bubble entrapment.

In the study of droplet impact and Leidenfrost dynamics on a heated post, we only investigated droplet impact on a stand-alone structure. What could be more interesting is using an array of

these large-structured surfaces, which would be more applicable to industrial application. The pinning effect from multiple large structures could possibly work together to further increase the dynamic Leidenfrost temperature – or could lead to enhanced flooding for too-small pillar spacings. On a horizontal or inclined surface, the structure array could provide a better improvement in the local heat transfer behavior. Hence, I suggest a future study of the droplet impact on macro-scale structure arrays.

For the molten droplet impact, the solidification process within the bulk fluid region and its effect on heat transfer effect is still not clear. A future study could combine the IR measurement with a better optical observation of the expansion of the solidification front within the droplet, for example using micro particle image velocimetry (μ PIV) or planar laser induced fluorescence (PLIF) imaging. Also, we observed an interesting change in the local heat flux distribution as the Field's metal droplet started to recoil. I propose that the recoil process of a molten droplet can lead to a significant change in the solidification rate and distribution, which can be investigated in the future.

Finally, for all the introduced fundamentals of the droplet-based two-phase thermal management methods, application-driven studies should be carried out to utilize the two-phase heat transfer techniques and explore the limitation of these advanced technologies. The need for ever-increasing cooling capacities with ever-smaller form factors will continue increasing with the continued development of microelectronic devices and power electronics. The research on two-phase thermal management should provide application-friendly and economical solutions, which can effectively help the development of new technologies and devices.

References

1. Zhang, Z.; Wang, X.; Yan, Y., A review of the state-of-the-art in electronic cooling. *e-Prime-Advances in Electrical Engineering, Electronics and Energy* **2021**, *1*, 100009.
2. Mandel, R.; Shooshtari, A.; Ohadi, M., Thin-film evaporation on microgrooved heatsinks. *Numerical Heat Transfer, Part A: Applications* **2017**, *71* (2), 111-127.
3. Yan, Z.; Jin, M.; Li, Z.; Zhou, G.; Shui, L., Droplet-Based Microfluidic Thermal Management Methods for High Performance Electronic Devices. *Micromachines* **2019**, *10* (2), 89.
4. Tissot, J.; Boulet, P.; Trinquet, F.; Fournaison, L.; Macchi-Tejeda, H., Air cooling by evaporating droplets in the upward flow of a condenser. *International Journal of Thermal Sciences* **2011**, *50* (11), 2122-2131.
5. Mahmud, M. A.; MacDonald, B. D., Experimental investigation of interfacial energy transport in an evaporating sessile droplet for evaporative cooling applications. *Physical Review E* **2017**, *95* (1), 012609.
6. Amon, C. H.; Murthy, J.; Yao, S.; Narumanchi, S.; Wu, C.-F.; Hsieh, C.-C., MEMS-enabled thermal management of high-heat-flux devices EDIFICE: embedded droplet impingement for integrated cooling of electronics. *Experimental Thermal and Fluid Science* **2001**, *25* (5), 231-242.
7. Kim, J., Spray cooling heat transfer: The state of the art. *International Journal of Heat and Fluid Flow* **2007**, *28* (4), 753-767.
8. Kumari, N.; Garimella, S. V., Characterization of the heat transfer accompanying electrowetting or gravity-induced droplet motion. *International Journal of Heat and Mass Transfer* **2011**, *54* (17-18), 4037-4050.
9. Erbil, H. Y., Evaporation of pure liquid sessile and spherical suspended drops: a review. *Adv Colloid Interface Sci* **2012**, *170* (1-2), 67-86.
10. Liang, G.; Mudawar, I., Review of drop impact on heated walls. *International Journal of Heat and Mass Transfer* **2017**, *106*, 103-126.
11. Herbert, S.; Fischer, S.; Gambaryan-Roisman, T.; Stephan, P., Local heat transfer and phase change phenomena during single drop impingement on a hot surface. *International Journal of Heat and Mass Transfer* **2013**, *61*, 605-614.
12. Quéré, D., Leidenfrost dynamics. *Annual Review of Fluid Mechanics* **2013**, *45*, 197-215.
13. Bernardin, J.; Mudawar, I., The Leidenfrost point: experimental study and assessment of existing models. **1999**.
14. Kim, S. H.; Lee, G.; Kim, H.; Kim, M. H., Leidenfrost point and droplet dynamics on heated micropillar array surface. *International Journal of Heat and Mass Transfer* **2019**, *139*, 1-9.
15. Kwon, H.-m.; Bird, J. C.; Varanasi, K. K., Increasing Leidenfrost point using micro-nano hierarchical surface structures. *Applied Physics Letters* **2013**, *103* (20), 201601.

16. Prasad, D.; Sharma, A.; Dash, S., Influence of the substrate permeability on Leidenfrost temperature. *International Journal of Heat and Mass Transfer* **2021**, *178*, 121629.
17. Kruse, C.; Anderson, T.; Wilson, C.; Zuhlke, C.; Alexander, D.; Gogos, G.; Ndao, S., Extraordinary shifts of the Leidenfrost temperature from multiscale micro/nanostructured surfaces. *Langmuir* **2013**, *29* (31), 9798-9806.
18. Kim, H.; Truong, B.; Buongiorno, J.; Hu, L.-W., On the effect of surface roughness height, wettability, and nanoporosity on Leidenfrost phenomena. *Applied Physics Letters* **2011**, *98* (8), 083121.
19. Park, J.; Kim, D. E., Dynamic Leidenfrost temperature of saturated water drops on textured surfaces. *International Journal of Heat and Mass Transfer* **2020**, *150*, 119298.
20. Pasandideh-Fard, M. Droplet impact and solidification in a thermal spray process. 1999.
21. Wang, C.-H.; Tsai, H.-L.; Wu, Y.-C.; Hwang, W.-S., Investigation of molten metal droplet deposition and solidification for 3D printing techniques. *Journal of Micromechanics and Microengineering* **2016**, *26* (9), 095012.
22. Maxwell, C., Scientific Papers, Vol. 2, No. 27. Dover Publications, New York: 1890.
23. Picknett, R. G. a. B., R., The Evaporation of Sessile or Pendant Drops in Still Air. *Journal of Colloid and Interface Science* **1977**, *61*, 336-350.
24. Birdi, K.; Vu, D.; Winter, A., A study of the evaporation rates of small water drops placed on a solid surface. *The Journal of physical chemistry* **1989**, *93* (9), 3702-3703.
25. Birdi, K.; Vu, D., Wettability and the evaporation rates of fluids from solid surfaces. *Journal of adhesion science and technology* **1993**, *7* (6), 485-493.
26. Amini, A.; Homsy, G., Evaporation of liquid droplets on solid substrates. I. Flat substrate with pinned or moving contact line. *Physical Review Fluids* **2017**, *2* (4), 043603.
27. Bourges-Monnier, C.; Shanahan, M., Influence of evaporation on contact angle. *Langmuir* **1995**, *11* (7), 2820-2829.
28. Hu, H.; Larson, R. G., Evaporation of a sessile droplet on a substrate. *The Journal of Physical Chemistry B* **2002**, *106* (6), 1334-1344.
29. McHale, G.; Rowan, S. M.; Newton, M.; Banerjee, M. K., Evaporation and the wetting of a low-energy solid surface. *The Journal of Physical Chemistry B* **1998**, *102* (11), 1964-1967.
30. Fang, X.; Li, B.; Petersen, E.; Ji, Y.; Sokolov, J. C.; Rafailovich, M. H., Factors controlling the drop evaporation constant. *The Journal of Physical Chemistry B* **2005**, *109* (43), 20554-20557.
31. Sadhal, S.; Plesset, M., Effect of solid properties and contact angle in dropwise condensation and evaporation. *Journal of Heat Transfer* **1979**, *101* (1), 48-54.
32. Guéna, G.; Poulard, C.; Cazabat, A., The leading edge of evaporating droplets. *Journal of colloid and interface science* **2007**, *312* (1), 164-171.

33. Liebermann, L., Air bubbles in water. *Journal of Applied Physics* **1957**, 28 (2), 205-211.
34. Arcamone, J.; Dujardin, E.; Rius, G.; Perez-Murano, F.; Ondarcuhu, T., Evaporation of femtoliter sessile droplets monitored with nanomechanical mass sensors. *The Journal of Physical Chemistry B* **2007**, 111 (45), 13020-13027.
35. Coutant, R. W.; Penski, E. C., Experimental evaluation of mass transfer from sessile drops. *Industrial & Engineering Chemistry Fundamentals* **1982**, 21 (3), 250-254.
36. Rowan, S. M.; Newton, M.; McHale, G., Evaporation of microdroplets and the wetting of solid surfaces. *The Journal of Physical Chemistry* **1995**, 99 (35), 13268-13271.
37. Shanahan, M.; Bourges, C., Effects of evaporation on contact angles on polymer surfaces. *International journal of adhesion and adhesives* **1994**, 14 (3), 201-205.
38. Wachters, L.; Westerling, N., The heat transfer from a hot wall to impinging water drops in the spheroidal state. *Chemical engineering science* **1966**, 21 (11), 1047-1056.
39. Qi, W.; Li, J.; Weisensee, P. B., Evaporation of Sessile Water Droplets on Horizontal and Vertical Biphobic Patterned Surfaces. *Langmuir* **2019**, 35 (52), 17185-17192.
40. Pasandideh-Fard, M.; Aziz, S.; Chandra, S.; Mostaghimi, J., Cooling effectiveness of a water drop impinging on a hot surface. *International journal of heat and fluid flow* **2001**, 22 (2), 201-210.
41. Guo, C.; Maynes, D.; Crockett, J.; Zhao, D., Heat transfer to bouncing droplets on superhydrophobic surfaces. *International Journal of Heat and Mass Transfer* **2019**, 137, 857-867.
42. Shiri, S.; Bird, J. C., Heat exchange between a bouncing drop and a superhydrophobic substrate. *Proceedings of the National Academy of Sciences* **2017**, 114 (27), 6930-6935.
43. Clavijo, C. E.; Crockett, J.; Maynes, D., Hydrodynamics of droplet impingement on hot surfaces of varying wettability. *International Journal of Heat and Mass Transfer* **2017**, 108, 1714-1726.
44. Moita, A.; Moreira, A., Drop impacts onto cold and heated rigid surfaces: morphological comparisons, disintegration limits and secondary atomization. *International journal of heat and fluid flow* **2007**, 28 (4), 735-752.
45. Tran, T.; Staat, H. J.; Susarrey-Arce, A.; Foertsch, T. C.; van Houselt, A.; Gardeniers, H. J.; Prosperetti, A.; Lohse, D.; Sun, C., Droplet impact on superheated micro-structured surfaces. *Soft Matter* **2013**, 9 (12), 3272-3282.
46. Soriano, G. E.; Zhang, T.; Alvarado, J. L., Study of the effects of single and multiple periodic droplet impingements on liquid film heat transfer. *International Journal of Heat and Mass Transfer* **2014**, 77, 449-463.
47. Moita, A.; Moreira, A. In *Boiling morphology and heat removal of impinging coolant droplets*, Proceedings of 22nd European conference on liquid atomization and spray systems, ILASS2008, Como Lake, Italy, 2008.

48. Lee, G. C.; Kang, J.-y.; Park, H. S.; Moriyama, K.; Kim, S. H.; Kim, M. H., Induced liquid-solid contact via micro/nano multiscale texture on a surface and its effect on the Leidenfrost temperature. *Experimental Thermal and Fluid Science* **2017**, *84*, 156-164.
49. Nair, H.; Staat, H. J.; Tran, T.; van Houselt, A.; Prosperetti, A.; Lohse, D.; Sun, C., The Leidenfrost temperature increase for impacting droplets on carbon-nanofiber surfaces. *Soft matter* **2014**, *10* (13), 2102-2109.
50. Jiang, M.; Wang, Y.; Liu, F.; Du, H.; Li, Y.; Zhang, H.; To, S.; Wang, S.; Pan, C.; Yu, J., Inhibiting the Leidenfrost effect above 1,000° C for sustained thermal cooling. *Nature* **2022**, *601* (7894), 568-572.
51. Dhiman, R.; McDonald, A. G.; Chandra, S., Predicting splat morphology in a thermal spray process. *Surface and Coatings Technology* **2007**, *201* (18), 7789-7801.
52. Jiang, X.; Wan, Y.; Herman, H.; Sampath, S., Role of condensates and adsorbates on substrate surface on fragmentation of impinging molten droplets during thermal spray. *Thin solid films* **2001**, *385* (1-2), 132-141.
53. Liu, M.; Yi, H.; Cao, H.; Huang, R.; Jia, L., Heat accumulation effect in metal droplet-based 3D printing: Evolution mechanism and elimination strategy. *Additive Manufacturing* **2021**, *48*, 102413.
54. Bhola, R.; Chandra, S., Parameters controlling solidification of molten wax droplets falling on a solid surface. *Journal of materials science* **1999**, *34* (19), 4883-4894.
55. Attinger, D.; Zhao, Z.; Poulikakos, D., An experimental study of molten microdroplet surface deposition and solidification: transient behavior and wetting angle dynamics. *J. Heat Transfer* **2000**, *122* (3), 544-556.
56. Shen, M.; Li, B. Q.; Yang, Q.; Bai, Y.; Wang, Y.; Zhu, S.; Zhao, B.; Li, T.; Hu, Y., A modified phase-field three-dimensional model for droplet impact with solidification. *International Journal of Multiphase Flow* **2019**, *116*, 51-66.
57. Wang, G.-X.; Matthys, E., Experimental determination of the interfacial heat transfer during cooling and solidification of molten metal droplets impacting on a metallic substrate: effect of roughness and superheat. *International Journal of Heat and Mass Transfer* **2002**, *45* (25), 4967-4981.
58. Li, J.; Shan, L.; Ma, B.; Jiang, X.; Solomon, A.; Iyengar, M.; Padilla, J.; Agonafer, D., Investigation of the confinement effect on the evaporation behavior of a droplet pinned on a micropillar structure. *Journal of colloid and interface science* **2019**, *555*, 583-594.
59. Lin, Z.; Granick, S., Patterns formed by droplet evaporation from a restricted geometry. *Journal of the American Chemical Society* **2005**, *127* (9), 2816-2817.
60. Pawlowski, L., *The science and engineering of thermal spray coatings*. John Wiley & Sons: 2008.
61. Kim, H.; Boulogne, F.; Um, E.; Jacobi, I.; Button, E.; Stone, H. A., Controlled uniform coating from the interplay of Marangoni flows and surface-adsorbed macromolecules. *Physical review letters* **2016**, *116* (12), 124501.

62. Park, J.; Moon, J., Control of colloidal particle deposit patterns within picoliter droplets ejected by ink-jet printing. *Langmuir* **2006**, *22* (8), 3506-3513.
63. Lim, T.; Han, S.; Chung, J.; Chung, J. T.; Ko, S.; Grigoropoulos, C. P., Experimental study on spreading and evaporation of inkjet printed pico-liter droplet on a heated substrate. *International Journal of Heat and Mass Transfer* **2009**, *52* (1-2), 431-441.
64. Abramzon, B.; Sirignano, W., Droplet vaporization model for spray combustion calculations. *International journal of heat and mass transfer* **1989**, *32* (9), 1605-1618.
65. Ebrahimi, A.; Dak, P.; Salm, E.; Dash, S.; Garimella, S. V.; Bashir, R.; Alam, M. A., Nanotextured superhydrophobic electrodes enable detection of attomolar-scale DNA concentration within a droplet by non-faradaic impedance spectroscopy. *Lab Chip* **2013**, *13* (21), 4248-4256.
66. Moore, A. L.; Shi, L., Emerging challenges and materials for thermal management of electronics. *Materials Today* **2014**, *17* (4), 163-174.
67. Bar-Cohen, A., Gen-3 thermal management technology: role of microchannels and nanostructures in an embedded cooling paradigm. *Journal of Nanotechnology in Engineering and Medicine* **2013**, *4* (2), 020907.
68. Won, Y.; Cho, J.; Agonafer, D.; Asheghi, M.; Goodson, K. E., Fundamental Cooling Limits for High Power Density Gallium Nitride Electronics. *IEEE Transactions on Components, Packaging and Manufacturing Technology* **2015**, *5* (6), 737-744.
69. Shuai, S.; Du, Z.; Ma, B.; Shan, L.; Dogruoz, B.; Agonafer, D. In *Numerical Investigation of Shape Effect on Microdroplet Evaporation*, ASME 2018 International Technical Conference and Exhibition on Packaging and Integration of Electronic and Photonic Microsystems, American Society of Mechanical Engineers: 2018; pp V001T04A010-V001T04A010.
70. Morse, H. W. In *On evaporation from the surface of a solid sphere. Preliminary note*, Proceedings of the American Academy of Arts and Sciences, JSTOR: 1910; pp 363-367.
71. Topley, B.; Whytlaw-Gray, R., LXXX. Experiments on the rate of evaporation of small spheres as a method of determining diffusion coefficients.—The diffusion coefficient of iodine. *The London, Edinburgh, and Dublin Philosophical Magazine and Journal of Science* **1927**, *4* (24), 873-888.
72. Fuchs, N.-A., *Evaporation and droplet growth in gaseous media*. Elsevier: 2013.
73. Johnson, J. C., Measurement of the surface temperature of evaporating water drops. *Journal of Applied Physics* **1950**, *21* (1), 22-23.
74. Langstroth, G.; Diehl, C.; Winhold, E., The evaporation of droplets in still air. *Canadian Journal of Research* **1950**, *28* (6), 580-595.
75. Picknett, R.; Bexon, R., The evaporation of sessile or pendant drops in still air. *Journal of Colloid and Interface Science* **1977**, *61* (2), 336-350.
76. Berteloot, G.; Hoang, A.; Daerr, A.; Kavehpour, H. P.; Lequeux, F.; Limat, L., Evaporation of a sessile droplet: Inside the coffee stain. *Journal of colloid and interface science* **2012**, *370* (1), 155-161.

77. MacDonald, B. D.; Ward, C., Onset of Marangoni convection for evaporating sessile droplets. *Journal of colloid and interface science* **2012**, 383 (1), 198-207.
78. Bormashenko, E.; Bormashenko, Y.; Pogreb, R.; Stanevsky, O.; Whyman, G., Droplet behavior on flat and textured surfaces: Co-occurrence of Deegan outward flow with Marangoni solute instability. *Journal of colloid and interface science* **2007**, 306 (1), 128-132.
79. Peixinho, J.; Lefèvre, G.; Coudert, F.-X.; Hurisse, O., Water evaporation in silica colloidal deposits. *Journal of colloid and interface science* **2013**, 408, 206-211.
80. Do Hong, S.; Ha, M. Y.; Balachandar, S., Static and dynamic contact angles of water droplet on a solid surface using molecular dynamics simulation. *Journal of colloid and interface science* **2009**, 339 (1), 187-195.
81. Gleason, K.; Putnam, S. A., Microdroplet evaporation with a forced pinned contact line. *Langmuir* **2014**, 30 (34), 10548-10555.
82. Multiphysics, C., Comsol. Inc., Burlington, MA, www.comsol.com **1994**.
83. Mitrovic, J., Josef Stefan and his evaporation–diffusion tube—the Stefan diffusion problem. *Chemical engineering science* **2012**, 75, 279-281.
84. Tonini, S.; Cossali, G., A multi-component drop evaporation model based on analytical solution of Stefan–Maxwell equations. *International Journal of Heat and Mass Transfer* **2016**, 92, 184-189.
85. Carle, F.; Semenov, S.; Medale, M.; Brutin, D., Contribution of convective transport to evaporation of sessile droplets: empirical model. *International Journal of Thermal Sciences* **2016**, 101, 35-47.
86. Xu, X.; Ma, L., Analysis of the effects of evaporative cooling on the evaporation of liquid droplets using a combined field approach. *Scientific reports* **2015**, 5, 8614.
87. Lu, Z.; Narayanan, S.; Wang, E. N., Modeling of Evaporation from Nanopores with Nonequilibrium and Nonlocal Effects. *Langmuir* **2015**, 31 (36), 9817-24.
88. Nguyen, T. A.; Biggs, S. R.; Nguyen, A. V., Analytical model for diffusive evaporation of sessile droplets coupled with interfacial cooling effect. *Langmuir* **2018**, 34 (23), 6955-6962.
89. Zhang, Y.; Li, Y.-R.; Yu, J.-J.; Liu, Q.-S., Three-Dimensional Numerical Simulation on Marangoni Convection in a Sessile Water Droplet Evaporating in its Vapor at Low Pressure. *Microgravity Science and Technology* **2019**, 31 (2), 231-240.
90. Günay, A. A.; Sett, S.; Oh, J.; Miljkovic, N., Steady method for the analysis of evaporation dynamics. *Langmuir* **2017**, 33 (43), 12007-12015.
91. Semenov, S.; Starov, V. M.; Rubio, R. G.; Velarde, M. G., Computer simulations of evaporation of pinned sessile droplets: influence of kinetic effects. *Langmuir* **2012**, 28 (43), 15203-15211.
92. Cengel, Y. A.; Boles, M. A., Thermodynamics: an engineering approach. *Sea* **2002**, 1000, 8862.

93. Hu, H.; Larson, R. G., Analysis of the effects of Marangoni stresses on the microflow in an evaporating sessile droplet. *Langmuir* **2005**, *21* (9), 3972-3980.
94. Hu, H.; Larson, R. G., Marangoni effect reverses coffee-ring depositions. *The Journal of Physical Chemistry B* **2006**, *110* (14), 7090-7094.
95. Girard, F.; Antoni, M.; Sefiane, K., On the effect of Marangoni flow on evaporation rates of heated water drops. *Langmuir* **2008**, *24* (17), 9207-9210.
96. Pan, Z.; Wang, H., Bénard–Marangoni instability on evaporating menisci in capillary channels. *International Journal of Heat and Mass Transfer* **2013**, *63*, 239-248.
97. Popov, Y. O., Evaporative deposition patterns: spatial dimensions of the deposit. *Physical Review E* **2005**, *71* (3), 036313.
98. Deegan, R. D.; Bakajin, O.; Dupont, T. F.; Huber, G.; Nagel, S. R.; Witten, T. A., Contact line deposits in an evaporating drop. *Physical review E* **2000**, *62* (1), 756.
99. Wang, Y.; Ma, L.; Xu, X.; Luo, J., Expressions for the evaporation of sessile liquid droplets incorporating the evaporative cooling effect. *Journal of colloid and interface science* **2016**, *484*, 291-297.
100. Pan, Z.; Dash, S.; Weibel, J. A.; Garimella, S. V. J. L., Assessment of water droplet evaporation mechanisms on hydrophobic and superhydrophobic substrates. **2013**, *29* (51), 15831-15841.
101. Diddens, C.; Kuerten, J. G.; Van der Geld, C.; Wijshoff, H., Modeling the evaporation of sessile multi-component droplets. *Journal of colloid and interface science* **2017**, *487*, 426-436.
102. Yu, Y.-S.; Wang, Z.; Zhao, Y.-P., Experimental and theoretical investigations of evaporation of sessile water droplet on hydrophobic surfaces. *Journal of colloid and interface science* **2012**, *365* (1), 254-259.
103. Siregar, D.; Kuerten, J. G.; Van der Geld, C., Numerical simulation of the drying of inkjet-printed droplets. *Journal of colloid and interface science* **2013**, *392*, 388-395.
104. Anantharaju, N.; Panchagnula, M.; Neti, S., Evaporating drops on patterned surfaces: Transition from pinned to moving triple line. *Journal of colloid and interface science* **2009**, *337* (1), 176-182.
105. Li, J.; Weisensee, P. B., Low Weber number droplet impact on heated hydrophobic surfaces. *Experimental Thermal and Fluid Science* **2022**, *130*, 110503.
106. Jia, W.; Qiu, H.-H., Experimental investigation of droplet dynamics and heat transfer in spray cooling. *Experimental Thermal and Fluid Science* **2003**, *27* (7), 829-838.
107. Liao, Y.; Eggenschwiler, P. D.; Furrer, R.; Wang, M.; Boulouchos, K., Heat transfer characteristics of urea-water spray impingement on hot surfaces. *International Journal of Heat and Mass Transfer* **2018**, *117*, 447-457.
108. Moreira, A.; Moita, A.; Panao, M., Advances and challenges in explaining fuel spray impingement: How much of single droplet impact research is useful? *Progress in energy and combustion science* **2010**, *36* (5), 554-580.

109. Shen, S.; Liang, G.; Guo, Y.; Liu, R.; Mu, X., Heat transfer performance and bundle-depth effect in horizontal-tube falling film evaporators. *Desalination and water treatment* **2013**, *51* (4-6), 830-836.
110. Bernardin, J. D.; Stebbins, C. J.; Mudawar, I., Mapping of impact and heat transfer regimes of water drops impinging on a polished surface. *International journal of heat and mass transfer* **1997**, *40* (2), 247-267.
111. Liu, L.; Cai, G.; Tsai, P. A., Drop impact on heated nanostructures. *Langmuir* **2020**, *36* (34), 10051-10060.
112. Jadidbonab, H.; Mitroglou, N.; Karathanassis, I.; Gavaises, M., Experimental study of diesel-fuel droplet impact on a similarly sized polished spherical heated solid particle. *Langmuir* **2018**, *34* (1), 36-49.
113. Liang, G.; Mu, X.; Guo, Y.; Shen, S.; Quan, S.; Zhang, J., Contact vaporization of an impacting drop on heated surfaces. *Experimental Thermal and Fluid Science* **2016**, *74*, 73-80.
114. Wang, Z.; Xiong, J.; Yao, W.; Qu, W.; Yang, Y., Experimental investigation on the Leidenfrost phenomenon of droplet impact on heated silicon carbide surfaces. *International Journal of Heat and Mass Transfer* **2019**, *128*, 1206-1217.
115. Moon, J. H.; Cho, M.; Lee, S. H., Dynamic contact angle and liquid displacement of a droplet impinging on heated textured surfaces. *Experimental Thermal and Fluid Science* **2019**, *101*, 128-135.
116. Jackson, R. G.; Kahani, M.; Karwa, N.; Wu, A.; Lamb, R.; Taylor, R.; Rosengarten, G. In *Effect of surface wettability on carbon nanotube water-based nanofluid droplet impingement heat transfer*, Journal of Physics: Conference Series, IOP Publishing: 2014; p 012024.
117. Chaze, W.; Caballina, O.; Castanet, G.; Pierson, J.-F.; Lemoine, F.; Maillet, D., Heat flux reconstruction by inversion of experimental infrared temperature measurements—Application to the impact of a droplet in the film boiling regime. *International Journal of Heat and Mass Transfer* **2019**, *128*, 469-478.
118. Teodori, E.; Pontes, P.; Moita, A.; Moreira, A., Thermographic analysis of interfacial heat transfer mechanisms on droplet/wall interactions with high temporal and spatial resolution. *Experimental Thermal and Fluid Science* **2018**, *96*, 284-294.
119. Strotos, G.; Nikolopoulos, N.; Nikas, K.-S.; Moustris, K., Cooling effectiveness of droplets at low Weber numbers: Effect of temperature. *International journal of thermal sciences* **2013**, *72*, 60-72.
120. Kumar, R.; Shukla, R. K.; Kumar, A.; Kumar, A., A computational study on air entrapment and its effect on convective heat transfer during droplet impact on a substrate. *International Journal of Thermal Sciences* **2020**, *153*, 106363.
121. Kunkelmann, C.; Ibrahim, K.; Schweizer, N.; Herbert, S.; Stephan, P.; Gambaryan-Roisman, T., The effect of three-phase contact line speed on local evaporative heat transfer: Experimental and numerical investigations. *International Journal of Heat and Mass Transfer* **2012**, *55* (7-8), 1896-1904.
122. Schweizer, N.; Stephan, P., Experimental study of bubble behavior and local heat flux in pool boiling under variable gravitational conditions. *Multiphase Science and Technology* **2009**, *21* (4).

123. Ibrahim, K.; Abd Rabbo, M.; Gambaryan-Roisman, T.; Stephan, P. In *Experimental investigation of micro-scale heat transfer at an evaporating moving 3-phase contact line*, International Heat Transfer Conference, 2010; pp 783-790.
124. Qi, W.; Weisensee, P. B., Dynamic wetting and heat transfer during droplet impact on bi-phobic wettability-patterned surfaces. *Physics of Fluids* **2020**, *32* (6), 067110.
125. Kim, S.; Moon, M.-W.; Kim, H.-Y., Drop impact on super-wettability-contrast annular patterns. *Journal of Fluid Mechanics* **2013**, *730*, 328.
126. Bartolo, D.; Josserand, C.; Bonn, D., Singular jets and bubbles in drop impact. *Physical review letters* **2006**, *96* (12), 124501.
127. Hung, Y.-L.; Wang, M.-J.; Huang, J.-W.; Lin, S.-Y., A study on the impact velocity and drop size for the occurrence of entrapped air bubbles–Water on parafilm. *Experimental thermal and fluid science* **2013**, *48*, 102-109.
128. Chen, L.; Li, L.; Li, Z.; Zhang, K., Submillimeter-sized bubble entrapment and a high-speed jet emission during droplet impact on solid surfaces. *Langmuir* **2017**, *33* (29), 7225-7230.
129. Pittoni, P. G.; Lin, Y.-C.; Wang, R.-J.; Yu, T.-S.; Lin, S.-Y., Bubbles entrapment for drops impinging on polymer surfaces: The roughness effect. *Experimental Thermal and Fluid Science* **2015**, *62*, 183-191.
130. Bouwhuis, W.; van der Veen, R. C.; Tran, T.; Keij, D. L.; Winkels, K. G.; Peters, I. R.; van der Meer, D.; Sun, C.; Snoeijer, J. H.; Lohse, D., Maximal air bubble entrainment at liquid-drop impact. *Physical review letters* **2012**, *109* (26), 264501.
131. Mehdi-Nejad, V.; Mostaghimi, J.; Chandra, S., Air bubble entrapment under an impacting droplet. *Physics of fluids* **2003**, *15* (1), 173-183.
132. Zhang, X.; Liu, X.; Wu, X.; Min, J., Impacting-freezing dynamics of a supercooled water droplet on a cold surface: Rebound and adhesion. *International Journal of Heat and Mass Transfer* **2020**, *158*, 119997.
133. Chu, F.; Wen, D.; Wu, X., Frost self-removal mechanism during defrosting on vertical superhydrophobic surfaces: Peeling off or jumping off. *Langmuir* **2018**, *34* (48), 14562-14569.
134. Graeber, G.; Schutzius, T. M.; Eghlidi, H.; Poulikakos, D., Spontaneous self-dislodging of freezing water droplets and the role of wettability. *Proceedings of the National Academy of Sciences* **2017**, *114* (42), 11040-11045.
135. Murr, L. E.; Johnson, W. L., 3D metal droplet printing development and advanced materials additive manufacturing. *Journal of Materials Research and Technology* **2017**, *6* (1), 77-89.
136. Aziz, S. D.; Chandra, S., Impact, recoil and splashing of molten metal droplets. *International journal of heat and mass transfer* **2000**, *43* (16), 2841-2857.
137. Sielaff, A. Experimental investigation of single bubbles and bubble interactions in nucleate boiling. Technische Universität, 2014.

138. Gerardi, C. D. Investigation of the pool boiling heat transfer enhancement of nano-engineered fluids by means of high-speed infrared thermography. Massachusetts Institute of Technology, 2009.
139. Drelich, J., Guidelines to measurements of reproducible contact angles using a sessile-drop technique. *Surface innovations* **2013**, *1* (4), 248-254.
140. Bergman, T. L.; Incropera, F. P.; DeWitt, D. P.; Lavine, A. S., *Fundamentals of heat and mass transfer*. John Wiley & Sons: 2011.
141. Clanet, C.; Béguin, C.; Richard, D.; Quéré, D., Maximal deformation of an impacting drop. *Journal of Fluid Mechanics* **2004**, *517*, 199.
142. Richard, D.; Clanet, C.; Quéré, D., Contact time of a bouncing drop. *Nature* **2002**, *417* (6891), 811-811.
143. Liang, G.; Shen, S.; Guo, Y.; Zhang, J., Boiling from liquid drops impact on a heated wall. *International journal of heat and mass transfer* **2016**, *100*, 48-57.
144. Laan, N.; de Bruin, K. G.; Bartolo, D.; Josserand, C.; Bonn, D., Maximum diameter of impacting liquid droplets. *Physical Review Applied* **2014**, *2* (4), 044018.
145. Renardy, Y. Y.; Popinet, S.; Duchemin, L.; Renardy, M. J.; Zaleski, S.; Josserand, C.; Drumright-Clarke, M.; Richard, D.; Clanet, C.; Quéré, D., Pyramidal and toroidal water drops after impact on a solid surface. **2003**.
146. Josserand, C.; Thoroddsen, S. T., Drop impact on a solid surface. *Annual review of fluid mechanics* **2016**, *48*, 365-391.
147. van der Veen, R. C.; Tran, T.; Lohse, D.; Sun, C., Direct measurements of air layer profiles under impacting droplets using high-speed color interferometry. *Physical Review E* **2012**, *85* (2), 026315.
148. Klaseboer, E.; Manica, R.; Chan, D. Y., Universal behavior of the initial stage of drop impact. *Physical review letters* **2014**, *113* (19), 194501.
149. Ibrahim, K.; Abd Rabbo, M.; Gambaryan-Roisman, T.; Stephan, P., Experimental investigation of evaporative heat transfer characteristics at the 3-phase contact line. *Experimental Thermal and Fluid Science* **2010**, *34* (8), 1036-1041.
150. Tang, C.; Qin, M.; Weng, X.; Zhang, X.; Zhang, P.; Li, J.; Huang, Z., Dynamics of droplet impact on solid surface with different roughness. *International Journal of Multiphase Flow* **2017**, *96*, 56-69.
151. Diaz, R.; Guo, Z., Molecular dynamics study of wettability and pitch effects on maximum critical heat flux in evaporation and pool boiling heat transfer. *Numerical Heat Transfer, Part A: Applications* **2017**, *72* (12), 891-903.
152. Bai, P.; Zhou, L.; Du, X., Effects of liquid film thickness and surface roughness ratio on rapid boiling of water over copper plates. *International Communications in Heat and Mass Transfer* **2021**, *120*, 105036.
153. Xu, Y.; Tian, L.; Zhu, C.; Zhao, N., Numerical investigation of droplet impact on heated surfaces with pillars. *Physics of Fluids* **2022**, *34* (2), 023305.

154. Kim, S. H.; Jiang, Y.; Kim, H., Droplet impact and LFP on wettability and nanostructured surface. *Experimental Thermal and Fluid Science* **2018**, *99*, 85-93.
155. Ma, Q.; Wu, X.; Li, T., Droplet impact on superheated surfaces with different wettabilities. *International Journal of Heat and Mass Transfer* **2019**, *141*, 1181-1186.
156. Van Limbeek, M. A.; Schaarsberg, M. H. K.; Sobac, B.; Rednikov, A.; Sun, C.; Colinet, P.; Lohse, D., Leidenfrost drops cooling surfaces: theory and interferometric measurement. *Journal of fluid mechanics* **2017**, *827*, 614-639.
157. van Limbeek, M. A.; Ramírez-Soto, O.; Prosperetti, A.; Lohse, D., How ambient conditions affect the Leidenfrost temperature. *Soft matter* **2021**, *17* (11), 3207-3215.
158. Orejon, D.; Sefiane, K.; Takata, Y., Effect of ambient pressure on Leidenfrost temperature. *Physical Review E* **2014**, *90* (5), 053012.
159. Park, J.; Kim, D. E., Dynamic Leidenfrost behaviors of different fluid drops on superheated surface: Scaling for vapor film thickness. *Physics of Fluids* **2019**, *31* (10), 101702.
160. Zhong, L.; Guo, Z., Effect of surface topography and wettability on the Leidenfrost effect. *Nanoscale* **2017**, *9* (19), 6219-6236.
161. Rozhkov, A.; Prunet-Foch, B.; Vignes-Adler, M., Impact of water drops on small targets. *Physics of Fluids* **2002**, *14* (10), 3485-3501.
162. Al-Sharafi, A.; Yilbas, B. S.; Al-Qahtani, H., Heating enhancement of a Droplet on a Superhydrophobic Surface. *Scientific Reports* **2020**, *10* (1), 1-15.
163. Wang, Z.; Lin, K.; Zhao, Y.-P., The effect of sharp solid edges on the droplet wettability. *Journal of colloid and interface science* **2019**, *552*, 563-571.
164. Ding, S.; Liu, X.; Wu, X.; Zhang, X., Droplet breakup and rebound during impact on small cylindrical superhydrophobic targets. *Physics of Fluids* **2020**, *32* (10), 102106.
165. Ren, W.; Foltyn, P.; Geppert, A.; Weigand, B., Air entrapment and bubble formation during droplet impact onto a single cubic pillar. *Scientific Reports* **2021**, *11* (1), 1-11.
166. Arogeti, M.; Sher, E.; Bar-Kohany, T., Drop impact on small targets with different target-to-drop diameters ratio. *Chemical Engineering Science* **2019**, *193*, 89-101.
167. Ding, S.; Hu, Z.; Dai, L.; Zhang, X.; Wu, X., Droplet impact dynamics on single-pillar superhydrophobic surfaces. *Physics of Fluids* **2021**, *33* (10), 102108.
168. Lisco, F.; Bukhari, F.; Uličná, S.; Isbilir, K.; Barth, K. L.; Taylor, A.; Walls, J. M., Degradation of hydrophobic, anti-soiling coatings for solar module cover glass. *Energies* **2020**, *13* (15), 3811.
169. Asmatulu, R.; Mahmud, G. A.; Hille, C.; Misak, H. E., Effects of UV degradation on surface hydrophobicity, crack, and thickness of MWCNT-based nanocomposite coatings. *Progress in Organic Coatings* **2011**, *72* (3), 553-561.

170. Liang, G.; Mudawar, I., Review of spray cooling–Part 2: High temperature boiling regimes and quenching applications. *International Journal of Heat and Mass Transfer* **2017**, *115*, 1206-1222.
171. Lim, D. H.; Kim, S. C., Thermal performance of oil spray cooling system for in-wheel motor in electric vehicles. *Applied Thermal Engineering* **2014**, *63* (2), 577-587.
172. Lin, Y.; Chu, F.; Wu, X., Evaporation and boiling of water-alcohol droplets: Dynamic characteristics of wetting and heat transfer. *International Communications in Heat and Mass Transfer* **2022**, *134*, 106045.
173. Bernardin, J. D., *Leidenfrost point and film boiling heat transfer of single droplets and sprays*. Purdue University: 1996.
174. Brody, J.; Brown, M., Transient heat conduction in a heat fin. *American Journal of Physics* **2017**, *85* (8), 582-586.
175. Shirota, M.; van Limbeek, M. A.; Sun, C.; Prosperetti, A.; Lohse, D., Dynamic Leidenfrost effect: Relevant time and length scales. *Physical review letters* **2016**, *116* (6), 064501.
176. Chausalkar, A.; Kong, S.-C.; Michael, J. B., Multicomponent drop breakup during impact with heated walls. *International Journal of Heat and Mass Transfer* **2019**, *141*, 685-695.
177. Squire, H., Investigation of the instability of a moving liquid film. *British Journal of Applied Physics* **1953**, *4* (6), 167.
178. van Limbeek, M. A.; Shirota, M.; Sleutel, P.; Sun, C.; Prosperetti, A.; Lohse, D., Vapour cooling of poorly conducting hot substrates increases the dynamic Leidenfrost temperature. *International journal of heat and mass transfer* **2016**, *97*, 101-109.
179. Lipson, N.; Chandra, S., Cooling of porous metal surfaces by droplet impact. *International Journal of Heat and Mass Transfer* **2020**, *152*, 119494.
180. Kim, W. S.; Lee, S. Y., Behavior of a water drop impinging on heated porous surfaces. *Experimental Thermal and Fluid Science* **2014**, *55*, 62-70.
181. Gao, X.; Xia, Y.; Li, R., Transient boiling of a droplet stream quenching microstructured surfaces. *International Journal of Heat and Mass Transfer* **2021**, *164*, 120580.
182. Soriano, G.; Alvarado, J. L.; Lin, Y. P. In *Experimental characterization of single and multiple droplet impingement on surfaces subject to constant heat flux conditions*, International Heat Transfer Conference, 2010; pp 707-715.
183. Shen, J.; Liburdy, J. A.; Pence, D. V.; Narayanan, V., Droplet impingement dynamics: effect of surface temperature during boiling and non-boiling conditions. *Journal of Physics: Condensed Matter* **2009**, *21* (46), 464133.
184. Craig, V.; Ninham, B.; Pashley, R. M., Effect of electrolytes on bubble coalescence. *Nature* **1993**, *364* (6435), 317-319.
185. Breitenbach, J.; Roisman, I. V.; Tropea, C., Drop collision with a hot, dry solid substrate: Heat transfer during nucleate boiling. *Physical Review Fluids* **2017**, *2* (7), 074301.

186. Wang, Y.; El Bouhali, A.; Lyu, S.; Yu, L.; Hao, Y.; Zuo, Z.; Liu, S.; Sun, C., Leidenfrost drop impact on inclined superheated substrates. *Physics of Fluids* **2020**, *32* (11), 112113.
187. Lim, E.; Ng, B. T.; Hung, Y. M.; Tan, M. K., Graphene-mediated suppression of Leidenfrost effect for droplets on an inclined surface. *International Journal of Thermal Sciences* **2022**, *174*, 107426.
188. Benter, J. D.; Restrepo, J. D. P.; Stanley, C.; Rosengarten, G., Successive droplet impingement onto heated surfaces of different wettabilities. *International Journal of Heat and Mass Transfer* **2022**, *185*, 122169.
189. Takata, Y.; Kohno, M.; Hidaka, S.; Wakui, T.; Majid, A. I.; Kuntoro, H. Y.; Widyaparaga, A., The effects of the surface roughness on the dynamic behavior of the successive micrometric droplets impacting onto inclined hot surfaces. *International Journal of Heat and Mass Transfer* **2016**, *101*, 1217-1226.
190. Benter, J. D.; Bhatt, V.; Restrepo, J. D. P.; Stanley, C.; Rosengarten, G., Non-simultaneous droplet impingement cooling of a solid heated surface. *International Journal of Heat and Mass Transfer* **2022**, *191*, 122752.
191. Takata, Y.; Widyatama, A.; Majid, A. I.; Wiranata, A.; Widyaparaga, A.; Kohno, M.; Hidaka, S., The interfacial dynamics of the micrometric droplet diameters during the impacting onto inclined hot surfaces. *International Journal of Heat and Mass Transfer* **2018**, *126*, 39-51.
192. Bussmann, M.; Mostaghimi, J.; Chandra, S., On a three-dimensional volume tracking model of droplet impact. *Physics of Fluids* **1999**, *11* (6), 1406-1417.
193. Xiong, W.; Cheng, P., Numerical investigation of air entrapment in a molten droplet impacting and solidifying on a cold smooth substrate by 3D lattice Boltzmann method. *International Journal of Heat and Mass Transfer* **2018**, *124*, 1262-1274.
194. Zhao, Z.; Poulikakos, D.; Fukai, J., Heat transfer and fluid dynamics during the collision of a liquid droplet on a substrate—I. Modeling. *International Journal of Heat and Mass Transfer* **1996**, *39* (13), 2771-2789.

Appendix 1: Sample fabrication and experimental uncertainty of droplet evaporation on the micropillar

The micropillar samples with different heights (0, 50, 75, 100, 125, and 150 μm) used for the experimental test were fabricated using thermal oxidation, photolithography, and reactive-ion etching (RIE). A 300 μm thick, double side polished, 4" wafer (University Wafer) was used for the microfabrication. Silicon dioxide layers with a thickness of 450 nm were grown on the both sides of the wafers in a tube furnace (Lindberg/Blue M). RTDs and platinum heaters were deposited on one side of the wafer in a physical vapor deposition chamber (Kurt J. Lesker, PVD 75). Though-holes and micropillars were dry etched using deep reactive ion etching (DRIE) in an RIE chamber (Oxford Instrument, Plasmalab System 100). Figure. A1 shows the detailed fabrication process and SEM images of the fabricated micropillars.

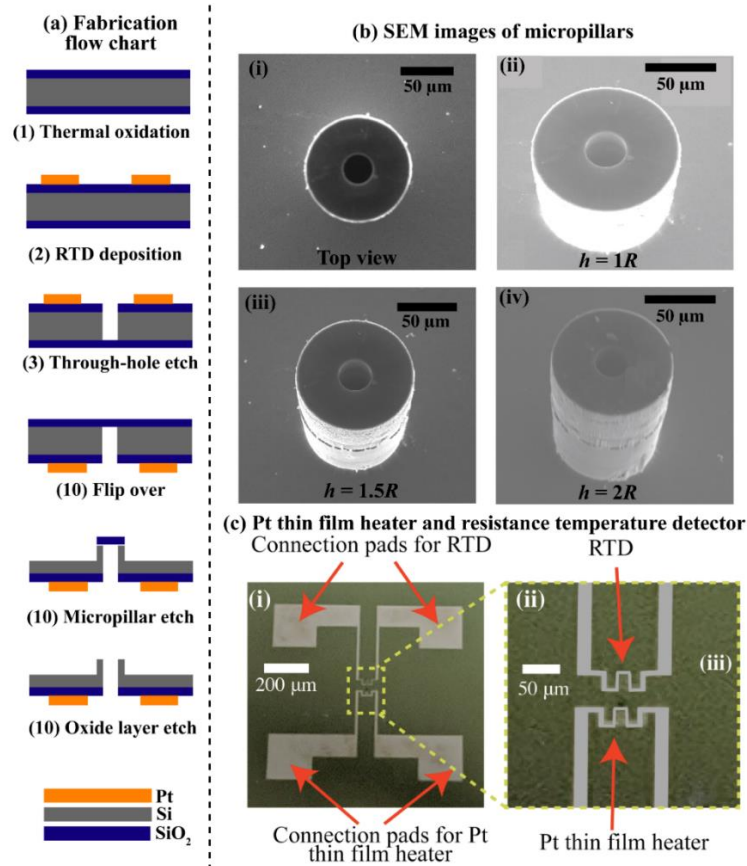


Figure A1 (a) Micropillar fabrication flow chart, including oxidation, photolithography, metal deposition, and etching. (b) SEM isometric views images of the fabricated porous micropillar structures. (c) Pt thin film region and the resistance temperature detector on the back side of the

sample. There are two connection pads each for the RTD detector and the RTD heater, assembled near the center of the samples. The resistance detector and Pt thin film heater pattern occupy the region around the center of the samples. The small wire width of the Pt thin film patterns shown in (ii) account for ~95% of the total electrical resistance.

In our experiment, after the porous micropillar samples were fabricated, silicon dioxide layer was first etched in an RIE chamber to expose the bare silicon surface. Subsequently, the samples were cleaned using O₂ plasma for 15 minutes to remove the photoresist and any other contaminations in the microfabrication process. During the Plasma treatment, a thin SiO₂ layer is grown on the silicon wafer which enhances the wettability of the top micropillar surface. The contact angle of the water droplet on plasma treated silicon wafer was then measured by a goniometer as shown in the image below:

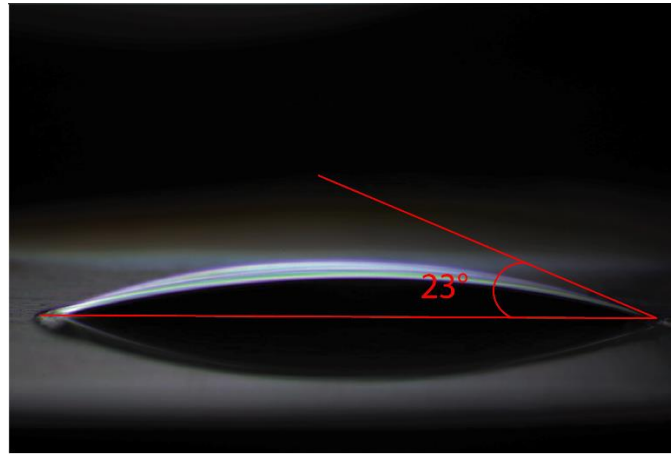


Figure A2. Contact angle of water on silicon

A digital thermometer/ hygrometer (AcuRite, # 00325A1) was used in our lab to measure both the room temperature and the indoor relative humidity during our experiments. The variation in room temperature is less than 0.5 °C during the experiments, and the relative humidity variation during the experiments is less than 5%. Both the variation in room temperature and the relative humidity have little effects on our experiments. During the experiments, the maximum heights of the microdroplets were adjusted carefully by controlling the inlet pressure. However, there are still 5-pixel uncertainty in determine the micropillar liquid-vapor interface. Since we used a microscope lens with a Numerical aperture (NA) of 4.2, each pixel stands for ~0.3 μm. Therefore, the total uncertainty for the microdroplets' height is ~1.5 μm. For a maximum microdroplet height of 50 μm, the corresponding percentage uncertainty in the microdroplets' height is 3%.

In the RTD calibration process, the relation between the electrical resistance and the substrate temperature was obtained, and then fitted by linear curves. However, ±0.3°C variation was found during the fitting process.